Multiscale Modeling of Thermomechanical Properties of Ceramic Pebbles

Zur Erlangung des akademischen Grades
Doktor der Ingenieurwissenschaften

Der Fakultät für Maschinenbau
Karlsruher Institut für Technologie (KIT)

genehmigte
Dissertation
von

M. Eng. Shuo Zhao

Tag der mündlichen Prüfung: 25. Nov. 2010
Hauptreferent: Prof. Dr. -Ing. habil. M. Kamlah
Korreferent: Prof. Dr. rer. nat. O. Kraft

Abstract

Ceramic pebbles are foreseen to be used as tritium breeder in helium cooled pebble bed (HCPB) blankets in fusion reactors. The pebbles will be subject to severe conditions, such as high temperature and irradiation. They may fail during thermomechanical loading. The failure of pebbles will influence the macroscopic thermomechanical response of pebble beds. Moreover, fragments of crushed pebbles could block the evacuation of purge gas. As a result, the tritium produced in pebble beds could not be brought away for continuous fusion reaction. Therefore, it is important to investigate the influence of pebble failure in pebble beds. As for the thermal properties of pebble beds, the thermal stress and thermal conductivity is of big concern for the blanket design.

We aim to derive the pebble strength for pebble-pebble contact like that in pebble beds. At first, crush tests for single pebbles are carried out to supply the crush load for plate-pebble contact. A strength or failure model is desired to explain the influence of plate material. In oder to validate the models based on stress analysis, an analytical solution is derived for stresses in a spherical pebble subjected to various loads along different directions. However, it is found that some models based on stresses inside the pebble can not explain the influence of plate material. Instead, the influence can be explained by a probabilistic model in terms of strain energy absorbed by the pebble. This model is then used to predict the pebble-pebble contact strength. Subsequently, the predicted strength is imported into discrete element simulations to investigate the influence of pebble failure on the macroscopic stress-strain relation. The influence of some input parameters, such as the friction coefficient between pebbles, in the discrete element code is studied as well.

The thermal stress is studied by thermal expansion and degradation of material parameters of pebbles. Each pebble has a homogenous temperature, but the temperature between pebbles can be different. The thermal conductivity of pebble beds is derived from the contact information in pebble beds. The calculated increase of thermal conductivity with stress agrees well with experimental results for the same stress level.

Zusammenfassung

In der Ummantelung von Fusionsreaktoren sind heliumgekühlten Schüttbetten zur Tritiumerzeugung vorgesehen. Die Schüttbetten bestehen aus keramischem Granulat, das im Fusionsreaktor extremen Umgebungsbedingungen, wie sehr hohen Temperaturen und starker Strahlung, ausgesetzt ist. Die daraus resultierende thermomechanische Belastung des Materials kann – neben der Veränderung der Wärmeleitfähigkeit – zur Zerstörung einzelner Partikel führen. Das Versagen einzelner Partikel beeinflusst die makroskopischen Eigenschaften des gesamten Schüttbettes und verändert damit die Antwort auf äußere Belastung und die Wärmeleitfähigkeit. Zudem können Bruchstücke die Abführung des Spülgases und den damit verbundenen Abtransport des gewonnenen Tritiums behindern, was zur Folge hat, dass dieses sich im Brutmaterial akkumuliert und den weiteren Abläufen des Fusionsreaktors nicht zur Verfügung steht. Um die Funktionsfähigkeit der Schüttbetten zu gewährleisten, ist es notwendig, den Einfluss der Schädigung einzelner Granulatkörner auf die Eigenschaften des Schüttbettes zu untersuchen. Hierbei sind thermomechanische Eigenschaften der Partikelstruktur, insbesondere Wärmeleitfähigkeit und Größe der thermisch induzierten Spannungen, von besonderer Bedeutung für die Gestaltung und Dimensionierung der Schüttbetten.

Um das Versagensverhalten der Partikeln zu bestimmen, soll deren Festigkeit im direkten Kontakt, wie er in Schüttbetten vorliegt, ermittelt werden. Zu diesem Zweck werden zunächst Untersuchungen zum Versagen einzelner Partikel zwischen Platten durchgeführt, um deren maximal ertragbare Last zu bestimmen. Auf Grundlage dieser Untersuchungen werden verschiedene Modellierungsansätze zur Beschreibung der Festigkeit bzw. des Versagensverhaltens und zur Berücksichtigung des Einflusses des Plattenmaterials evaluiert. Dazu wird eine analytische Lösung für die Spannungen in einem kugelförmigen Partikel unter mehreren in verschiedene Richtungen wirkenden Lasten hergeleitet. Dabei stellen sich Versagensmodelle, die auf der Spannungsverteilung im Partikel basieren als weniger geeignet heraus, da sie den Einfluss des Plattenmaterials nicht ausreichend berücksichtigen. Ein probabilistisches Modell hingegen, das die von der Kugel ab-

sorbierte Verformungsenergie betrachtet, bildet das beobachtete Schädigungsverhalten sehr gut nach. Dieses Modell wird dazu verwendet, das Kontaktverhalten zwischen zwei Granulatkörnern vorherzusagen. Die auf diese Weise ermittelte Kontaktfestigkeit wird in Diskrete Elemente Modelle übertragen, um darin den Einfluss der Zerstörung einzelner Partikel auf das makroskopische Verhalten des Schüttbettes zu untersuchen. Des Weiteren wurde der Einfluss einiger Parameter, wie zum Beispiel des Reibkoeffizienten, auf das Modellverhalten untersucht.

Die thermisch induzierten Spannungen werden in Abhängigkeit von der thermischen Ausdehnung der Partikel und der Degradation der Materialparameter untersucht. Die Temperatur innerhalb eines Partikels wird dabei als konstant angenommen, von Partikel zu Partikel hingegen können die Temperaturen variieren. Die für die Temperaturverteilung entscheidende Wärmeleitfähigkeit der Schüttbetten wird aus den Kontaktinformationen der Partikelstruktur hergeleitet. Die dabei gefundene Zunahme der thermischen Leitfähigkeit bei steigender Belastung korreliert mit den experimentell gewonnenen Ergebnissen.

List of Figures

List of Tables

Contents

Symbols

Symbols	Meaning
a	flaw size
a_c	critical flaw size
k	thermal conductivity
k_s	shear stiffness
m	Weibull modulus
p	(1) pressure
	(2) probability density function (PDF)
p_a	PDF of flaw size
p_c	PDF of critical flaw size
p_e	PDF of contact force or energy
p_s	PDF of strength of single particles
r_-	reduction ratio
z_s	surface flaw density
z_v	volume flaw density
$\boldsymbol{k}^*$	effective thermal conductivity tensor
$\boldsymbol{n}(n_i)$	normal unit vector
$\boldsymbol{q}$	heat flux vector
$\boldsymbol{x}(x_i)$	position vector
AL	aluminum alloy
D	diameter
D_m	average diameter of pebbles
E	Young's modulus

E^*	equivalent Young's modulus
W_a	absorbed energy
F	force
F_ave	average contact force
F_c	crush load
G	shear modulus
G^*	equivalent shear modulus
K_Ic	fracture toughness
N	(1) the number of pebbles in pebble beds
	(2) the number of crushed pebbles in crush tests
N_c	coordination number
N_f	the number of crushed pebbles in pebble beds
P_a	cumulative distribution function (CDF) of flaw size
P_c	CDF of critical flaw size of particles
P_e	CDF of contact force or energy
P_f	CDF of failure of particles
P_s	CDF of strength of single particles
PF	packing factor
R	radius
R^*	radius of the relative curvature of two contacting bodies
R_a	radius of contact circle
S	surface area
T	temperature
V	volume
W	work or energy
W_c	critical energy of pebbles
W_a	strain energy absorbed by pebbles
WC	tungsten carbide
Z	total flaw number
$\boldsymbol{F}(F_i)$	force vector
$\mathbf{I}$	identity matrix
$\boldsymbol{L}(L_i)$	periodic length vector

Greek Symbols

Contents

Index

Chapter 1
Introduction

Lithium-based ceramic pebbles are foreseen to be utilized in the solid breeder blanket, i.e., the helium cooled pebble bed (HCPB) blanket, in fusion reactors as tritium breeder. These pebbles will have to sustain severe thermomechanical loads because of high temperature and neutron fluence. As a result, the pebbles may fail and the thermomechanical response of the pebble bed will be subsequently modified. Furthermore, the integrity of these pebbles will greatly affect the functionality of the pebble bed, such as heat transfer, which will in turn influence the internal temperature. Therefore, thermomechanical analysis of these pebbles plays an important role in the design, characterization and diagnostics of the solid breeder blanket. In this chapter the background is first introduced. Then the motivation, present research activities and objectives are discussed. Finally, a brief description of the chapters is given.

1.1 Background

1.1.1 Nuclear fusion

Nuclear fusion power is one of the most promising solutions for the growing energy demand. Fusion of deuterium with tritium releases a large amount of energy according to

$$_1^2\text{D} + {}_1^3\text{T} \rightarrow {}_2^4\text{He} + {}_0^1\text{n} + 17.6 \text{ MeV} , \tag{1.1}$$

where D and T, namely deuterium and tritium, are isotopes of hydrogen. Comparing to traditional energy powers fusion has many advantages. First of all, fusion has an almost limitless fuel supply. Deuterium, a stable isotope of hydrogen, is abundant and can be easily extracted from see water. Although tritium is an unstable isotope of hydrogen, it can be readily produced from lithium which also has a great natural abundance. Besides, fusion does not produce greenhouse gas emissions or any long-term radioactive waste. It is in principle environmentally friendly. Moreover, since radioactive tritium fuel has to be produced within a fusion reactor, i.e., tritium breeding, no transport of radioactive materials is required for continuous operation. Finally, as fusion has no chain reaction like fission, it can be controlled inherently and hence is safe for the operation of reactors.

Tritium breeding from lithium (Li) is required for self-efficient fusion reaction. It can be obtained through the reactions

$$
\begin{aligned}
{}_{0}^{1}\text{n} + {}_{3}^{6}\text{Li} &\rightarrow {}_{2}^{4}\text{He} + {}_{1}^{3}\text{T} + 4.8 \text{ MeV} \\
{}_{0}^{1}\text{n} + {}_{3}^{7}\text{Li} &\rightarrow {}_{2}^{4}\text{He} + {}_{1}^{3}\text{T} + {}_{0}^{1}\text{n} - 2.5 \text{ MeV} .
\end{aligned}
\tag{1.2}
$$
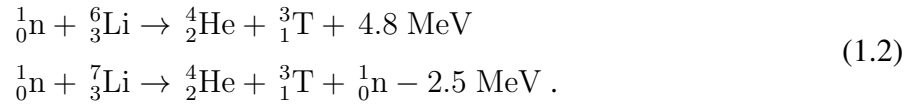
Eq. (1.2) shows that the reaction with ${}_{3}^{6}\text{Li}$ is exothermic while it is endothermic for ${}_{3}^{7}\text{Li}$. The consumed neutrons are from the outcome of the D-T reaction in Eq. (1.1). It is required that the tritium breeding ratio (TBR), defined as the ratio of the generated T to the consumed T, be at least greater than unity for self-sufficient fueling (Übeyli, 2003). To achieve this goal, more neutrons are desired. The concept of a neutron multiplier is thus introduced in the next section.
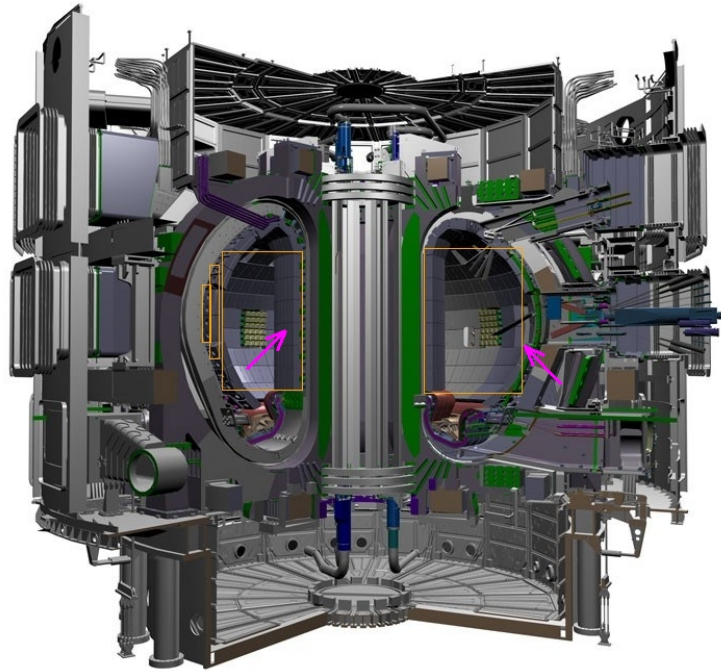
Figure 1.1: ITER machine.

1.1.2 Blanket concept

The blanket facing the hot plasma directly is one of the most important components in the Internal Thermonuclear Experimental Reactor (ITER), which is based on the tokamak concept of magnetic confinement (Fig. 1.1). The blanket has three main functions: shielding of vacuum vessel, transferring neutron kinetic energy to heat energy and breeding tritium. As for the tritium breeding, both tritium breeder and neutron multiplier have to be utilized in blankets. Lithium is to be used as tritium breeder while lead (Pb) and beryllium (Be) can be used as neutron multiplier. Two different blanket concepts are currently being developed in the European Union. One is the helium cooled lithium lead (HCLL) blanket and the other is the HCPB blanket (Giancarli et al.,

2000; Poitevin et al., 2005). In the HCLL blanket, the eutectic Pb-15.7Li liquid metal is utilized as both breeder and multiplier. Its main advantage is no breeder damage or swelling comparing to the HCPB blanket. There are two disadvantages of the liquid metal. Firstly, the generated tritium is hard to be extracted because of its high solubility of tritium. Secondly, it has strong reaction with air and water and can corrode structure materials. In the HCPB blanket, there are two kinds of pebbles: beryllium neutron multiplier and lithium tritium breeder. The thermome-chanical properties of these pebbles are consequently of concern. Test blanket modules (TBMs), namely HCLL-TBM and HCPB-TBM, based on the both concepts developed in the European breeding blanket R&D will be tested in ITER (Boccaccini et al., 2009). They are going to share a common box with an external dimension of 484 mm (toroidal) × 1660 mm (poloidal) × ∼ 700 mm (radial). The HCPB-TBM structure is shown in Fig. 1.2. Apart from stiffening grids (SGs), first wall (FW) and caps, its main element is the breeder unit (BU). BU for HCPB-TBM contains the pebbles and has the tritium breeding function. One of the BUs is shown in Fig. 1.3. The next section will give details of BU.
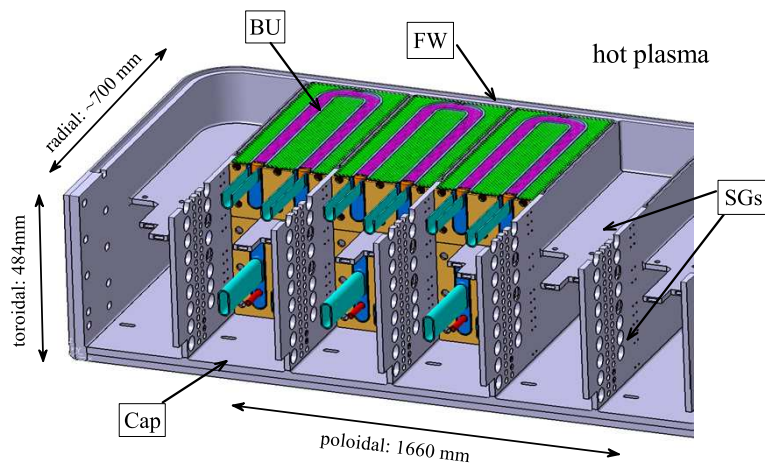
Figure 1.2: HCPB-TBM structure.

1.1.3 HCPB breeder unit

As shown in Fig. 1.3, there are several layers in the BU with a dimension of 206.5 mm (toroidal) × ∼ 190 mm (poloidal) × 400 mm (radial). Beryllium and lithium pebble beds are packed alternately inside. Two competitive tritium breeders are lithium orthosilicate (Li_4SiO_4) and lithium metatitanate (Li_2TiO_3). Helium gas will be slowly purged into the pebble beds so as to bring the generated tritium fuel away. At the same time, helium gas, with a pressure of 8 MPa, inside cooling plates takes the generated heat away. The maximum allowable design temperature for breeder and multiplier is 917^oC and 655^oC, respectively. A TBR of 1.14 can be achieved with a radial length of 460 mm. Comparing to the radial dimension of the TBM box, the remaining

space can be used for further optimization of HCPB-TBM design (Poitevin et al., 2005).
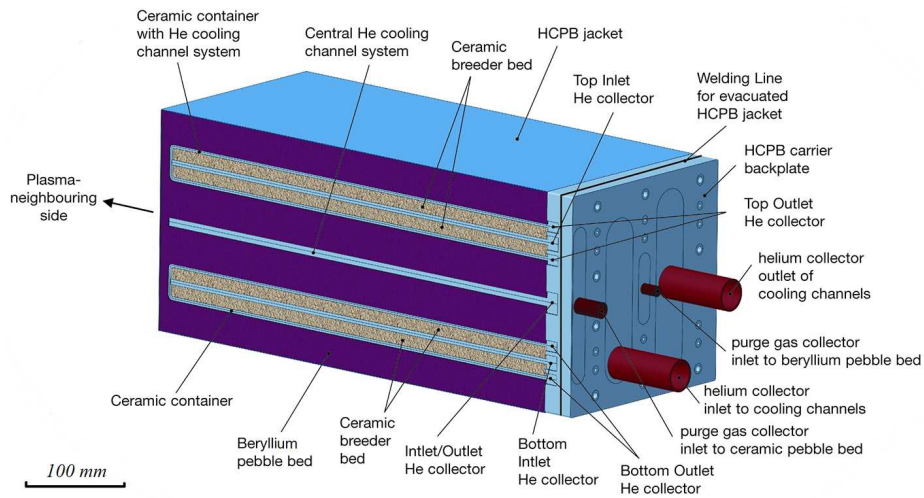
Figure 1.3: BU for the HCPB-TBM.

The Li_4SiO_4 pebbles with diameters ranging from 0.25 to 0.63 mm are produced with melt-spraying method (Knitter et al., 2007). Most of the pebbles have good spherical shape. The competitor, Li_2TiO_3, is produced through wet process. Due to the fabrication process the Li_2TiO_3 pebbles deviate from the spherical shape and tend to be ellipsoidal shape. The size ranges from 0.2 to 2 mm (Tsuchiya et al., 2005; van der Laan and Muis, 1999). The appearance of both pebbles was examined by Knitter (2003). Figure 1.4 shows the results for Li_4SiO_4 pebbles produced by Schott Germany and Li_2TiO_3 pebbles produced by CEA France.
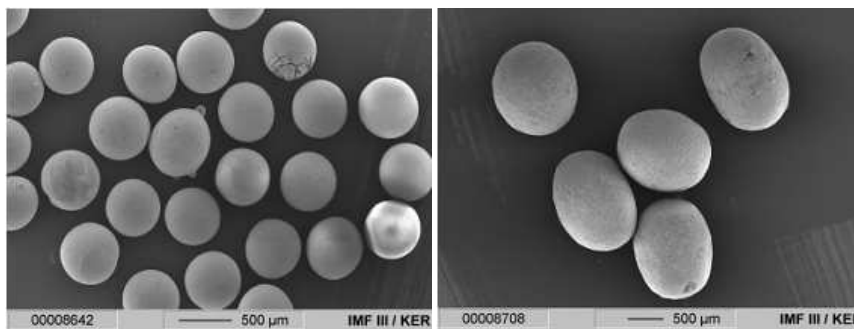
Figure 1.4: Appearance of Li_4SiO_4 pebbles produced by Schott, Germany (left) and Li_2TiO_3 pebbles produced by CEA, France (right).

1.2 Motivation

The ceramic breeders in the form of pebbles are subject to high heat flux and neutron load in fusion reactors. The thermal expansion of structure materials like the cooling plate will change

the volume of pebble beds. Meanwhile, the pebble volume expands due to the heat flux and neutron-induced swelling. The expansion will be hindered by the container of the BU. As a result, this leads to high contact forces between pebbles, and pebbles might fail. The failure of pebbles will in turn influence the macroscopic response of pebble beds. Therefore, it is essential to study the macroscopic behavior of pebble beds in the view of micromechanics under fusion relevant conditions.

The macroscopic behavior of pebble beds subjected to combined effects of temperature, deformation and swelling is of concern. It can be studied either by continuum mechanics, such as adoption of phenomenological models, or by discrete element method (DEM). With the latter method, the response for each pebble can be monitored, e.g., the failure of single pebbles. The failure of pebbles leads to two main consequences. Firstly, the fragments may block the flow of the purge gas. If the purge gas was totally blocked, there would be no tritium extraction. For the same consideration, the helium gas is slowly purged so that no pebbles will flow away and block the gas evacuation. Secondly, it has an influence on local and global thermal conductivity. The thermal conductivity of pebble beds inherently depends on the contacts between pebbles, such as coordination number N_c and the size of each contact area. The failure of pebbles will obviously change both of them.

In this thesis, DEM will be adopted to study the thermomechanical behavior of ceramic pebbles. Before any analysis with DEM, it is important to take advantage of existing experimental data, and subsequently to assign to pebbles rational parameters. Besides, since there are some input parameters in DEM that are hard to identify, such as the friction coefficient between pebbles, it is necessary to carry out parameter study to check their influence on DEM simulations. After that DEM can be taken as a predictive tool for the design and analysis for ceramic pebble beds in HCPB blankets.

1.3 Present research activities

Much effort has been made on the thermomechanical properties of pebbles and pebble beds. Various experiments can supply the essential information required in DEM. The experimental results can be used to verify the numerical results as well. There have already been some DEM models to study the thermomechanical behavior of pebble beds. In the following the present research activities, including experiments and modellings, are introduced.

1.3.1 Experiments

The experiments for ceramics pebbles contain two aspects: single pebble characterization and pebble bed characterization. The characterization of single pebbles includes mechanical and

thermal properties of bulk materials, microstructure, pebble size distribution, density, porosity, chemical and phase analysis and crush loads. Characterization of pebble beds includes Young's modulus of pebble beds, macroscopic plasticity, creep, thermal conductivity, heat transfer coefficient, packing factor (PF) and topology. Compression tests of pebble beds are commonly used to study the mechanical and thermal behavior under various external excitations. A comprehensive database for pebbles and pebble beds is given by Reimann et al. (2005).

There are three states of each kind of pebbles: as-received, annealed or conditioned, and irradiated. The characterization of single ceramic pebbles under various states has been performed by Knitter and Alm (2005); Knitter et al. (2007); Piazza et al. (2001b), which includes, for example, pebble size, porosity and crush load. The crush load of single pebbles is obtained in crush tests, e.g., single pebbles are crushed by two parallel plates. The crush load characterizes the strength of single pebbles. It varies with batches, environments, and plates. The crush load is 5.9 ± 1.1 N for dried Li_4SiO_4 pebbles from the OSi 07/1 batch crushed by BK7 glass plates (Löbbecke and Knitter, 2007).

For the bulk material, the mechanical properties, such as Young's modulus and Poisson's ratio, have been widely studied, e.g., Chu et al. (1989); Dienst and Zimmermann (1988); Johnson et al. (1988); Vollath et al. (1990). Young's modulus for each breeder material decreases with increasing temperature. Major thermal properties comprise of thermal expansion coefficient, thermal conductivity and heat transfer coefficient. The thermal expansion coefficients for various breeder materials of temperature dependence have been studied by Billone et al. (1993); Dienst and Zimmermann (1988). Abou-Sena et al. (2005) summarized the experimental results for temperature-dependent thermal conductivity for several breeder materials. The thermal conductivity of both Li_4SiO_4 and Li_2TiO_3 remains around 3.2 W/mK at room temperature and decreases to some extent with increasing temperature. Finally, irradiation-induced swelling of ceramic pebbles is studied by Johnson et al. (1988). Few post-irradiation tests for ceramic pebbles are performed, e.g., Piazza et al. (2004).

Compression tests of pebble beds are commonly used to study the mechanical and thermal behavior under various external excitations. The macroscopic stress-strain relation of pebble beds with various parameters, such as temperature, can be obtained from uniaxial compression tests (UCTs, or oedometric compression). Nonlinear elasticity, overall plastic deformation and hardening are typical observations in UCTs (Reimann et al., 2000). The stress-dependent Young's modulus is derived from the loading or unloading curve (Piazza et al., 2002; Reimann et al., 2002a). The macroscopic plasticity is measured when the external load is totally removed. Creep can be seen at different temperature and stress levels. The correlations of creep properties of Li_4SiO_4 and Li_2TiO_3 pebble beds are obtained by Reimann and Wörner (2000, 2001); Reimann et al. (2002b). Some biaxial or triaxial compression tests are available in literature (Hermsmeyer and Reimann, 2002; Piazza et al., 2002; Zaccari and Aquaro, 2009), which provide additional

information, such as the inner friction angle of beds. Some compression tests have shown the influence of pebble bed dimensions and filling factor as well (Hermsmeyer and Reimann, 2002; Reimann et al., 2003). Using a shallow bed, i.e., the bed height is small compared to other bed dimensions, can efficiently minimize the influence of wall friction.

Thermal conductivity of pebble beds is one of the most important design parameters. It depends not only on the average temperature but also on the contacts between pebbles. Thermal conductivity is investigated as a function of temperature, e.g., Dell'Orco et al. (2004); Piazza et al. (2001a) or macroscopic strain, e.g., Aquaro (2003); Piazza et al. (2002) or macroscopic stress, e.g., Aquaro and Zaccari (2006, 2007). It is also investigated as a function of stress and strain, e.g., Reimann and Hermsmeyer (2002) or temperature and strain, e.g. Tanigawa et al. (2005). Abou-Sena et al. (2005) summarized the experimental results of temperature-dependent thermal conductivity for various ceramic pebble beds. The stress- or strain- dependent thermal conductivity is usually measured in UCTs. This relation depends on many internal factors, such as the PF. Therefore, it will be helpful to show the thermal conductivity with respect to stress and strain at the same time (Reimann and Hermsmeyer, 2002).

The heat transfer coefficient between pebble beds and the container wall is also important, especially in the thermal analysis of pebble beds. Some experimental investigations have been carried out for ceramic pebbles (Dalle Donne and Sordon, 1990; Tehranian and Abdou, 1995; Tehranian et al., 1994).

Another issue related to pebble beds is their topology. The topology of aluminum sphere assembly with and without compression has been recently investigated (Reimann et al., 2006, 2008). The results clearly showed the influence of the container wall on the position distribution of spheres. The contact coordination number N_c, poloidal angle and contact surface ratio were also examined. All the results give an insight into the topology of pebble beds. DEM needs initial configuration of pebbles, such as position distribution, which plays an important role in DEM simulations. The method to obtain the initial configuration for DEM can be verified by these experimental results.

1.3.2 Modeling

Pebble beds can be modeled by DEM due to the similarity to sand and soil. This method has first been introduced by Cundall and Strack (1979). DEM can be used to simulate a wide variety of granular flow and rock mechanics situations. Its applicability is verified by experimental results in a wide range of engineering applications. It can also supply more detailed internal information in granular assembly than physical experiments. For example, the force chains developed in a granular assembly can be visualized with DEM, e.g., Gilabert et al. (2007), while this is nearly impossible in experiments with a large number of small particles. The main disadvantage is the

maximum number of particles which is limited by computational power.

Pebble beds comprise of numerous discrete pebbles which form a granular material. Some common characteristics of granular materials are a) nearly rate-independent plastic deformation and yield stress; b) strong pressure-dependent hardening or softening; c) the dilatancy under shear stress. Hydrostatic pressure can give rise to irreversible volume change and such change can either harden or soften the granular assembly. When the assembly is sheared, shear bands due to bulk expansion are commonly observed (Mooney et al., 1998; Oda et al., 1998). The micro-deformation mechanism leading to the development of shear bands is not yet well understood. The overall plastic or inelastic deformation of granular assemblies arises from the plastic deformation of the particle contacts and the rearrangement of particles. Moreover, the thermal properties, such as effective thermal conductivity and thermal expansion of pebble beds, depend heavily on the packing structure and force chains in the granular assembly (Jaeger et al., 1996).

There are several models based on DEM to study the thermomechanical behavior of pebble beds. Thermal creep of ceramic breeder pebble beds is investigated with a three dimensional thermomechanics code (Lu et al., 2000; Ying et al., 2002). An et al. (2007a,b) investigated the contact force distribution inside pebble beds. In these studies, all the pebbles are randomly packed into a structure and the initial PF is about 60±0.5% which is smaller than the reference value for fusion (around 63%). Besides, the wall influence is not negligible since there are only thousands of spheres in their simulations. An alternative choice to avoid wall influence is to utilize periodic boundary condition (Gan and Kamlah, 2010). Other researchers simplify the pebbles in regular lattices as beam elements (Aquaro and Zaccari, 2005, 2006), which represent the interaction forces between pebbles. By using such regular lattices, analytical solutions can be obtained, and the initial PF can be varied by using different types of lattices. However, this method cannot incorporate the rearrangement of particles, which is also an important factor for the overall plastic strains of the assembly.

Recently, a DEM code for pebble beds has been developed (Gan, 2008; Gan and Kamlah, 2010) at Karlsruhe Institute of Technology (KIT). It has the following main features: a) pebbles are modeled as mono-sized or multi-sized spheres; b) periodic boundary conditions are used; c) a high PF comparable to the reference value is realized. With the periodic boundary condition, the properties of the bulk region of the pebble bed can be obtained by a relatively small number of pebbles and there is no wall influence at all. The PF is related to the initial configuration of spheres, which is generated with the algorithm proposed by Jodrey and Tory (1985). Because the PF is an important factor affecting the overall thermomechanical behavior of pebbles beds, it is essential to use the reference PF. Mechanical load can be controlled by either macroscopic stress or macroscopic strain. The average stress tensor is obtained from either local or global coordinates. Consequently, the macroscopic stress-strain relation can be derived under various excitations. The influence of pebble failure can be also included.

Engineering applications of DEM into large scale structures, such as the HCPB-TBM, will not be practical without the help of continuum modeling. There are also some phenomenological models based on the continuum mechanics to study the behavior of pebble beds (Bühler, 2002; Gan, 2008; Hofer and Kamlah, 2005; Reimann et al., 2002a). Since a micro-based phenomenological model can be in principle developed from the DEM simulation, it can be then incorporated into these phenomenological models, such as the one developed by Gan (2008); Gan and Kamlah (2007).

1.4 Objective of this work

The main objective of this work is multiscale thermomechanical modeling of ceramic pebble beds with DEM tools. The required information for DEM includes geometry and material parameters, such as contact strength, of pebble beds. They will be derived either directly from experiments or with some reasonable simplifications, e.g., spherical shape of pebbles. Moreover, the contact strength for pebbles in pebble beds will be derived from available experiments like crush tests. The contact strength has to be properly defined based on certain failure criteria and verified by experiments.

When all the parameters are derived from experiments and analysis, the analysis of failure initiation and propagation of pebbles will be performed. Thus, the influence of pebble failure on the macroscopic behavior of pebble beds can be studied. Moreover, the macroscopic stress-strain relation of pebble beds with increasing temperature will be analyzed as well. Finally, the average thermal conductivity of pebble beds is calculated according to the contact information derived from DEM simulations.

1.5 Overview of the following chapters

Crush tests of Li_4SiO_4 pebbles were carried out to study the plate influence on the crush load. The results and discussion are shown in Chapter 2. According to the experimental results, a failure model is sought to characterize the plate influence. However, the pebbles in pebble beds have normally more than two contacts while there are only two contacts in crush tests. Therefore, Chapter 3 shows the stresses in a sphere subjected to various loads. The analytical solution enables to make use of any stress-based failure model in principle. Some failure models based on various failure criteria are shown in Chapter 4. A modified failure model based on energy criterion is found to be applicable to explain the plate influence. Moreover, the underlying reasons for the applicability of this model are discussed as well. Before DEM simulations, the shear stiffness, a parameter in the linear tangential contact model, is derived from another analytical tangential contact model. Its influence on the macroscopic stress-strain relation is shown in Chapter 5. The

implementation of pebble strength into DEM is shown in Chapter 6. First of all, each pebble is assigned to a unique strength in terms of critical energy above which the pebble will fail. Thus, the initiation of pebble failure can be studied. The propagation of pebble failure is also shown in Chapter 6. It is of concern that when the macroscopic stress-strain relation is influenced by the crushed pebbles. In Chapter 7, an analysis is performed for the thermal properties, such as thermal expansion and thermal conductivity. Finally, a summary of this work is given in Chapter 8.

Chapter 2
Crush tests

The thermomechanical behavior of pebble beds can be studied through DEM in principle. Pebble geometry and material parameters, such as Young's modulus, Poisson's ratio and contact strength, are input parameters in DEM. Various experiments have been performed to supply these parameters. For example, the properties of bulk material for some ceramic pebbles have been derived from experiments by Chu et al. (1989); Dienst and Zimmermann (1988); Johnson et al. (1988); Vollath et al. (1990). Many crush tests for ceramic pebbles have been performed to characterize the contact strength of pebbles in terms of crush load, i.e., the maximum contact force at which the pebbles fail (Piazza et al., 2001b; Schumacher et al., 1988; Tsuchiya et al., 2006; Zaccari and Aquaro, 2007). However, unlike the bulk material parameters which can be implemented into DEM directly, the crush load from crush tests cannot be simply imported as the pebble strength in DEM. At first, in pebble beds there are pebble-pebble contacts while there are plate-pebble contacts in crush tests; they are different forms of contact. It is very hard, if not impossible, to carry out experiments as pebble-pebble contacts. Secondly, the strength of pebbles is based on certain failure criteria, such as critical stress or critical energy criterion. Any failure criterion that will be adopted should be validated by experiments. When the failure criterion for pebbles is identified, the crush load from crush tests can be converted to the pebble-pebble contact strength. Subsequently, the derived strength can be implemented in DEM.

When pebbles are simplified as mono-sized spheres and friction is ignored, the pebble-pebble contact reduces to a contact between a sphere and a rigid plate. Compared to the plate-pebble contact in crush tests the only difference is the stiffness of the plates. That is, the crush load for pebble-pebble contacts can be predicted when the plate influence is known. The crush load also depends on experimental environments. For example, the crush load of Li_4SiO_4 pebbles varies when crushed in air and in dry inert gas. The pebbles in air tend to be a slightly tougher (Knitter, 2010). As it is known that Li_4SiO_4 can easily take up moisture and carbon dioxide (CO_2) from air (Kato et al., 2002), it is speculated that the pebbles in air react with water and CO_2 and thus enhance their strength. As this effect is difficult to be quantitatively described, the environment of crush tests should be as close as possible to the fusion relevant environment. Furthermore, it is found that the mean crush loads are different to some extent for pebbles from different batches (Knitter, 2004; Löbbecke and Knitter, 2007, 2009). Therefore, pebbles from the same batch will

be used in experiments, analyzed in simulation and utilized in HCPB-TBM.

This chapter reports about the crush tests for single Li_4SiO_4 pebbles performed to study the plate influence on the crush load; the geometry of the pebbles is also examined. Moreover, the pebbles were monitored by a microscope during loading so that the forms of pebble failure can be recorded. This helps finding the suitable failure criterion.

2.1 Experimental tests

Crush tests are usually performed to characterize the strength of single ceramic pebbles (Piazza et al., 2001b; Schumacher et al., 1988; Tsuchiya et al., 2006; Zaccari and Aquaro, 2007). However, there are some common issues for these tests. Firstly, few crush load results are given in terms of distributions. The crush load has a big scatter due to the ceramic characteristic of the pebbles. Although the scatter of the crush load is well known and thus many pebbles are crushed in one crush test, only the mean crush load, sometimes together with the standard deviation, is provided. This will omit some information compared to the complete crush load distribution. Secondly, different plates are used to crush pebbles. For example, Löbbecke and Knitter (2007) took BK7 glass as plates in order to avoid plastic deformation of the plates while Zaccari and Aquaro (2007) took nickel alloy as plates. Consequently, different crush loads would be obtained even if the same pebbles were used in both tests. Finally, as previously mentioned the environment, e.g., air or dry inert gas, can also affect the crush load. Therefore, in order to study the plate influence on the crush load, crush tests should be performed with exactly the same conditions, i.e., the same pebbles in the same environment, except for the plates. The crush load distribution should be shown instead of simply the mean value.

In this work, crush tests were carried out with two different plates, which were made of aluminum alloy (AL) and tungsten carbide (WC), respectively. The plates were selected in view of their different stiffnesses so that there would be a significant difference between their crush load distributions. Conditioned Li_4SiO_4 pebbles from the batch OSi 07/1 were crushed for both plates in air. Before tests, these pebbles were exposed in air for some days so that there was enough time for pebbles to react with moisture and CO_2 in air. Consequently, the difference between the crush load distributions solely stems from the plate. Note that the experimental environment is different from that in fusion reactors. The results in this work do not characterize the pebble strength in fusion relevant conditions.

Some material parameters are listed in Table 2.1, including for the BK7 glass plates used in the crush tests at the Fusion Material Lab (FML), KIT. The crush tests at FML for a purpose of quality control are performed in dry inert gas. The environment at FML is similar to fusion reactors except that it is at room temperature. Thus, once the plate influence can be quantitatively described, the crush load from FML will be used to predict the pebble-pebble contact strength

Table 2.1: Material parameters of Li_4SiO_4 pebbles and the plates.

Materials	Young's modulus (GPa)	Poisson's ratio	Yield stress (MPa)
Li_4SiO_4	90*	0.25**	-
WC	732	0.22	2000
AL	70	0.33	500
BK7	82	0.206	-

* From Ref. Gan (2008); ** From Ref. Vollath et al. (1990).

under fusion relevant conditions. It is noted that the stiffness of AL is similar to BK7. The difference between their crush loads for the same pebbles should mainly arise from the different experimental environment.
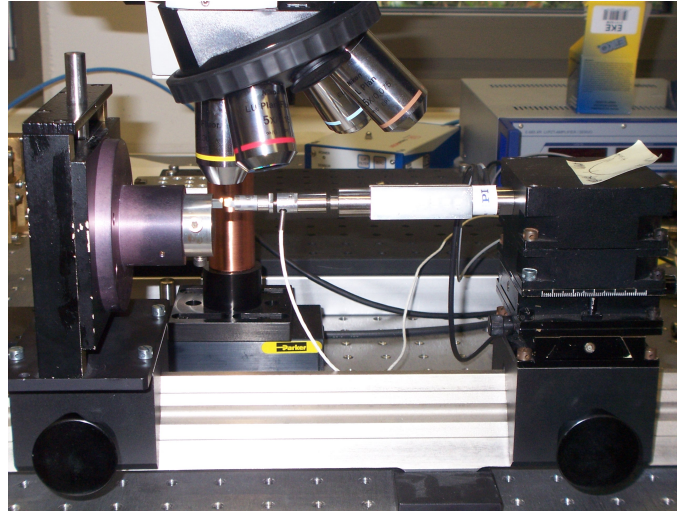
Figure 2.1: Experimental apparatus for single Li_4SiO_4 pebbles for different plates in air.

The experimental apparatus is shown in Fig. 2.1. The pebbles were placed on the plate on the left side under the microscope. The microscope was used to check the geometry, i.e., shape and size, of pebbles and the failure form. The plate on the left side was fixed. The one on the right side moved horizontally towards the pebble until it failed. The approach velocity was as slow as 0.015 mm/min. The displacement of the right plate and the reaction force were recorded during loading. As a ceramic material, the failure of pebbles is spontaneous and the crush load can be easily identified.

The crush load probability for $F_c \leqslant F_{ci}$ is $P_s(F_{ci}) = i/(N+1)$ where F_c denotes the crush load. All crush loads $F_{ci}(i = 1, 2, \cdots, N)$ obtained in experiment are ranked in an increasing order, namely $F_{c1} \leqslant F_{c2} \leqslant \cdots F_{ci} \cdots \leqslant F_{cN}$, where N is the total number of crushed pebbles. Two crush load distributions for each type of plates are thus derived from this work. The Weibull

distribution is used to fit the experimental data, that is

$$
P_{\rm s} = \begin{cases} 1 - \exp\left[-\left(\frac{F_c - F_u}{F_0} \right)^m \right] & F_c \geqslant F_u \\ 0 & F < F_u \,, \end{cases}
\tag{2.1}
$$

where F_u, F_0 and the Weibull modulus m are fitting parameters. Finally, the crush load distribution for each type of plates obtained from FML for conditioned pebbles from the same batch, namely OSi 07/1, is also given in this chapter.

2.2 Experimental results
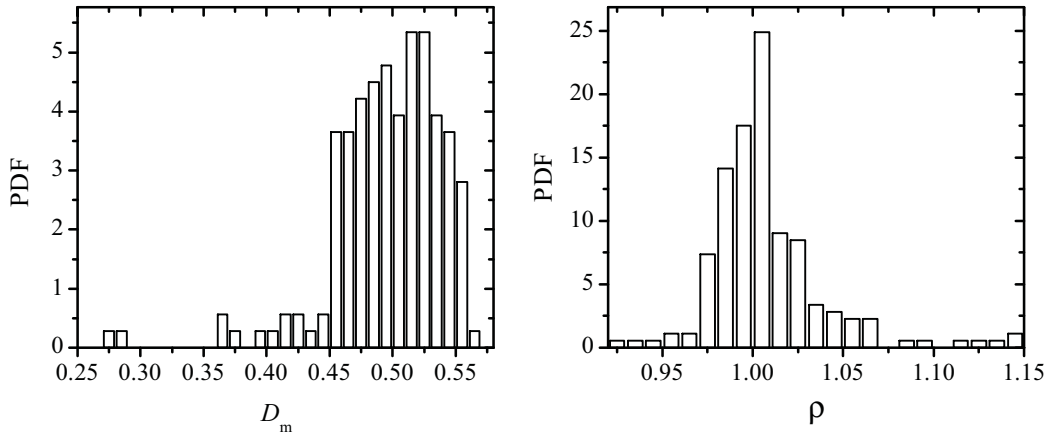
Figure 2.2: Characterization of Li$_4$SiO$_4$ pebble geometry. Left: pebble size distribution; right: pebble shape distribution.

The appearance of pebbles was examined by microscope. The probability density functions (PDF) of the size and shape are shown in Fig. 2.2. The size is characterized by an average diameter, namely $D_{\rm m} = (H + W)/2$, while the shape is characterized by $\rho = H/W$, where H and W is the hight and width, respectively, measured from the pebble picture taken before crush tests. As seen in Fig. 2.2, most pebbles have a size in the range of $0.44 < D_{\rm m} < 0.56$ mm, and most pebbles have a good sphericity since most data are around $\rho = 1$.

The size distribution is quite different from the one obtained by Löbbecke and Knitter (2007) although both pebbles are from the same batch. The reason is that sieved pebbles were used in this work, while as-received pebbles were measured by Löbbecke and Knitter (2007). The sieved, or selected, pebbles should have a size of $0.5 < D_{\rm m} < 0.56$ mm according the hole size of the stacked sieves. Anyhow, nearly half of the pebbles which were randomly chosen in this work had a size smaller than 0.5 mm. This indicates a certain inefficiency of the sieving method. Note that the pebbles with a nominal size of 0.5 mm crushed at FML were prepared in the same way. The geometry of pebbles was thus statistically the same as used in this work.

As for the pebble shape, the good sphericity of most pebbles conforms to the examination by Löbbecke and Knitter (2007). The sphericity of Li_4SiO_4 pebbles is much better than that for Li_2TiO_3 produced by CEA (Fig. 1.4). The Li_4SiO_4 pebbles can be accordingly represented by spheres in DEM. They could be mono-sized or multi-sized spheres. If multi-sized spheres are implemented in DEM, the sphere sizes should satisfy the distribution in Fig. 2.2 or that examined by Löbbecke and Knitter (2007).
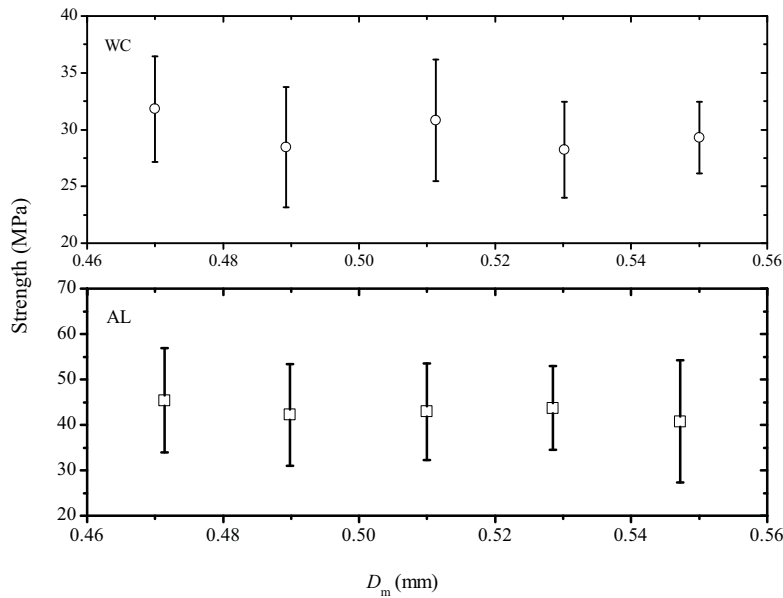
Figure 2.3: Size effect of the contact strength F_c/D_m^2.

Figure 2.3 shows the size effect of the contact strength. The pebbles with a size of $0.44 < D_m < 0.56$ mm are divided into five groups according to their sizes. The number of pebbles in each group is between 10 and 20. The strength in this chapter is defined as F_c/D_m^2, which is usually taken as the characteristic stress for the failure of brittle spheres, e.g., McDowell and Amon (2000). The size effect describes the volume influence on the crush load. For example, if critical flaws dominate the failure of pebbles, and assuming the flaw size distribution is independent of the volume, the strength will depend on the volume, i.e., the contact strength decreases while pebble size increases. The contact strength is calculated for each pebble. The mean value and standard deviation are derived with these strengths for each group. The mean size of pebbles for each group is taken as the corresponding D_m in Fig. 2.3. For both plates, it shows that the presence of a size effect, at least within this size range, is not clear. Thus, it is doubtful that the failure is dominated by critical flaws inside pebbles.

Figure 2.4 shows the crush load distributions where the size difference is ignored. Clearly seen is the significant influence of the plates. Table 2.2 lists additional information of these tests including the one performed at FML (Rolli, 2008). The crush load distribution at FML is shown in Fig. 2.5. As previously mentioned, the crush load difference between AL and BK7 plates is
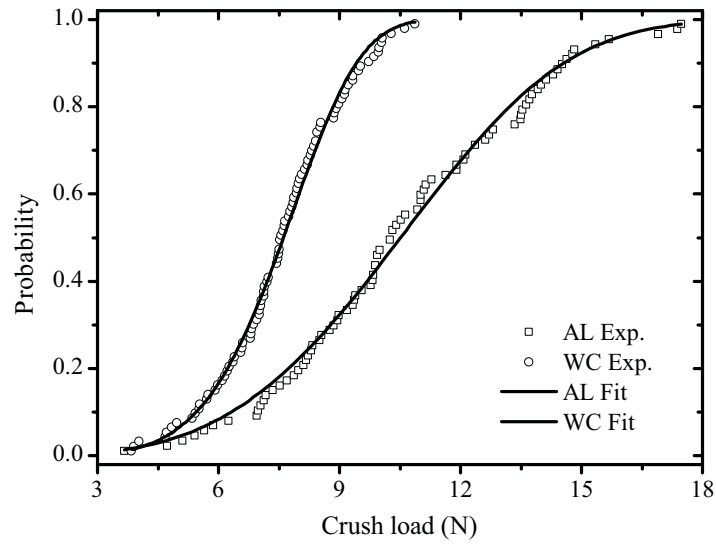
Figure 2.4: Crush load distributions for single Li_4SiO_4 pebbles in air.

Table 2.2: Information for these crush tests.

Plates	N	F_c (N)*	(F_u, F_0, m)**	Environment
WC	92	7.55 ± 1.55	(2.23,5.88,3.97)	air
AL	86	10.6 ± 3.02	(3.67,7.87,2.39)	air
BK7	200	5.88 ± 1.14	(3.03,3.18,2.50)	dry inert gas

* Mean value plus standard deviation; ** Fitting parameters.
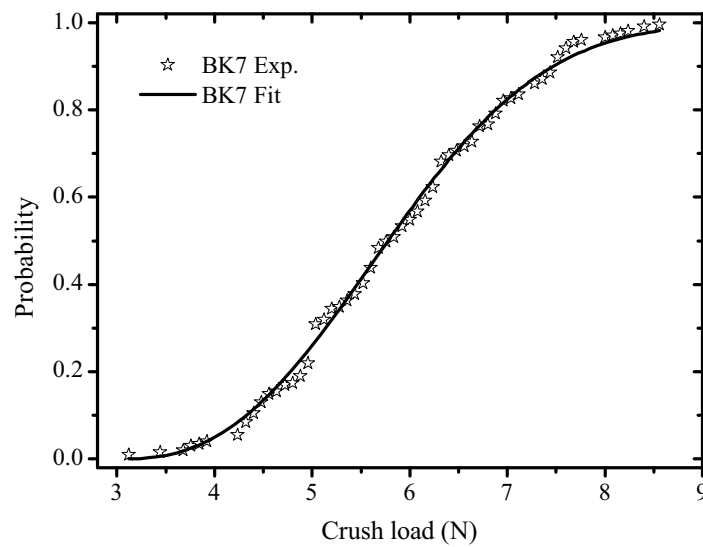
Figure 2.5: Crush load distribution for single Li_4SiO_4 pebbles in dry inert gas at FML.

mainly due to the experimental environment. These two crush load distributions show that the strength of pebbles becomes much higher for pebbles crushed in air than in dry inert gas, which is accordance with the findings by Knitter (2010).

Finally, some typical forms of failure are shown in Fig. 2.6. It is found that most pebbles failed spontaneously. It is hard to identify where failure started. Besides, there are several distinct failure forms, which indicates the underlying complicate failure mechanism. For most pebbles, as soon as failure occurred, all or part of the fragments of pebbles were ejected from the apparatus making any post failure investigation impossible. Certain fragments sometimes stayed on the plates, e.g., the first image in Fig. 2.6. On the other hand, some pebbles, after the first time failure when there was a jump of the contact force, could still sustain some load. In such cases, the pebbles broke into two or more parts, e.g., the upper right and lower left images in Fig. 2.6. The failure possibly originates from the contact points. However, the last image shows that the failure of this pebble does not start from the lower contact point.
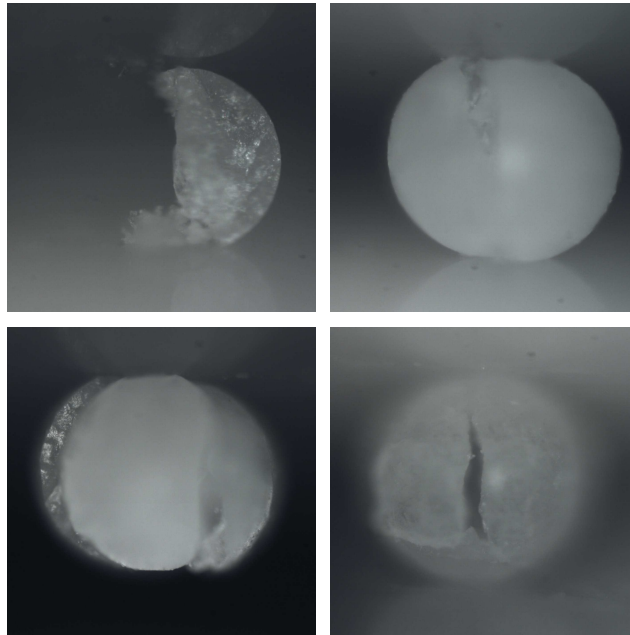
Figure 2.6: Some failure forms of Li_4SiO_4 pebbles.

2.3 Discussion

The geometry including size and shape of Li_4SiO_4 pebbles was examined. It offers important information not only for the initial configuration in DEM but also for the failure criterion analysis. As for the failure criterion of single pebbles, pebbles can be simplified as spheres, which significantly reduces the complexity for the analysis. This simplification is reasonable for Li_4SiO_4 pebbles. However, such a simplification may not be suitable for Li_2TiO_3 pebbles because of

their ellipsoidal shape. Consequently, spheres can represent the Li_4SiO_4 pebbles while ellipsoids should be used to represent the Li_2TiO_3 pebbles in DEM simulations.

There are two options for the pebble size in DEM, i.e., either mono size or multi size. The size selection will affect the failure criterion analysis, that is, whether the pebble strength depends on size or not. There are basically two methods to describe the pebble strength (Marketos and Bolton, 2007). One is that pebbles with the same size have a unique strength, but there is a size distribution. The other way is that mono-sized pebbles have a strength distribution. Of course, the strength could be described with the two methods at the same time, i.e., pebbles have a size distribution while there is a strength distribution for pebbles with the same size. However, this will give rise to much difficulty to study the plate influence. Moreover, as shown in Fig. 2.3 the strength seems to be size independent. Therefore, mono-sized pebbles with a strength distribution are preferred in the failure criterion analysis as well as in DEM simulations. More importantly, the failure criterion related to the contact strength must be able to explain the plate influence on the crush load. Otherwise, the contact strength could not be incorporated into DEM.

The failure starting point and subsequent propagation can reveal the potential failure criteria. For example, some fracture tests of glass spheres show that failure of those spheres starts from the contact circle (ring crack), which implies that a stress criterion dominates failure. Although the failure starting point could not be identified from the tests, the variety of failure forms implies a complicate failure mechanism for pebbles. Therefore, various models based on different criteria deserve consideration to study the plate influence.

2.4   Summary

In this chapter, crush tests for single Li_4SiO_4 pebbles were performed to quantitatively show the plate influence on the crush load. AL and WC were used as the plates on both sides, respectively. The crush loads are shown in terms of statistic distributions which can supply more information, such as the failure probability under a given contact force. The final goal is to characterize the plate influence. Subsequently, the pebble-pebble contact strength can be predicted from the crush load obtained from FML and then implemented into DEM. The size and shape distributions of pebbles were examined by microscope, which supplied the required information in DEM. Finally, some typical failure forms of pebbles are provided to support the failure criterion analysis.

Chapter 3
Stress in pebbles

In the last chapter, the crush load of single pebbles is obtained from the crush tests. We intend to make use of these data to characterize the strength of single pebbles in pebble beds. Consequently, two aspects have to be taken into account. Firstly, there is a difference between plate-pebble contacts in crush tests and pebble-pebble contacts in pebble beds, i.e., the contact forms are different. Secondly, as shown in Fig. 3.1, there are more contacts for each pebble in pebble beds (Löbbecke and Knitter, 2009) than in crush tests. For any pebble in pebble beds, the number of its neighboring pebbles in contact is defined as the coordination number N_c. These two differences necessitate the transformation of the strength derived from crush tests. On the other hand, the strength still has to be characterized by certain failure criteria. There are various failure criteria based on stress analyses (Langitan and Lawn, 1969). Nevertheless, the stresses are often derived from FEM simulation because there are few cases in which the analytical solution is known. It is very helpful if the stresses in ceramic pebbles under consideration can be analytically obtained.

In this chapter, an analytical solution for the stresses in an elastic sphere subjected to various loads is derived. The spherically isotropic sphere in equilibrium is compressed by several loads or forces along different directions, i.e., $N_c > 2$. Moreover, the body force is neglected. In each load area, the pressure along the radial direction is distributed axisymmetrically either in a uniform form or a Hertz form; stresses tangential to the surface are taken to be zero. The stresses inside the sphere are derived analytically. The numerical evaluations are validated by the Hüber-Hertz analytical solution (Hüber, 1904) and FEM simulations. Ceramic pebbles have good sphericity as found in the crush tests. Therefore, the stresses in the pebbles can be evaluated with our solution for elastic spheres.

3.1 Theory

3.1.1 Hooke's law

With the spherical coordinate system (r, θ, φ) as shown in Fig. 3.2, the relations between stress σ and strain ε components are expressed by the generalized Hooke's law for spherically isotropic
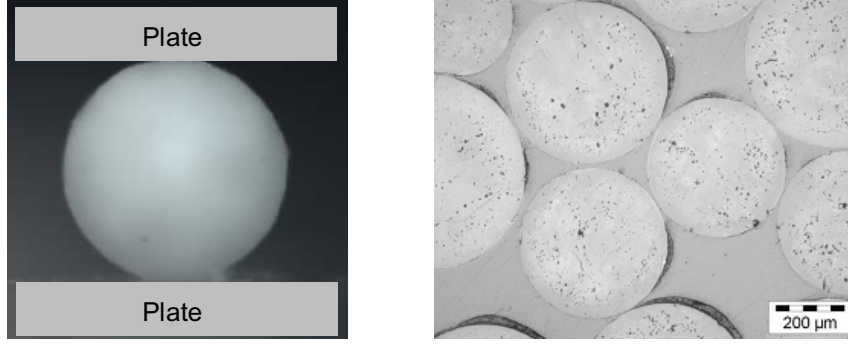
Figure 3.1: Left: crush tests for single pebbles; right: pebbles in beds.

spheres (Chau and Wei, 1999)

$$\sigma_{\theta\theta} = (2A_{66} + A_{12})\varepsilon_{\theta\theta} + A_{12}\varepsilon_{\varphi\varphi} + A_{13}\varepsilon_{rr}$$
$$\sigma_{\varphi\varphi} = A_{12}\varepsilon_{\theta\theta} + (2A_{66} + A_{12})\varepsilon_{\varphi\varphi} + A_{13}\varepsilon_{rr}$$
$$\sigma_{rr} = A_{13}(\varepsilon_{\theta\theta} + \varepsilon_{\varphi\varphi}) + A_{33}\varepsilon_{rr}$$
$$\sigma_{\theta\varphi} = 2A_{66}\varepsilon_{\theta\varphi}, \ \sigma_{r\theta} = 2A_{44}\varepsilon_{r\theta}, \ \sigma_{r\varphi} = 2A_{44}\varepsilon_{r\varphi} \,,$$

$$(3.1)$$

where

$$A_{12} = -\frac{E(\nu E' + \nu'^2 E)}{(1+\nu)\bar{E}}, \ A_{13} = -\frac{\nu' E' E}{\bar{E}}, \ A_{33} = -\frac{E'^2(1-\nu)}{\bar{E}},$$

$$(3.2)$$

$$A_{66} = \frac{E}{2(1+\nu)}, \ A_{44} = G', \ \bar{E} = E'(\nu - 1) + 2\nu'^2 E \,.$$
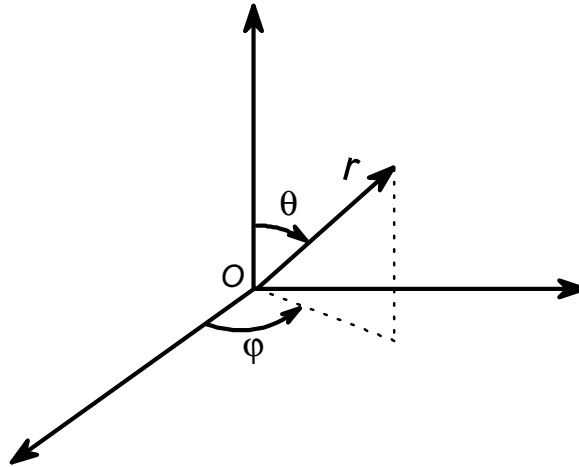
Figure 3.2: Spherical coordinate system (r, θ, φ).

E and E' are the Young's moduli governing the deformation in the isotropic plane and along

20

the direction perpendicular to it, i.e., the radial direction, respectively. The corresponding Poisson's ratios are ν and ν', respectively. G' is the shear modulus governing the shear deformation in the isotropic plane perpendicular to the radial direction. Spherical isotropy contains isotropy as a special case. For the case of isotropic material, the material parameters reduce to

$$E' = E, \quad \nu' = \nu, \quad G' = \frac{E}{2(1+\nu)} \,. \tag{3.3}$$

The relations between small strain ε, and small deformation u, are expressed as

$$
\begin{aligned}
&\varepsilon_{rr} = \frac{\partial u_r}{\partial r}, \ \varepsilon_{\theta\theta} = \frac{1}{r}\frac{\partial u_\theta}{\partial \theta} + \frac{u_r}{r}, \ \varepsilon_{\varphi\varphi} = \frac{1}{r\sin\theta}\frac{\partial u_\varphi}{\partial \varphi} + \frac{u_r}{r} + \frac{u_\theta}{r}\cot\theta \\
&\varepsilon_{r\varphi} = \frac{1}{2}\left(\frac{1}{r\sin\theta}\frac{\partial u_r}{\partial \varphi} - \frac{u_\varphi}{r} + \frac{\partial u_\varphi}{\partial r}\right), \ \varepsilon_{r\theta} = \frac{1}{2}\left(\frac{1}{r}\frac{\partial u_r}{\partial \theta} - \frac{u_\theta}{r} + \frac{\partial u_\theta}{\partial r}\right) \\
&\varepsilon_{\theta\varphi} = \frac{1}{2}\left(\frac{1}{r}\frac{\partial u_\varphi}{\partial \theta} - \frac{u_\varphi}{r}\cot\theta + \frac{1}{r\sin\theta}\frac{\partial u_\theta}{\partial \varphi}\right),
\end{aligned}
\tag{3.4}
$$

where u_θ, u_φ and u_r are displacements in the directions of θ, φ and r, respectively.

3.1.2 Equilibrium equations

The sphere under consideration stays in equilibrium and the body force is neglected. Thus, the equations of equilibrium can be written as

$$
\begin{aligned}
\frac{\partial \sigma_{rr}}{\partial r} + \frac{1}{r\sin\theta}\frac{\partial \sigma_{r\varphi}}{\partial \varphi} + \frac{1}{r}\frac{\partial \sigma_{r\theta}}{\partial \theta} + \frac{2\sigma_{rr} - \sigma_{\theta\theta} - \sigma_{\varphi\varphi} + \sigma_{r\theta}\cot\theta}{r} &= 0 \\
\frac{\partial \sigma_{r\varphi}}{\partial r} + \frac{1}{r\sin\theta}\frac{\partial \sigma_{\varphi\varphi}}{\partial \varphi} + \frac{1}{r}\frac{\partial \sigma_{\theta\varphi}}{\partial \theta} + \frac{3\sigma_{r\varphi} + 2\sigma_{\theta\varphi}\cot\theta}{r} &= 0 \\
\frac{\partial \sigma_{r\theta}}{\partial r} + \frac{1}{r\sin\theta}\frac{\partial \sigma_{\theta\varphi}}{\partial \varphi} + \frac{1}{r}\frac{\partial \sigma_{\theta\theta}}{\partial \theta} + \frac{3\sigma_{r\theta} + (\sigma_{\theta\theta} - \sigma_{\varphi\varphi})\cot\theta}{r} &= 0 \,.
\end{aligned}
\tag{3.5}
$$

Substituting Eq. (3.1) and (3.4) into (3.5), the equilibrium equations read as

$$
\begin{aligned}
-2(A_{12} + A_{66})\frac{\varepsilon_1}{r} + A_{13}\left(\frac{\partial \varepsilon_1}{\partial r} + \frac{2\varepsilon_1}{r} - \frac{2\varepsilon_{rr}}{r}\right) + A_{33}\left(\frac{\partial \varepsilon_{rr}}{\partial r} + \frac{2\varepsilon_{rr}}{r}\right) + \\
A_{44}\left[\frac{1}{r^2}\nabla_1^2 u_r + \frac{\partial}{\partial r}\left(\varepsilon_1 - \frac{2u_r}{r}\right)\right] = 0
\end{aligned}
$$

$$
\begin{aligned}
\frac{A_{12}}{r\sin\theta}\frac{\partial \varepsilon_1}{\partial \varphi} + 2A_{66}\left(\frac{1}{r\sin\theta}\frac{\partial \varepsilon_{\varphi\varphi}}{\partial \varphi} + \frac{1}{r}\frac{\partial \varepsilon_{\theta\varphi}}{\partial \theta} + \frac{2\cot\theta}{r}\varepsilon_{\theta\varphi}\right) + \frac{A_{13}}{r\sin\theta}\frac{\partial \varepsilon_{rr}}{\partial \varphi} + \\
2A_{44}\left(\frac{\partial \varepsilon_{r\varphi}}{\partial r} + \frac{3\varepsilon_{r\varphi}}{r}\right) = 0
\end{aligned}
\tag{3.6}
$$

$$
\begin{aligned}
\frac{A_{12}}{r}\frac{\partial \varepsilon_1}{\partial \theta} + 2A_{66}\left[\frac{1}{r\sin\theta}\frac{\partial \varepsilon_{\theta\varphi}}{\partial \varphi} + \frac{1}{r}\frac{\varepsilon_{\theta\theta}}{\partial \theta} + \frac{\cot\theta}{r}(\varepsilon_{\theta\theta} - \varepsilon_{\varphi\varphi})\right] + \frac{A_{13}}{r}\frac{\partial \varepsilon_{rr}}{\partial \theta} + \\
2A_{44}\left(\frac{\partial \varepsilon_{r\theta}}{\partial r} + \frac{3\varepsilon_{r\theta}}{r}\right) = 0 \,,
\end{aligned}
$$

where

$$\varepsilon_1 = \varepsilon_{\theta\theta} + \varepsilon_{\varphi\varphi}$$

$$\nabla_1^2 = \frac{\partial^2}{\partial\theta^2} + \cot\theta\frac{\partial}{\partial\theta} + \frac{1}{\sin^2\theta}\frac{\partial^2}{\partial\varphi^2} \ . \tag{3.7}$$

3.1.3 Boundary conditions
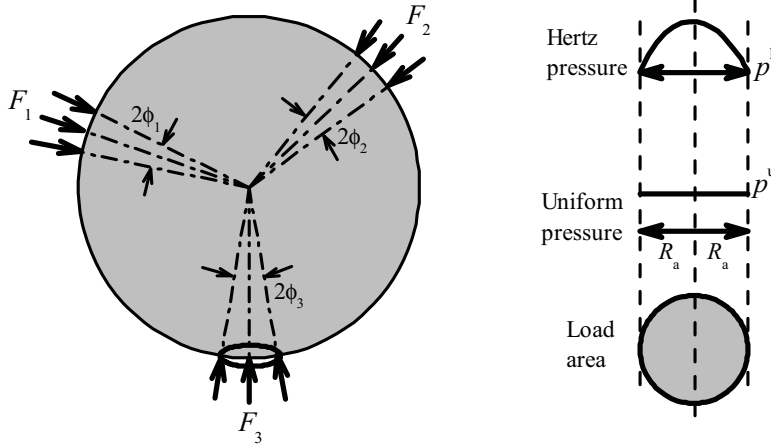
Figure 3.3: Left: three loads applied on the sphere surface; right: two pressure distributions.

For the sphere in equilibrium, the i-th load of magnitude of F_i is applied on the i-th circle load area A_i, which subtends an angle of $2\phi_i$ from the center of sphere as shown in Fig. 3.3. It is assumed that the load is axisymmetrically distributed in each load area. The symmetry axis, namely loading axis, is the line across the center of the load area (R, θ_i, φ_i) and the sphere center. The position of i-th load is denoted by (θ_i, φ_i) in the remainder of this chapter. The pressure p_i is distributed along the radial direction in the range of $0 \leqslant \phi \leqslant \phi_i$. Subsequently, the boundary conditions can be written as

$$\sigma_{rr}^i(\phi) = \begin{cases} p_i(\phi) & 0 \leqslant \phi \leqslant \phi_i \\ 0 & \text{in the other areas} \end{cases} \tag{3.8}$$

and

$$\sigma_{r\varphi} = \sigma_{r\theta} = 0 \tag{3.9}$$

on $r = R$, where R is the radius of sphere. p_i is a pressure distribution which can be any kind of distribution in this work. In practice, pressure distribution is induced by contact, e.g, contact between a plate and a sphere. The adopted pressure distribution in this work is meaningful only when it gives rise to the same stress state in the sphere as that induced in a real contact. In order to obtain an explicit pressure distribution, its distribution form and the relation between pressure

and load have to be assumed. For a given contact problem, the accuracy of the solution in this work depends on the consistency between the assumptions and the real contact case.

Two pressure distributions, i.e., uniform pressure p^u and Hertz pressure p^h, are considered

$$p_i^u(\phi) = -p_u \tag{3.10}$$

$$p_i^h(\phi) = -p_{\max}\left[1 - \left(\frac{\sin\phi}{\sin\phi_i}\right)^2\right]^{\frac{1}{2}}, \tag{3.11}$$

where p_u is the uniform pressure and $p_{\max}$ is the maximum pressure in the load area. Both of them are determined by the relation between pressure and load. The Hertz pressure distribution in Eq. (3.11) conforms to the Hertz pressure expression of Eq. (3.39) in Johnson (1987).

For the uniform pressure, the relation

$$\int_{A_i} p_i dA = \int_0^{\phi_i} p_i 2\pi R^2 \sin\phi d\phi = -F_i \tag{3.12}$$

has been used by Hiramatsu and Oka (1966) and Chau and Wei (1999) to derive the analytical solutions for stresses in a sphere subjected to a pair of uniaxial loads (for the case of $R_{a1} = R_{a2}$ in Fig. 3.4). A is the initial surface load area. The pressure is applied on the initial (undeformed) load area as shown in Fig. 3.4. The uniform pressure reads as

$$p_u = \frac{F_i}{2\pi R^2(1 - \cos\phi_i)} . \tag{3.13}$$

Substitution of Eq. (3.11) into (3.12) yields

$$p_{\max} = \frac{F_i}{\pi R^2}\frac{1}{1 - \text{arctanh}(\sin\phi_i)\cot\phi_i\cos\phi_i} . \tag{3.14}$$

Both pressure distributions will be used in our analysis. The uniform distribution, namely Eqs. (3.10) and (3.13), will be used to validate the solution obtained in this work by comparison with the result calculated by Chau and Wei (1999). The Hertz distribution, namely Eqs. (3.11) and (3.14), should be closer to the one in an elastic contact. Thus, Hertz pressure is better than uniform pressure to represent the case for elastic contact.

For the Hertz pressure distribution, another relation between pressure and load reads as

$$\int_{S_i} p_i dS = \int_0^{\phi_i} p_i 4\pi R^2 \sin\phi\cos\phi d\phi = -F_i , \tag{3.15}$$

where S is the area of the load circle with a radius R_a. The pressure is applied on the circle along the load axis direction. The derived $p_{\max}$ is exactly the one derived by Hertz (1881) as

$$p_{\max} = \frac{3}{2}\frac{F_i}{\pi R_a^2} = \frac{F_i}{2\pi R^2}\frac{3}{\sin^2\phi_i} . \tag{3.16}$$
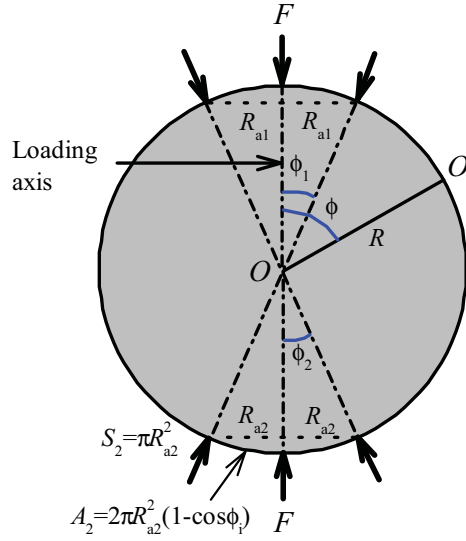
Figure 3.4: Uniaxial loading on a sphere. R_{a1} and R_{a2} are two load radii. O' is a point on the surface. ϕ ranging from 0 to $\pi/2$ is the angle between the loading axis and the line across O and O'.

The Hertz distribution together with Eq. (3.16) was used by Chau et al. (2000) for the case of a pair of rigid plates compressing an elastic sphere. However, the value $p_{\max}$ calculated from Eqs. (3.14) and (3.16), respectively, has a little difference. For example, the difference is less than 0.2% for the same F_i, R and $\phi_i = 5°$, which means the corresponding stress difference at any point in the sphere will be less than 0.2%. Accordingly, the $p_{\max}$ in Eq. (3.14) is used in this work.

Force equilibrium requires that

$$\sum_i F_i \cos \theta_i = 0$$

$$\sum_i F_i \sin \theta_i \cos \varphi_i = 0 \qquad (3.17)$$

$$\sum_i F_i \sin \theta_i \sin \varphi_i = 0 \ .$$

3.1.4 Displacement functions

It was proposed by Hu (1954) that the displacements under consideration can be expressed by two displacement potential functions. In order to get the explicit roots for the governing equations, Chau and Wei (1999) have made some changes of the variables. As a result, two displacement potentials Z and Φ are derived, which satisfy

$$A_{44}\left(\frac{\partial^2 Z}{\partial \eta^2} + \frac{\partial Z}{\partial \eta}\right) + A_{66}\nabla_1^2 Z - 2(A_{44} - A_{66})Z = 0 \qquad (3.18)$$

$$\left[\left(\frac{\partial^2}{\partial\eta^2}+\frac{\partial}{\partial\eta}\right)^2+2D\left(\frac{\partial^2}{\partial\eta^2}+\frac{\partial}{\partial\eta}\right)+M\nabla_1^2\left(\frac{\partial^2}{\partial\eta^2}+\frac{\partial}{\partial\eta}\right)-4L+2(N-L)\nabla_1^2+N\nabla_1^2\nabla_1^2\right]\Phi=0\,. \tag{3.19}$$

Appendix I shows details including the introduced variables, such as Z, F, H and η, and parameters, such as D, L, M and N. The displacements components read as

$$u_\theta = -\frac{1}{\sin\theta}\frac{\partial Z}{\partial\varphi}+\left[d\frac{\partial}{\partial\eta}+2(a+b)\right]\frac{\partial\Phi}{\partial\theta}$$

$$u_\varphi = \frac{\partial Z}{\partial\theta}+\frac{1}{\sin\theta}\left[d\frac{\partial}{\partial\eta}+2(a+b)\right]\frac{\partial\Phi}{\partial\phi} \tag{3.20}$$

$$u_r = -\left[h\left(\frac{\partial^2}{\partial\eta^2}+\frac{\partial}{\partial\eta}\right)+a\nabla_1^2-2b\right]\Phi\,.$$

The strain and stress components can be expressed in terms of Z and Φ by substitution of Eq. (3.20) into (3.4) and (3.1) subsequently. Now it is clear that when Z and Φ are known, the problem is solved.

Inspired by the displacement functions used by Chau and Wei (1999), the solution form

$$Z = \sum_{n=0}^{\infty}\sum_{m=0}^{n}e^{\lambda_n\eta}S_{nm}(\theta,\varphi) \tag{3.21}$$

is sought for the displacement function Z, where

$$S_{nm}(\theta,\varphi) = (D_{nm}^1\cos m\varphi + D_{nm}^2\sin m\varphi)P_n^m(\cos\theta)\,. \tag{3.22}$$

D_{nm}^1, D_{nm}^2 and λ_n are constants. $P_n^m(x)$ is the associated Legendre function. S_{nm} satisfies

$$\nabla_1^2 S_{nm}(\theta,\varphi)+n(n+1)S_{nm}(\theta,\varphi)=0\,. \tag{3.23}$$

Both n and m are integers. n ranges from 0 to infinity and m ranges from 0 to n.

Substitution of Eq. (3.21) into (3.18) yields

$$\lambda_n^2+\lambda_n-M_n=0\,, \tag{3.24}$$

where

$$M_n = 2+(n-1)(n+2)\frac{A_{66}}{A_{44}}\,. \tag{3.25}$$

The two characteristic roots for Eq. (3.24) are

$$\lambda_{n1}=\frac{-1+\sqrt{1+4M_n}}{2},\ \lambda_{n2}=\frac{-1-\sqrt{1+4M_n}}{2}\,. \tag{3.26}$$

As a result, if $\lambda_{n1}\neq\lambda_{n2}$, Z reads as

$$Z = \sum_{n=0}^{\infty}\sum_{m=0}^{n}(D_{n1}^m e^{\lambda_{n1}\eta}+D_{n3}^m e^{\lambda_{n2}\eta})\cos m\varphi P_n^m(\cos\theta)+$$

$$\sum_{n=0}^{\infty}\sum_{m=0}^{n}(D_{n2}^m e^{\lambda_{n1}\eta}+D_{n4}^m e^{\lambda_{n2}\eta})\sin m\varphi P_n^m(\cos\theta)\,, \tag{3.27}$$

where $D_{ni}^m(i = 1, 2, 3, 4)$ are unknown coefficients.

Similarly, the solution form

$$\Phi = \sum_{n=0}^{\infty} \sum_{m=0}^{n} e^{\mu_n \eta} S'_{nm}(\theta, \varphi) \tag{3.28}$$

is sought for the displacement function Φ, where

$$S'_{nm}(\theta, \varphi) = (C_{nm}^1 \cos m\varphi + C_{nm}^2 \sin m\varphi) P_n^m(\cos\theta) . \tag{3.29}$$

Substitution of Eq. (3.28) into Eq. (3.19) yields

$$(\mu_n^2 + \mu_n)^2 + 2P_n(\mu_n^2 + \mu_n) + Q_n = 0 , \tag{3.30}$$

where

$$P_n = D - n(n+1)\frac{M}{2}, \ Q_n = (n+2)(n-1)\Big[2L + n(n+1)N\Big] . \tag{3.31}$$

The four characteristic roots for Eq. (3.30) are

$$\mu_{n1} = \frac{-1 + \sqrt{\varsigma_n}}{2}, \ \mu_{n2} = \frac{-1 + \sqrt{\xi_n}}{2}, \ \mu_{n3} = \frac{-1 - \sqrt{\varsigma_n}}{2}, \ \mu_{n4} = \frac{-1 - \sqrt{\xi_n}}{2} , \tag{3.32}$$

where

$$\varsigma_n = 1 - 4\big(P_n + \sqrt{P_n^2 - Q_n}\big), \ \xi_n = 1 - 4\big(P_n - \sqrt{P_n^2 - Q_n}\big) . \tag{3.33}$$

If these roots are distinct, Φ reads as

$$\begin{aligned}
\Phi = \sum_{n=0}^{\infty} \sum_{m=0}^{n} (C_{n1}^m e^{\mu_{n1}\eta} + C_{n2}^m e^{\mu_{n2}\eta} + C_{n5}^m e^{\mu_{n3}\eta} + C_{n6}^m e^{\mu_{n4}\eta}) \cos m\varphi P_n^m(\cos\theta) + \\
\sum_{n=0}^{\infty} \sum_{m=0}^{n} (C_{n3}^m e^{\mu_{n1}\eta} + C_{n4}^m e^{\mu_{n2}\eta} + C_{n7}^m e^{\mu_{n3}\eta} + C_{n8}^m e^{\mu_{n4}\eta}) \sin m\varphi P_n^m(\cos\theta) ,
\end{aligned} \tag{3.34}$$

where $C_{ni}^m(i = 1, 2, 3, 4, 5, 6, 7, 8)$ are unknown coefficients.

The proposed Z and Φ depend on φ, which enables to resolve the solution for asymmetric boundary conditions. For example, when a sphere is subjected to three loads along different directions, the load boundary condition is asymmetric.

3.1.5 Characteristic roots

Chau and Wei (1999) concluded that all roots for λ_n and μ_n with a real part less than 1 would lead to infinite stresses at the sphere center and have to be discarded. Furthermore, the analysis also indicated that the real parts of λ_{n2}, μ_{n3} and μ_{n4} are less than 1. Consequently, D_{n3}^m, D_{n4}^m, and C_{ni}^m $(i = 5, 6, 7, 8)$ should be set to zero.

As a result, Eq. (3.27) reduces to

$$Z = \sum_{n=0}^{\infty} \sum_{m=0}^{n} \Big[D_{n1}^m e^{\lambda_{n1}\eta} \cos m\varphi P_n^m(\cos\theta) + D_{n2}^m e^{\lambda_{n1}\eta} \sin m\varphi P_n^m(\cos\theta) \Big] . \tag{3.35}$$

On the other hand, there are two cases for Φ.

Case I: Two real roots

If $P_n^2 - Q_n > 0$, $\xi_n > 0$ and $\varsigma_n > 0$, μ_{n1} and μ_{n2} are two real unequal roots. If $\mu_{n1} \geqslant 1$ and $\mu_{n2} \geqslant 1$, the resultant solution is

$$
\begin{aligned}
\Phi_n^m =& (C_{n1}^m e^{\mu_{n1}\eta} + C_{n2}^m e^{\mu_{n2}\eta}) \cos m\varphi P_n^m(\cos\theta) + \\
& (C_{n3}^m e^{\mu_{n1}\eta} + C_{n4}^m e^{\mu_{n2}\eta}) \sin m\varphi P_n^m(\cos\theta) \, .
\end{aligned}
\tag{3.36}
$$

If $\mu_{n1} < 1$ and $\mu_{n2} < 1$, there are no converging solutions.

Case II: Two complex conjugate roots

If $P_n^2 - Q_n < 0$, μ_{n1} and μ_{n2} are two complex conjugates. If the real part for both μ_{n1} and μ_{n2} is not less than 1, the resultant solution is

$$
\begin{aligned}
\Phi_n^m =& (E_{n1}^m e^{\mu_n \eta} + \bar{E}_{n1}^m e^{\bar{\mu}_n \eta}) \cos m\varphi P_n^m(\cos\theta) + \\
& (E_{n2}^m e^{\mu_n \eta} + \bar{E}_{n2}^m e^{\bar{\mu}_n \eta}) \sin m\varphi P_n^m(\cos\theta) \, ,
\end{aligned}
\tag{3.37}
$$

where $E_{n\alpha}^m = R_{n\alpha}^m + i I_{n\alpha}^m$ $(\alpha = 1, 2)$ are complex constants and $\mu_n = x_n + i y_n$ with

$$
x_n + i y_n = \frac{-1 + \sqrt{1 - 4P_n - i4\sqrt{|P_n^2 - Q_n|}}}{2} \, .
\tag{3.38}
$$

$\bar{E}_{n\alpha}^m$ and $\bar{\mu}_n$ are complex conjugates of $E_{n\alpha}^m$ and μ_n, respectively.

Subsequently, the general solution for Φ is

$$
\Phi = \sum_{n=0}^{\infty} \sum_{m=0}^{n} \Phi_n^m \, ,
\tag{3.39}
$$

where Φ_n^m is defined either in Eq. (3.36) or (3.37), which depends on the type of μ_n.

3.1.6 The general solution

Substituting Eqs. (3.35) and (3.39) into Eqs. (3.20), (3.4) and (3.1) subsequently, the stress components read as

$$\sigma_{\theta\theta} = -\frac{1}{R}\sum_{h=0}^{\infty}\sum_{i=1}^{2}\sum_{m=0}^{h}D_{hi}^{m}\rho^{\lambda_{hi}-1}\left\{2A_{66}\csc\theta(-1)^{i}m\left[\frac{\partial P_{h}^{m}(\cos\theta)}{\partial\theta}-\cot\theta P_{h}^{m}(\cos\theta)\right]s_{i}\right\}$$

$$-\frac{1}{R}\sum_{l}\sum_{j=1}^{4}\sum_{m=0}^{l}C_{lj}^{m}\rho^{\mu_{lj}-1}\left\{\begin{array}{c}\left[\begin{array}{c}A_{12}l(l+1)\Gamma_{lj}+\\(A_{13}\mu_{lj}+2A_{12}+2A_{66})\Lambda_{lj}\end{array}\right]P_{l}^{m}(\cos\theta)\\-2A_{66}\Gamma_{lj}\dfrac{\partial^{2}P_{l}^{m}(\cos\theta)}{\partial\theta^{2}}\end{array}\right\}cs_{j}$$

$$+\frac{1}{R}\sum_{n}\sum_{k=1}^{2}\sum_{m=0}^{n}\rho^{x_{n}-1}\left\{\begin{array}{c}\left[\begin{array}{c}\Omega_{1}(R_{nk}^{m},I_{nk}^{m})\cos(y_{n}\ln\rho)+\\\Omega_{1}(-I_{nk}^{m},R_{nk}^{m})\sin(y_{n}\ln\rho)\end{array}\right]P_{n}^{m}(\cos\theta)-\\\left[\begin{array}{c}\Omega_{2}(R_{nk}^{m},I_{nk}^{m})\cos(y_{n}\ln\rho)+\\\Omega_{2}(-I_{nk}^{m},R_{nk}^{m})\sin(y_{n}\ln\rho)\end{array}\right]\dfrac{\partial^{2}P_{n}^{m}(\cos\theta)}{\partial\theta^{2}}\end{array}\right\}sc_{k}$$

$$(3.40)$$

$$\sigma_{r\varphi} = \frac{1}{R}\sum_{h=0}^{\infty}\sum_{i=1}^{2}\sum_{m=0}^{h}D_{hi}^{m}\rho^{\lambda_{hi}-1}(\lambda_{hi}-1)\frac{\partial P_{h}^{m}(\cos\theta)}{\partial\theta}sc_{i}$$

$$-\frac{\csc\theta}{R}\sum_{l}\sum_{j=1}^{4}\sum_{m=0}^{l}\left\{A_{44}C_{lj}^{m}\rho^{\mu_{lj}-1}\left[(1-\mu_{lj})\Gamma_{lj}+\Lambda_{lj}\right]\right\}sgn_{j}P_{l}^{m}(\cos\theta)cs_{5-j}\qquad(3.41)$$

$$+\frac{\csc\theta}{R}\sum_{n}\sum_{k=1}^{2}\sum_{m=0}^{n}\rho^{x_{n}-1}\left[\begin{array}{c}\Pi(R_{nk}^{m},I_{nk}^{m})\cos(y_{n}\ln\rho)+\\\Pi(-I_{nk}^{m},R_{nk}^{m})\sin(y_{n}\ln\rho)\end{array}\right](-1)^{k}mP_{n}^{m}(\cos\theta)s_{k}$$

$$\sigma_{r\theta} = -\frac{\csc\theta}{R}\sum_{h=0}^{\infty}\sum_{i=1}^{2}\sum_{m=0}^{h}D_{hi}^{m}\rho^{\lambda_{hi}-1}(\lambda_{hi}-1)(-1)^{i}mP_{h}^{m}(\cos\theta)s_{i}$$

$$-\frac{1}{R}\sum_{l}\sum_{j=1}^{4}\sum_{m=0}^{l}\left\{A_{44}C_{lj}^{m}\rho^{\mu_{lj}-1}\left[(1-\mu_{lj})\Gamma_{lj}+\Lambda_{lj}\right]\right\}\frac{\partial P_{l}^{m}(\cos\theta)}{\partial\theta}cs_{j}\qquad(3.42)$$

$$+\frac{1}{R}\sum_{n}\sum_{k=1}^{2}\sum_{m=0}^{n}\rho^{x_{n}-1}\left[\begin{array}{c}\Pi(R_{nk}^{m},I_{nk}^{m})\cos(y_{n}\ln\rho)+\\\Pi(-I_{nk}^{m},R_{nk}^{m})\sin(y_{n}\ln\rho)\end{array}\right]\frac{\partial P_{n}^{m}(\cos\theta)}{\partial\theta}sc_{k}$$

$$\sigma_{\theta\varphi} = \frac{A_{66}}{R}\sum_{h=0}^{\infty}\sum_{i=1}^{2}\sum_{m=0}^{h}D_{hi}^{m}\rho^{\lambda_{hi}-1}\left[\frac{\partial^{2}P_{h}^{m}(\cos\theta)}{\partial\theta^{2}}-\cot\theta\frac{\partial P_{h}^{m}(\cos\theta)}{\partial\theta}+\frac{m^{2}}{\sin^{2}\theta}P_{h}^{m}(\cos\theta)\right]sc_{i}$$

$$+\frac{2A_{66}}{R\sin\theta}\sum_{l}\sum_{j=1}^{4}\sum_{m=0}^{l}C_{lj}^{m}\rho^{\mu_{lj}-1}\Gamma_{lj}sgn_{j}m\left[\frac{\partial P_{l}^{m}(\cos\theta)}{\partial\theta}-\cot\theta P_{l}^{m}(\cos\theta)\right]cs_{5-j}$$

$$+\frac{2A_{66}}{R\sin\theta}\sum_{n}\sum_{k=1}^{2}\sum_{m=0}^{n}\Xi^{n}(R_{nk},I_{nk})(-1)^{k}m\left[\frac{\partial P_{n}^{m}(\cos\theta)}{\partial\theta}-\cot\theta P_{n}^{m}(\cos\theta)\right]s_{k},$$

$$(3.43)$$

where $\rho = r/R$ is the normalized radial length. The notations and functions

$$s_{2} = cs_{1} = cs_{2} = sc_{1} = \cos m\varphi \qquad(3.44a)$$

28

$$s_1 = cs_3 = cs_4 = sc_2 = \sin m\varphi \tag{3.44b}$$

$$sgn_1 = sgn_2 = -sgn_3 = -sgn_4 = -1 \tag{3.44c}$$

$$\mu_{l3} = \mu_{l1}, \ \mu_{l4} = \mu_{l2} \tag{3.44d}$$

$$\Gamma_{lj} = d\mu_{lj} + 2(a + b) \tag{3.44e}$$

$$\Lambda_{lj} = h\mu_{lj}(\mu_{lj} + 1) - 2b - al(l + 1) \tag{3.44f}$$

$$
\begin{aligned}
\Omega_1(R, I) =& 4A_{44}(A_{12} + A_{66}) \left[I(2x_n + 1)y_n - R(x_n^2 - y_n^2 + x_n) \right] + \\
& A_{12}n(n + 1) \left[2d(Iy_n - Rx_n) - 4(a + b)R \right] + \\
& 2A_{44}A_{13} \left[(Ix_n + Ry_n)(2x_n + 1)y_n - (Rx_n - Iy_n)(x_n^2 - y_n^2 + x_n) \right] + \\
& 2 \left[2b + an(n + 1) \right] \left[2(A_{12} + A_{66})R + A_{13}(Rx_n - Iy_n) \right]
\end{aligned}
\tag{3.44g}
$$

$$\Omega_2(R, I) = 2A_{66} \left[2d(Iy_n - Rx_n) - 4(a + b)R \right] \tag{3.44h}$$

$$
\begin{aligned}
\Pi(R, I) =& A_{44} \left\{ \begin{matrix} Iy_n[2d(1 - 2x_n) - 4(a + b)] + \\ R[2d(x_n^2 - y_n^2 - x_n) + 4(a + b)(x_n - 1)] \end{matrix} \right\} - \\
& 2A_{44}^2 \left[R(x_n^2 - y_n^2 + x_n) - I(2x_n + 1)y_n \right] + 2A_{44} \left[2b + an(n + 1) \right] R
\end{aligned}
\tag{3.44i}
$$

$$
\Xi^n(R, I) = 2\rho^{x_n - 1} \left\{ \begin{matrix} \left[R\cos(y_n \ln \rho) - I\sin(y_n \ln \rho) \right] \left[dx_n + 2(a + b) \right] \\ - \left[I\cos(y_n \ln \rho) + R\sin(y_n \ln \rho) \right] dy_n \end{matrix} \right\}
\tag{3.44j}
$$

have been used.

The unknown coefficients in the above equations can be obtained by applying the boundary conditions, i.e., Eqs. (3.8) and (3.9). All stress components will be derived when these coefficients are known. Note that the first summation for l is done for the case of two real roots and the second summation for n is done for the case of two complex roots. The relation

$$
\frac{-m^2}{\sin^2 \theta} P_n^m(\cos \theta) + \frac{\partial^2 P_n^m(\cos \theta)}{\partial \theta^2} + \cot \theta \frac{\partial P_n^m(\cos \theta)}{\partial \theta} = -n(n + 1)P_n^m(\cos \theta)
\tag{3.45}
$$

has been used in the deduction, which is a variation of Eq. (3.23).

Note that there is a special case for $n = 0$. It holds $\mu_{n1} = (-1 + |2n - 1|)/2$ and $\mu_{n2} = n + 1$ for an isotropic material. Although $\mu_{n1} = 0 < 1$ when $n = 0$, it does *NOT* lead to infinite stresses at the sphere center because $\rho^{\mu_{n1} - 1}$ in Eq. (3.40) multiplies a zero value. Therefore, the first term for $n = 0$ in the series should be checked separately. Moreover, $n = 0$ is the only exception of the requirement for roots for isotropic materials. For $\sigma_{\theta\theta}, \sigma_{\varphi\varphi}$ and σ_{rr} in our solution, the term for $n = 0$ is A_0^0 (see Eq. (3.47) below). On the other hand, this term for $\sigma_{r\varphi}, \sigma_{r\theta}$ and $\sigma_{\theta\varphi}$ is alway 0. This term for all stress components is independent of positions in the sphere.

The expression for σ_{rr} can be obtained by replacing A_{12}, $(2A_{66})$ and A_{13}, with A_{13}, 0 and A_{33} in Eq. (3.40), respectively. Replacing A_{12} and $(2A_{66})$ in Eq. (3.40) by $(2A_{66} + A_{12})$ and $(-2A_{66})$, respectively, yields the expression for $\sigma_{\varphi\varphi}$.

3.1.7 Determination of unknown coefficients

The union of all loads $p(\theta, \varphi) = \cup p_i(\phi)$ on a sphere surface can be expanded with the associated Legendre function (see Appendix II).

$$p(\theta, \varphi) = \sum_{n=0}^{\infty} \sum_{m=0}^{m=n} \left(A_n^m \cos m\varphi + B_n^m \sin m\varphi\right) P_n^m(\cos \theta) , \qquad (3.46)$$

where A_n^m and B_n^m are two coefficients determined by

$$\begin{aligned} A_n^m &= \frac{(2n+1)(n-m)!}{2\pi\delta_m(n+m)!} \int_0^\pi \int_0^{2\pi} p(\theta, \varphi) P_n^m(\cos \theta) \cos m\varphi \sin \theta d\varphi d\theta \\ B_n^m &= \frac{(2n+1)(n-m)!}{2\pi(n+m)!} \int_0^\pi \int_0^{2\pi} p(\theta, \varphi) P_n^m(\cos \theta) \sin m\varphi \sin \theta d\varphi d\theta , \end{aligned} \qquad (3.47)$$

where

$$\delta_m = \begin{cases} 2 & m = 0 \\ 1 & m \neq 0 . \end{cases} \qquad (3.48)$$

Consequently, the boundary condition of Eq. (3.8) becomes

$$\sigma_{rr}|_{r=R} = p(\theta, \varphi) = \sum_{n=0}^{\infty} \sum_{m=0}^{m=n} \left(A_n^m \cos m\varphi + B_n^m \sin m\varphi\right) P_n^m(\cos \theta) . \qquad (3.49)$$

The domain of the integrals in Eq. (3.47) is shown in Appendix III. Moreover, in Appendix IV the angle ϕ as a function of (θ, φ) is derived. In Appendix V the relation between coefficients using the boundary condition of Eq. (3.9) is obtained. These relations yield the explicit forms of all coefficients in the stress expressions as

$$\begin{aligned} D_{h1}^m &= 0, & D_{h2}^m &= 0 \\ C_{l2}^m &= -\frac{A_l^m R}{L_{12}J_{l1} + J_{l2}}, & C_{l4}^m &= -\frac{B_l^m R}{L_{12}J_{l1} + J_{l2}} \\ R_{n1}^m &= \frac{A_n^m R}{H_n}, & R_{n2}^m &= \frac{B_n^m R}{H_n} \end{aligned} \qquad (3.50)$$

and

$$C_{l1}^m = L_{l12}C_{l2}^m, \ C_{l3}^m = L_{l12}C_{l4}^m, \ I_{n1}^m = K_{n12}R_{n1}^m, \ I_{n2}^m = K_{n12}R_{n2}^m , \qquad (3.51)$$

where

$$J_{lj} = A_{13}l(l+1)\Gamma_{lj} + (A_{33}\mu_{lj} + 2A_{13})\Lambda_{lj} \qquad (3.52\text{a})$$

$$L_{l12} = -\frac{(1 - \mu_{l2})\Gamma_{l2} + \Lambda_{l2}}{(1 - \mu_{l1})\Gamma_{l1} + \Lambda_{l1}}, \ K_{n12} = \frac{\Pi(1,0)}{\Pi(0,-1)} \qquad (3.52\text{b})$$

$$\begin{aligned} H_n =\ & 4A_{44}A_{13} \left[K_{n12}(2x_n + 1)y_n - (x_n^2 - y_n^2 + x_n)\right] + \\ & A_{13}n(n+1) \left[2d(K_{n12}y_n - x_n) - 4(a+b)\right] + \\ & 2A_{44}A_{33} \begin{bmatrix} (K_{n12}x_n + y_n)(2x_n + 1)y_n - \\ (x_n - K_{n12}y_n)(x_n^2 - y_n^2 + x_n) \end{bmatrix} + \\ & 2\left[2b + an(n+1)\right]\left[2A_{13} + A_{33}(x_n - K_{n12}y_n)\right] . \end{aligned} \qquad (3.52\text{c})$$

3.1.8 Final solution

Substitution of Eqs.(3.50) and (3.51) into Eqs. (3.40), (3.41) and (3.42) gives the final expressions for stress components as

$$
\sigma_{\theta\theta} = \sum_l \sum_{m=0}^l \left[\frac{A_l^m}{L_{l12}J_{l1} + J_{l2}} \cos m\varphi + \frac{B_l^m}{L_{l12}J_{l1} + J_{l2}} \sin m\varphi \right] \Theta_l +
$$
$$
\sum_n \sum_{m=0}^n \left[\frac{A_n^m}{H_n} \cos m\varphi + \frac{B_n^m}{H_n} \sin m\varphi \right] \Theta_n \tag{3.53}
$$

$$
\sigma_{r\varphi} = \sum_l \sum_{m=0}^l \Xi_l \left[-\frac{A_l^m}{L_{l12}J_{l1} + J_{l2}} \sin m\varphi + \frac{B_l^m}{L_{l12}J_{l1} + J_{l2}} \cos m\varphi \right] m \csc\theta P_l^m(\cos\theta)
$$
$$
+ \sum_n \sum_{m=0}^n \Xi_n \left[-\frac{A_n^m}{H_n} \sin m\varphi + \frac{B_n^m}{H_n} \cos m\varphi \right] m \csc\theta P_n^m(\cos\theta) \tag{3.54}
$$

$$
\sigma_{r\theta} = \sum_l \sum_{m=0}^l \Xi_l \left[\frac{A_l^m}{L_{l12}J_{l1} + J_{l2}} \cos m\varphi + \frac{B_l^m}{L_{l12}J_{l1} + J_{l2}} \sin m\varphi \right] \frac{\partial P_l^m(\cos\theta)}{\partial\theta}
$$
$$
+ \sum_n \sum_{m=0}^n \Xi_n \left[\frac{A_n^m}{H_n} \cos m\varphi + \frac{B_n^m}{H_n} \sin m\varphi \right] \frac{\partial P_n^m(\cos\theta)}{\partial\theta} \tag{3.55}
$$

$$
\sigma_{\theta\varphi} = \left\{ \begin{array}{l} \displaystyle\sum_l \sum_{m=0}^l \Xi^l \left[\frac{A_l^m}{L_{l12}J_{l1} + J_{l2}} \sin m\varphi - \frac{B_l^m}{L_{l12}J_{l1} + J_{l2}} \cos m\varphi \right] \\ \displaystyle\sum_n \sum_{m=0}^n \Xi^n(1, K_{n12}) \left[-\frac{A_n^m}{H_n} \sin m\varphi + \frac{B_n^m}{H_n} \cos m\varphi \right] \end{array} \right\}
$$
$$
\times \frac{2m A_{66}}{\sin\theta} \left[\frac{\partial P_i^m(\cos\theta)}{\partial\theta} - \cot\theta P_i^m(\cos\theta) \right] (i = l \text{ or } n) , \tag{3.56}
$$

where

$$
\Theta_l = \sum_{j=1}^2 \delta_{lj} \rho^{\mu_{lj}-1} \left\{ \begin{array}{l} [A_{12}l(l+1)\Gamma_{lj} + (A_{13}\mu_{lj} + 2A_{12} + 2A_{66})\Lambda_{lj}] \\ \times P_l^m(\cos\theta) - 2A_{66}\Gamma_{lj} \frac{\partial^2 P_l^m(\cos\theta)}{\partial\theta^2} \end{array} \right\} \tag{3.57a}
$$

$$
\Theta_n = \rho^{x_n-1} \left\{ \begin{array}{l} \left[\begin{array}{l} \Omega_1(1, K_{n12}) \cos(y_n \ln\rho) + \\ \Omega_1(-K_{n12}, 1) \sin(y_n \ln\rho) \end{array} \right] P_n^m(\cos\theta) - \\ \left[\begin{array}{l} \Omega_2(1, K_{n12}) \cos(y_n \ln\rho) + \\ \Omega_2(-K_{n12}, 1) \sin(y_n \ln\rho) \end{array} \right] \frac{\partial^2 P_l^m(\cos\theta)}{\partial\theta^2} \end{array} \right\} \tag{3.57b}
$$

$$
\Xi_l = \sum_{j=1}^2 \delta_{lj} A_{44} \rho^{\mu_{lj}-1} [(1 - \mu_{lj})\Gamma_{lj} + \Lambda_{lj}] \tag{3.57c}
$$

$$
\Xi_n = \rho^{x_n-1} [\Pi(1, K_{n12}) \cos(y_n \ln\rho) + \Pi(-K_{n12}, 1) \sin(y_n \ln\rho)] \tag{3.57d}
$$

$$
\Xi^l = L_{l12}\rho^{\mu_{l1}-1}\Gamma_{l1} + \rho^{\mu_{l2}-1}\Gamma_{l2} \tag{3.57e}
$$

31

$$\delta_{lj} = \begin{cases} L_{l12} & j = 1 \\ 1 & j = 2 \,. \end{cases} \tag{3.57f}$$

The expression for σ_{rr} can be obtained by replacing A_{12}, $(2A_{66})$ and A_{13}, with A_{13}, 0 and A_{33} in Eq. (3.53). Replacing A_{12} and $(2A_{66})$ in Eq. (3.53) by $(2A_{66} + A_{12})$ and $(-2A_{66})$, respectively, yields the expression for $\sigma_{\varphi\varphi}$.

3.2 Numerical evaluation and discussion
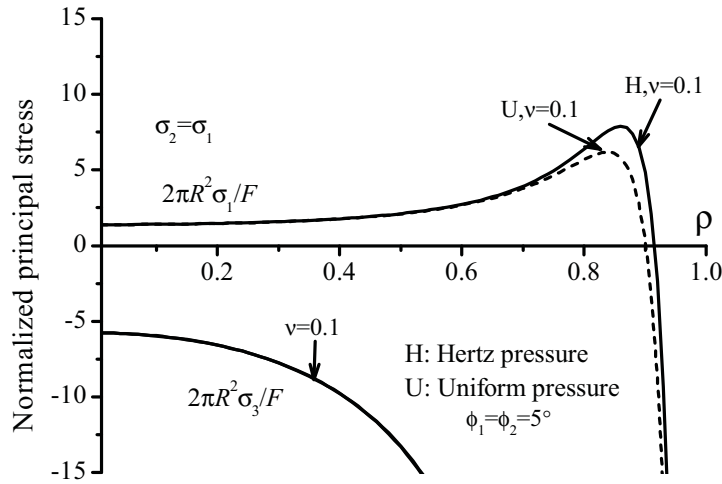
Figure 3.5: Normalized stresses along the loading axis ($\theta = 0°$) calculated from the solution derived by Chau and Wei (1999). The proposed Hertz pressure distribution, namely Eq. (3.11), is incorporated into the solution.

For the sake of simplicity, the analysis is restricted to isotropic ceramic pebbles, and the numerical evaluation only for isotropic materials will be reported. As stated in Section 3.1.6, it holds that $\mu_{n1} = (-1+|2n-1|)/2$ and $\mu_{n2} = n + 1$ for an isotropic material. The roots are two unequal real numbers which are not less than 1 for $n \geqslant 2$. Thus, there are only $l = 0, 2, 3, \cdots, \infty$ terms for the case of two real roots in the analytical solution obtained in this work, namely Eqs. (3.53), (3.54), (3.55) and (3.56). The term for $l = 1$ is discarded because of the root requirement (see Section 3.1.5). The analytical solution is evaluated numerically by summing a finite number of terms. Nt is defined as the number of summing terms which are not equal to zero. Hiramatsu and Oka (1966) derived the analytical solution for an isotropic sphere subjected to a pair of uniaxial loads (for the case of $R_{a1} = R_{a2}$ in Fig. 3.4). As for that solution, Wijk (1978) indicated that no good convergence can be achieved if the number of summing terms Nt is less than 20. The convergence rate will be discussed in the next section. Chau and Wei (1999) derived the corresponding solution for a spherically isotropic sphere. Uniform pressure was used in both analyses. However, the well-known Hertz pressure distribution should be applied if the loads are

induced by elastic contact. In the crush tests with elastic plates, the radius of the load area R_a can be measured or calculated for different plates. The input parameter ϕ_i in Eq. (3.11) corresponds to this radius. The relation between these quantities is $R_a = R \sin \phi_i$. Hence, our solution for Hertz pressure should represent the experimental situation when the two radii of load areas are the same.

Let the principal stresses be denoted by $\sigma_1 \geqslant \sigma_2 \geqslant \sigma_3$, respectively. Applying Eq. (3.11) to the solution derived by Chau and Wei (1999) the influence of pressure distributions is shown in Fig. 3.5. The principal stresses along the loading axis are plotted for both pressure distributions. The result for $\phi_i = 5^\circ$ and $\nu = 0.1$ has been demonstrated by Chau and Wei (1999) for the uniform pressure distribution. A relatively small Poisson's ratio $\nu = 0.1$ is used in Fig. 3.5 , so that the influence of pressure distributions can be distinctly illustrated. Note that tensile stresses are positive and compressive stresses are negative. Besides, it holds $\sigma_2 = \sigma_1$ along the loading axis for both pressure distributions. The maximum principal stress at $\rho \approx 0.85$ for Hertz pressure becomes higher than for uniform pressure. The minimum principal stress is hardly influenced by the pressure distributions. The curves in Fig. 3.5 can be used to validate the solution derived in this work.

Figure 3.6 shows the numerical evaluation for our solution for the same case as studied by Hiramatsu and Oka (1966) and Chau and Wei (1999). The loads lie in $(60^\circ, 36^\circ)$ and $(120^\circ, 216^\circ)$ (coordinate explained in Section 3.1.3), respectively. Both load areas correspond to $\phi_i = 5^\circ$. Note that in our solution loads cannot lie near $\theta = 0$ and $\theta = \pi$ (see Appendix III). The numerical evaluations have been truncated at $Nt = 25$. Attention should be given that the terms with odd number of n are zero because of load symmetry. The stresses along the loading axis for $\nu = 0.1$ coincide with those in Fig. 3.5. The stresses for $\nu = 0.25$ which is the Poisson's ratio of Li$_4$SiO$_4$ pebbles are plotted as well. The difference between the two pressure distributions becomes smaller when ν increases.

To further validate our analytical solution, FEM simulations have been performed. Table 3.1 lists the maximum tensile stress and maximum shear stress along the loading axis derived from our solution, FEM simulations and the Hüber-Hertz solution (Hüber, 1904), respectively. Hüber (1904) derived stresses within the Hertian elastic contact field in cylindrical coordinate system based on Hertz theory (Hertz, 1881). In our solution, the configuration is the same as that for Hertz pressure distribution and $\nu = 0.25$ in Fig. 3.6. The stresses are evaluated with more terms $Nt = 300$ in order to achieve a high accuracy. The sphere radius is set to $R = 0.25$ mm corresponding to the mean size of pebbles. $\phi_i = 5^\circ$ corresponds to a load $F = 2.497$ N for an elastic contact between BK7 plate and Li$_4$SiO$_4$ pebble according to the Hertz theory. For the convenience of comparison, $F = 2.497$ N is used to calculate the stresses in each method. In the FEM simulation, an elastic sphere with a radius of $R = 0.25$ mm is compressed between a pair of parallel flat plates. The material parameters for Li$_4$SiO$_4$ pebbles and BK7 plates in Table
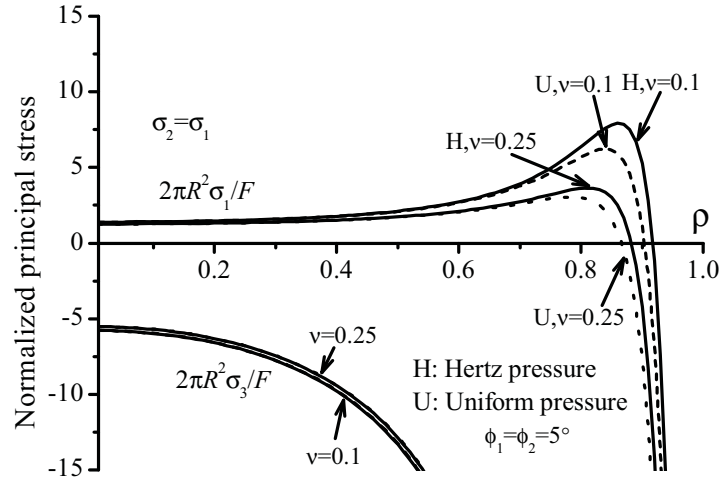
Figure 3.6: Normalized stresses along the loading axis ($\theta = 60^\circ, \varphi = 36^\circ$) calculated from our solution for $N_c = 2$.

2.1 are used. Interface friction is not taken into account. A pair of $F = 2.497$ N is applied on the plates uniaxially. The results are derived with a mesh size of 0.125 μm along the loading axis. A single contact between a sphere and a plate is considered in the Hüber-Hertz solution. Material parameters and the contact load are the same as those used in the FEM simulation. The configurations for each method correspond to the same load case. Therefore, the results are comparable, in principle.

Table 3.1: Maximum tensile tress σ_{max} and shear stress τ_{max} along the loading axis.

	Position: σ_{max} (MPa)	Position: τ_{max} (MPa)
Our solution	ρ =0.811: 23.2	ρ =0.955: 797
FEM simulation	ρ =0.812: 23.8	ρ =0.956: 801
Hüber-Hertz solution	ρ =0.825: 22.9	ρ =0.957: 808

The maximum tensile stress from Hüber-Hertz solution lies a little closer to the load area than the other methods. All the stresses are close to each other anyhow. The relative error between them is less than 3%. On the other hand, the maximum shear stresses appear almost at the same position close to the load area with a relative error of less than 1.5%. This good agreement validates our analytical solution and shows its applicability even near the load area. Note that the stresses in the sphere depend on the pair of loads in FEM simulations and our solution. They only depend on a single contact load for the Hüber-Hertz solution. Accordingly, there could be a difference to some extent. For example, $\sigma_{max} \approx 1.6$ MPa at the sphere center according to the Hüber-Hertz solution while $\sigma_{max} \approx 7.9$ MPa according to the FEM simulation and our solution. This difference indicates the invalidity of applying Hüber-Hertz solution at points away from the

load area.
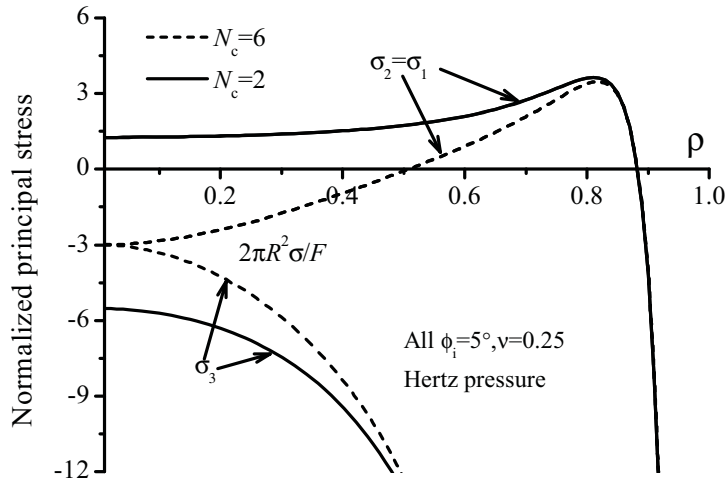
Figure 3.7: Normalized stresses along the loading axis ($\theta = 60^\circ, \varphi = 36^\circ$) calculated from our solution for $N_c = 6$ for Hertz pressure.

Our solution enables the stress analysis for a sphere subjected to various loads, i.e. $N_c > 2$. Figure 3.7 shows the principal stresses along one loading axis for $\nu = 0.25$ subjected to 6 Hertz pressures, i.e., $N_c = 6$. The stresses are evaluated with $Nt = 25$. The loads lie in $(60^\circ, 36^\circ)$, $(120^\circ, 216^\circ)$, $(90^\circ, 126^\circ)$, $(90^\circ, 306^\circ)$, $(150^\circ, 36^\circ)$, $(30^\circ, 216^\circ)$, respectively. Besides, the result for $\nu = 0.25$ and Hertz pressure in Fig. 3.6 is also plotted for comparison. The same load F is applied on each load area with the same size in both cases. In any case, the loads have to satisfy Eq. (3.17). Compared to the case for $N_c = 2$ the maximum principal stress for $N_c = 6$ changes greatly when ρ approaches zero. Tensile stresses become compressive at the sphere center. Note that the relation $\sigma_2 = \sigma_1$ holds for both $N_c = 2$ and $N_c = 6$ under consideration. On the other hand, the stresses stay approximately the same for both cases for $\rho > 0.8$.

The stresses along one loading axis for $N_c = 4$ are shown in Fig. 3.8. The stresses are also evaluated with $Nt = 25$. The loads lie in $(60^\circ, 36^\circ)$, $(120^\circ, 216^\circ)$, $(90^\circ, 126^\circ)$, $(90^\circ, 306^\circ)$, respectively. In this case, the maximum principal stress has increased significantly for a radius $\rho < 0.85$. Its peak value increases nearly by 25%. It is thus essential to consider the influence of N_c if the tensile stress inside a sphere is of big concern. Similar to Fig. 3.7, the stresses close to the load area, such as $\rho > 0.9$, are not influenced by N_c. The stresses at points that are close to the load area are still dominated by Hertz theory.

As mentioned in Section 3.1.3, the accuracy of our solution depends on the consistency between the assumed pressure distribution and the real contact one. The adopted Hertz pressure distribution, namely Eq. (3.11), and the pressure-load relation, namely Eq. (3.12), can represent the elastic contact case well according to the results in Table 3.1. Nevertheless, other pressure distributions correspond other contact cases. For example, if a elastic sphere is compressed by soft metals, plasticity may occur in the metal. For such a case, if the contact pressure distribution
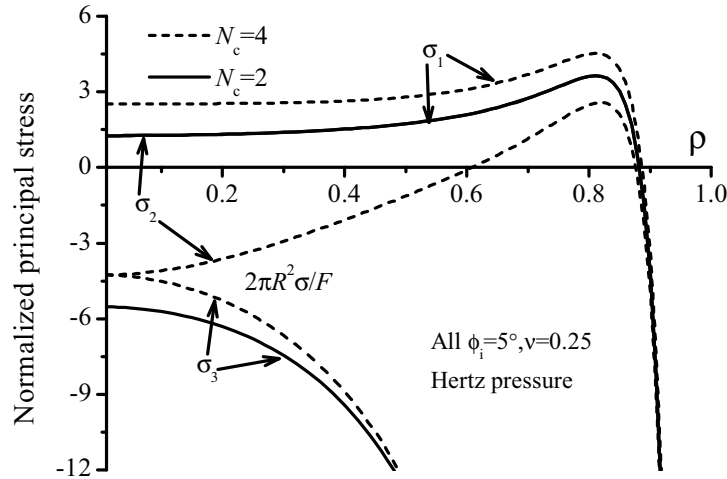
Figure 3.8: Normalized stresses along the loading axis ($\theta = 60°, \varphi = 36°$) calculated from our solution for $N_c = 4$ for Hertz pressure.

can be derived, such as from FEM simulation, it is expected that the results from our solution with the derived pressure distribution are close to the real case.

There are various combinations of equilibrium loads that can be applied on a sphere. The stresses in the sphere can be evaluated for any load combination. The load area or size can be different even for the same load. For instance, $R_{a1} \neq R_{a2}$ in Fig. 3.4 can represent the load case that a sphere is compressed by two parallel plates with different stiffnesses. Gundepudi et al. (1997) used a superposition method to obtain the stresses for different load combination as well. In their analysis there is an analytical stress solution in the sphere for a single load. The overall stresses at a point are the stress superposition of all loads. However, this solution is incorrect because the shear stress components, $\sigma_{r\varphi}$ and $\sigma_{\theta\varphi}$, are always zero in the analytical solution they used, which is not true for asymmetric loads. Furthermore, the maximum principal stress σ_1 at the sphere center, where stresses are almost independent of the Poission ratio (Chau and Wei, 1999), is too small for a pair of uniaxial loads (see Gundepudi et al., 1997, Fig. 4) compared to our evaluation in Fig. 3.6 which is validated by FEM simulation.

The solution from Hiramatsu and Oka (1966) can be regarded as a special case of the one from Chau and Wei (1999). Our solution obtained in this work is an extension of the one from Chau and Wei (1999). Note that Wijk (1978) speculated on the invalidity of applying the solution from Hiramatsu and Oka (1966) in the vicinity of the load areas. The applicability of such solutions is therefore discussed in the next section.

3.3 Applicability

This section discusses the applicability of the solution obtained in this work. However, the conclusions will also hold for the solutions of Hiramatsu and Oka (1966) and Chau and Wei (1999). The discussion includes two aspects. The first one is the convergence rate of the solution. For convenience the stress σ, which can denote any stress component of Eqs. (3.53), (3.54), (3.55) and (3.56), can be written for isotropic materials

$$\sigma_l = \sum_{m=0}^{l} \sigma_{lm}, \quad \sigma = \sigma_0 + \sum_{l=2}^{\infty} \sigma_l, \tag{3.58}$$

where σ_l is the l-th term in the series. The numerical evaluation is carried out by summing a finite number of terms. The number Nt is of concern as to the accuracy of results. Fast convergence rate needs less terms to achieve a certain accuracy. Figure 3.9 shows terms of the normalized stress $\sigma_{\theta\theta}$ with respect to even n. This corresponds to an elastic sphere subjected to a pair of
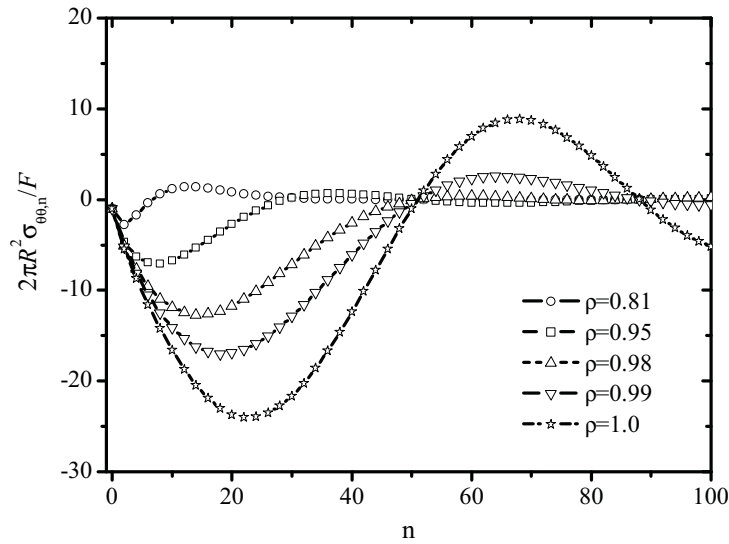
Figure 3.9: Normalized stress terms $\sigma_{\theta\theta,n}$ for $\sigma_{\theta\theta}$ along the loading axis calculated from our solution for $N_c = 2$ for Hertz pressure. $\nu = 0.25$ and $\phi_1 = \phi_2 = 5°$.

uniaxial loads with Hertz pressures where $\nu = 0.25$ and $\phi_1 = \phi_2 = 5°$. The terms for odd n is equal to zero because of load symmetry. The 0 terms for odd n are not counted into Nt in this work. The maximum tensile stress appearing around $\rho = 0.81$ requires about $Nt = 20$ to achieve a relative error of less than 0.1%. However, more terms are needed with ρ approaching 1. In other words, the convergence rate at points near the surface becomes slow. For example, to achieve the same relative error of 0.1%, the numerical evaluations show that $Nt \approx 140$ at $\rho = 0.95$ while $Nt \approx 320$ at $\rho = 0.99$.

The second point is the applicability on the sphere surface. Figure 3.9 illustrates that the slowest convergence rate is found on the surface ($\rho = 1$). If good convergence, such as a relative error

less than 1%, can be achieved only when Nt is very large, this might lead to numerical problems. Figure 3.10 shows the stresses on the surface derived from three methods with configurations as
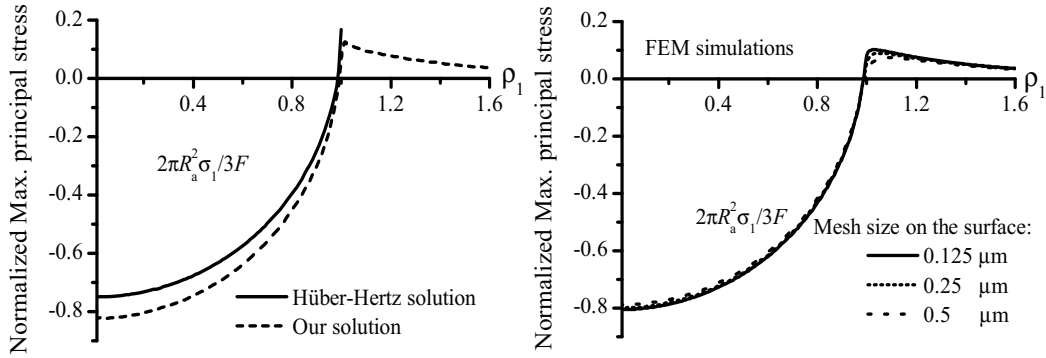
Figure 3.10: Normalized stresses on the surface, $\rho_1 = R\sin\phi/R_a$ for the Hüber-Hertz solution. $\rho_1 = R\phi/R_a$ for FEM simulations and our solution. ϕ is shown in Fig. 3.4. Configurations are the same as those stated in the last section.

used in the last section. The stresses are plotted with respect to the normalized distance away from the center of the contact area. The Hüber-Hertz result is obtained by applying $z = 0$ in the solution of Hüber (1904). The normalized maximum tensile stress appearing around $\rho_1 = 1$ is 0.167. The maximum tensile stress with $Nt = 2000$ terms for our solution is 0.125. The relative change, compared to $Nt = 8000$, is less than 2%. This value is still much smaller than 0.167. In the FEM simulations, three mesh sizes, namely $0.125, 0.25$ and 0.5 μm, on the surface are used, respectively. The derived maximum tensile stress becomes higher with smaller mesh size. Its position approaches to $\rho_1 = 1$ with decreasing mesh size. The maximum tensile stress for the mesh size of 0.125 μm is only about 0.1. Except in the area around $\rho_1 = 1$, the stresses from FEM simulations and our solution are a little higher than the Hüber-Hertz result. Even so, both stresses agree well with each other in most of the surface. This proves the applicability of our solution even on the surface. It should be noted that in Fig. 3.10 the stresses from the Hüber-Hertz solution is derived in a cylindrical coordinated system where the sphere is deformed, and the stresses from our solution and FEM simulation are given in a spherical coordinate system where the sphere is *undeformed*.

As for the maximum principal or tensile stresses on the surface, there are three different values derived from our solution, FEM simulations and the Hüber-Hertz solution, respectively. It is probable that the convergence rate near the point, $\rho_1 = 1$, in our solution is too slow. Only summing nearly infinite terms could then achieve a good accuracy. In this case, the maximum tensile stress evaluated with a finite number would be underestimated. Besides, the numerical integral in Eq. (3.47) for big n may be not accurate anymore. As a result, there will be a numerical problem to evaluate the maximum tensile stress around $\rho_1 = 1$. As for the FEM simulations, in view of the high stress gradient around $\rho_1 = 1$, it is not strange that the maximum tensile stress

depends on the mesh size to some extent. This does not mean that there is a stress singularity. In other words, the maximum tensile stresses will not always increase with decreasing mesh sizes. The stresses from FEM simulations will be always underestimated with a finite mesh size in principle. Thus, stresses around $\rho_1 = 1$ calculated from the Hüber-Hertz solution are preferred.

There are some numerical programs that deal with fracture mechanics, which depend on the stresses derived from FEM simulation (Gyekenyesi and Nemeth, 1987; Riesch-Oppermann et al., 2008; Ruggieri and Dodds, 1998). We should take care when using such programs to study the failure behavior of single spheres. Stresses with a high accuracy on the sphere surface from the FEM simulation require a very fine mesh size. Furthermore, the maximum tensile stress has a very high gradient along the radial direction. Both will affect the accuracy of results from such programs.

As for stress analysis, all stress components in a sphere can be numerically evaluated. The load positions and ϕ_i or load areas are required in our solution. The spherical coordinate system can be selected almost arbitrarily. The only requirement on the coordinate system is that every load lies within $\phi_i < \theta_i < \pi - \phi_i$ (see Appendix III). The load areas can be obtained from experiments or Hertz theory. For the Hertz theory, it is assumed that the load area is independent of the other loads. By now, all stresses in a sphere can be estimated with our solution. For example, the stresses in spherical pebbles in crush tests can be analyzed by the following steps. First, the load positions have to be specified like (θ, φ) and $(\pi - \theta, \varphi + \pi)$ where θ and φ can be arbitrary angles. Secondly, the load areas measured from experiments are converted to ϕ_1 and ϕ_2. Finally, the stresses under consideration can be solved by our solution with θ, φ, ϕ_1 and ϕ_2. Note that the stresses along $\theta = 0$ and $\theta = \pi$ are not available in our solution because of the artificial singularity, e.g., $\sigma_{r\varphi}$ in Eq. (3.54) and $\sigma_{\theta\varphi}$ in Eq. (3.56). This may not be a problem as an appropriate coordinate system can be normally found. The Hüber-Hertz solution is preferred to calculate the stresses at points around $\rho_1 = 1$ for elastic contacts. For a sphere compressed by various loads, i.e., $N_c > 2$, stress analysis can be performed with a similar procedure as in the above example.

3.4 Summary

In this chapter, an analytical solution for the stresses in an elastic sphere subjected to various loads is derived. The stresses in the sphere can be obtained by summing a finite number of terms in the solution. Two kinds of pressure distributions, uniform or Hertz pressure, are applied in the load areas. The stresses derived with Hertz pressure agree well with the results from FEM simulations where a sphere is compressed by two parallel elastic plates. Other pressure distributions in real contact, if they can be obtained by experiment, theory or simulation, can be applied to our analytical solution as well. The numerical evaluation of our solution clearly shows

the influence of the number N_c of load on stresses inside the sphere. N_c has to be taken into account when the stresses inside a sphere are of big concern.

Our solution can be applied at any points in a sphere in principle. However, a large number of terms needs to be added up to achieve a good convergence at surface points around the boundary of the load area. The Hüber-Hertz solution is then preferred to calculate the stresses at these points.

Chapter 4
Pebble strength characterization

We aim at converting the crush load from crush tests into the pebble-pebble contact strength in pebble beds. Subsequently, the strength will be imported into DEM to simulate the failure of pebbles in pebble beds. An appropriate failure model for pebbles has to be established. The model must be able to interpret the plate influence in the first place. Its applicability should be validated by the comparative experimental results in Chapter 2. It is meaningful if the influence of N_c of contact loads can be incorporated into the model as well.

Several aspects have to be taken into account to establish the failure model. At first, the geometry of pebbles has to be simplified, e.g., spherical shape. Such a simplification is justified for Li_4SiO_4 pebbles as shown in Chapter 2. We will restrict our analysis to the Li_4SiO_4 pebbles in this chapter. The pebbles can be modeled as either mono-sized or multi-sized spheres in principle.

Failure mechanism is one of the most important factors to be considered. It is influenced by flaw type, initial flaw locations and fracture criterion of flaws. The flaw can be crack, pore, void or inclusion (Evans, 1982). Failure can start from surface or volume. The fracture of a single crack can be explained by the Griffith criterion (Griffith, 1921; Irwin, 1957), i.e., fracture occurs when the available energy release rate is greater than or equal to the fracture energy which is considered to be a material property. The crack growth in a component could be *stable* or *unstable*. Stable means that the crack grows to some extent and then stops while the component stays intact. Unstable means that once the flaw starts to grow it will not stop until the whole component fails. The case for stable fracture will be discussed later in this chapter. Moreover, the influence of interaction between flaws is normally ignored.

Finally, different models are proposed under various considerations mentioned above. Some models have a solid physical foundation like the multiaxial Weibull theory (Batdorf and Crose, 1974; Batdorf and Heinisch Jr, 1978; Evans, 1978). On the other hand, some others like Weibull approach are "purely statistical" (Lamon, 1988). The applicability of failure models depends on the consistency between the assumptions and the real case. In general, failure models for brittle material can be classified into two classes based on stress and energy analysis, respectively. The stresses in a sphere have already been derived in Chapter 3. On the other hand, energy absorption of spherical pebbles can be calculated through analytical solutions, such as the Hertz theory, or FEM simulation. Accordingly, the applicability of various existing failure models for ceramic

41

materials will be verified for Li_4SiO_4 pebbles. We use the material parameters in Table 2.1 in this chapter. Besides, all quantities with a superscript AL or WC or BK7 indicate the crush tests in Chapter 2 using AL or WC or BK7 plates, respectively.

4.1 Multi-sized models

The strength of brittle particles can be characterized in terms of size in principle. For example, Jaeger (1967) concluded that failure of rock particles would occur when $F_c/D^2 = \sigma_c$ where D is the particle size. The characteristic stress σ_c is defined as the strength which is a material constant. The failure load F_c is thus proportional to the square of the particle size, and the strength is the same when the particles have an identical size. Some probabilistic models based on this concept have been developed to characterize the strength scatter of spherical particles with different sizes, e.g., McDowell and Amon (2000). However, this concept and related probabilistic models are not applicable for the Li_4SiO_4 pebbles. According to Fig. 2.3, the strength of pebbles for almost the same size has a large standard deviation, which is against the assumption of unique strength for the same size of particles. On the other hand, the strength F_c/D^2 is almost independent of size. Therefore, as concluded in Chapter 2, the concept that mono-sized Li_4SiO_4 spheres have a strength distribution is preferred for the strength analysis.

4.2 Mono-sized models

There are two fundamental aspects for models for mono-sized particles, i.e., the representative size of pebbles and the strength distribution function. Most pebbles have a size ranging $0.44 < D_m < 0.56$ mm in our crush tests. As the size of pebbles crushed at FML was not measured, a nominal size 0.5 mm was simply given. The pebble size or diameter is set to $D = 0.5$ mm in this chapter. Some distributions, such as the Weibull distribution and the normal distribution, have been examined in the view of goodness of fit (Doremus, 1983; Lu et al., 2002a). It is concluded that the Weibull distribution was not always preferred to the other distributions. Nevertheless, the Weibull distribution is the most frequently used one in probabilistic fracture mechanics. There are two main reasons. At first, the parameters in the distribution can be assigned to physical meaning with the help of fracture mechanics. It is widely accepted that failure of brittle materials at stresses far below their theoretical strength is due to the presence of microflaws. Weibull (1939) has firstly elucidated the relation between the microflaws and ultimate strength with the Weibull distribution. The basic assumptions include weakest link, no interaction between flaws, flaw size distribution and fracture criterion of the microflaws. Many probabilistic models are subsequently developed based on these assumptions. Much effort has been made on specifying the flaw size, e.g., shape and size distribution, and proper fracture criteria. Secondly, Weibull (1951) showed the

applicability of the Weibull distribution to a wide field of problems, such as the yield strength of a Bofors steel, where the Weibull distribution was purely statistically applied without any physical basis. It was suggested by Weibull that the distribution was not always valid and should be tested empirically. For strength analysis for a brittle material, applying the Weibull distribution purely statistically, namely Weibull approach, is popular because of its ease of application. Furthermore, this approach can often be validated by experiments despite the criticism that it lacks any physical basis (Lamon, 1988).

In this section, various failure models are used to investigate the plate influence on the crush load. The common validation method is as follows. For a given model, its parameters are derived with the crush loads for AL plates, and a prediction is made for WC plates with its variables and the derived parameters for AL plates. On the other hand, the parameters can be derived with the crush loads for WC plates, and a prediction is made for AL plates with its variables and the derived parameters for WC plates. Finally, when both predictions agree with the corresponding experimental result at the same time the model is considered to be validated. When a probabilistic model is used, its parameters are derived by fitting the corresponding crush load distribution using the least square method.

4.2.1 Uniform strength

Although there is no consensus on the failure mechanism for brittle spheres, the tensile stress is normally assumed to dominate the failure. However, there are two views about the position of the stress, i.e., inside the sphere or on the surface (Darvell, 1990). For instance, it is assumed that the failure of spheres is dominated by the maximum tensile stress inside the sphere by many researches. In the work of Chau et al. (2000); Hiramatsu and Oka (1966)), it is assumed that spheres will fail when the maximum tensile stress inside the sphere σ_{vmax} reaches the critical stress which is a material parameter. In this section, we also assume that there is a characteristic stress σ_{c} for Li_4SiO_4 pebbles and its scatter is ignored. Pebbles fail when the maximum tensile stress σ_{vmax} inside the pebble reaches the characteristic stress, i.e., $\sigma_{\mathrm{vmax}} = \sigma_{\mathrm{c}}$. This model is validated when $\sigma_{\mathrm{vmax}}^{\mathrm{AL}} = \sigma_{\mathrm{vmax}}^{\mathrm{WC}} = \sigma_{\mathrm{c}}$ holds for AL and WC plates.

For the uniaxial loading on a sphere (see Fig. 3.4), it is found that the maximum tensile stress along the loading axis is also the maximum tensile stress inside the sphere from our solution. Moreover, it is known from our solution that σ_{vmax} is proportional to F/D^2, namely $\sigma_{\mathrm{vmax}} = cF/D^2$, where c should be a constant depending the type of load. For example, c^{AL} for AL plates and c^{WC} for WC plates should be two different constants. The relation $\sigma_{\mathrm{vmax}} = \sigma_{\mathrm{c}}$ requires that $F_{\mathrm{c}}/D^2 = \sigma_{\mathrm{c}}/c$ has to be two different constants for AL and WC plates, respectively. If F_{c}/D^2 obtained in experiments for either plates is not a constant, the assumption $\sigma_{\mathrm{vmax}} = \sigma_{\mathrm{c}}$ for pebbles is violated. As seen in Fig. 2.3, the average stress F_{c}/D^2 for both plates is approximately a

constant, that is, $F_c^{AL}/D^2 \approx 43\,\text{MPa}$ and $F_c^{WC}/D^2 \approx 30\,\text{MPa}$. The assumption of $\sigma_{vmax} = \sigma_c$ is satisfied. The next step is then to validate whether $\sigma_{vmax}^{AL} = \sigma_{vmax}^{WC}$ hold for both plates.

As shown in Table 2.2 the average crush loads for both plates are $F_c^{AL} = 10.6$ N and $F_c^{WC} = 7.55$ N, respectively. Under the assumption of elastic deformation for pebbles and plates, it turns out that $F_c^{AL} = 10.6$ N corresponds to $\phi_1 = \phi_2 = 8.24°$ with $\sigma_{vmax}^{AL} = 51.0$ MPa (calculated from our analytical solution based on the Hertz theory), and $F_c^{WC} = 7.55$ N corresponds to $\phi_1 = \phi_2 = 5.85°$ with $\sigma_{vmax}^{WC} = 55.4$ MPa. Note that the difference between σ_{vmax}^{AL} and σ_{vmax}^{WC} is about 8%.

It is found in our analytical solution that compared to the Hertz pressure the uniform pressure gives rise to smaller stresses for the same load F and sphere radius R (see Fig. 3.6). When the potential plastic deformation of the soft AL plate is taken into account, it is expected that the load area will increase and pressure will be distributed more uniformly compared to the Hertz pressure for elastic contact for the same load. Accordingly, the maximum tensile stress inside the pebble will decrease to some extent (see Fig. 4.11 below). The difference between σ_{vmax}^{AL} and σ_{vmax}^{WC} will be then much larger than 8%. This difference suggests that the assumption of $\sigma_{vmax}^{AL} = \sigma_{vmax}^{WC}$ is not reasonable.

4.2.2 Non-uniform strength distribution

The strength is assumed to have a non-uniform strength distribution such that the scatter of pebble strength can be taken into account. For example, Munz and Fett (1999) have derived the strength distribution P_s for a brittle component

$$P_s = 1 - \exp\left[-\left(\frac{\sigma_c}{\sigma_0}\right)^m\right], \tag{4.1}$$

where

$$m = 2(r-1), \quad \sigma_0 = \frac{K_{Ic}}{Y\sqrt{a_0}Z^{1/m}}, \quad \sigma_c = \frac{K_{Ic}}{Y\sqrt{a}}. \tag{4.2}$$

Here r is a constant characterizing the flaw size distribution $P_a(a)$ which is a material property, K_{Ic} is the fracture toughness, Y is a geometry factor accounting for flaw shape, a_0 is a normalization factor which can be taken as a material parameter, and Z is the number of flaws either inside the component or on the component surface depending on where the failure starts. For the same material, $P_a(a)$, K_{Ic}, Y and a_0 are the same. If the components made of the same material have the same shape and size, such as the pebbles in both tests, Z will be also a constant when the failure starts on the same location. Assuming the failure for pebbles starts on their surface, m and σ_0 are then constants for the pebbles according to Eq. (4.2). In this section, the maximum tensile stress σ_{smax} on pebble surface is taken as the characteristic stress, namely $\sigma_c = \sigma_{smax}$. Moreover, it is assumed that the same σ_c leads to the same failure probability of pebbles for both plates,

The relation between σ_c and the contact load F is given by

$$\sigma_c = \sigma_{\mathrm{smax}} = \left(\frac{6FE^{*2}}{\pi^3 R^{*2}}\right)^{\frac{1}{3}} \tag{4.3}$$

according to the Hertz theory, where E^* is the equivalent Young's modulus, and R^* is the radius of relative curvature. They are defined as

$$\frac{1}{E^*} = \frac{1 - \nu_1^2}{E_1} + \frac{1 - \nu_2^2}{E_2}, \quad \frac{1}{R^*} = \frac{1}{R_1} + \frac{1}{R_2} \, . \tag{4.4}$$

Here E_1 and E_2 are Young's moduli, and ν_1 and ν_2 are Poisson's ratios of the two contacting bodies, respectively. R_1 and R_2 are the radii of curvature of the two contacting bodies, respectively. By plugging Eq. (4.3) in the condition $P_s(\sigma_c^{\mathrm{AL}}) = P_s(\sigma_c^{\mathrm{WC}})$, the relation

$$\frac{F^{\mathrm{AL}}}{F^{\mathrm{WC}}} = \left(\frac{E^{*\mathrm{WC}}}{E^{*\mathrm{AL}}}\right)^2 = 3.9 \tag{4.5}$$

can be used for prediction for crush load probability. For example, $F^{\mathrm{AL}} = 3.9$ N and $F^{\mathrm{WC}} = 1$ N correspond to the same failure probability because of the same σ_c induced by F^{AL} and F^{WC}, respectively. Note that Eq. (4.5) is derived without any information about the distribution form. It could be the example of Eq. (4.1) or any other distributions as long as the only variable is σ_{smax} and the parameters in the distribution are the same for both plates.

Accordingly, for any crush load probability $P_s(F_{ci})$ shown in Figure 2.4 the prediction for the other one is made according to Eq. (4.5) for the same P_s.

Figure 4.1: Comparison of crush load probability of experiments and the corresponding predictions. It is assumed that the same maximum tensile stress on pebble surface leads to the same failure probability.

Fig. 4.1 shows the comparison between the predictions and experimental results. Note that the prediction for AL plates is made with P_s^{WC} in Fig. 2.4 and Eq. (4.5), and the prediction for WC plates is made with P_s^{AL} in Fig. 2.4 and Eq. (4.5). It seems that the stress influence has

been greatly exaggerated. If the potential plasticity of plates is taken into account, F^{AL}/F^{WC} will be larger than 3.9 for the same σ_c. It is thus foreseen that the difference between prediction and corresponding experiments will become larger, meaning this model not useful to describe the influence of the plate material.

4.2.3 Three parameter strength distribution

The threshold load F_u or stress σ_u below which no failure occurs can be theoretically introduced into Eq. (4.1). The flaw size distribution

$$P_a(a) = 1 - \left(\frac{a_0}{a}\right)^{r-1} \tag{4.6}$$

has been used by Munz and Fett (1999). The flaw size distribution P'_a proposed in this section is

$$P'_a(a) = \begin{cases} 1 - \left(\frac{a_0}{a}\right)^{r-1} + \left(\frac{a_0}{a_u}\right)^{r-1} & a \leqslant a_u \\ 1 & a > a_u , \end{cases} \tag{4.7}$$

where a_u is a parameter corresponding to the possible maximum size of flaws. This formulation takes into account that any preexisting flaw size in excess of the particle dimension is impossible. The difference between Eq. (4.6) and (4.7) is very small since a_0 is much smaller than a_u in general. Figure 4.2 shows the flaw size distributions. The strength distribution is finally derived as (see Appendix VI)

$$P_s(F) = \begin{cases} 1 - \exp\left[-\left(\frac{F}{F_1}\right)^{\frac{1+m}{3}} + \left(\frac{F}{F_2}\right)^{\frac{1}{3}}\right] & F \geqslant F_u \\ 0 & F < F_u , \end{cases} \tag{4.8}$$

where F_1, m, F_2 are material parameters given by

$$F_1 \propto \left(\frac{E^*}{R^*}\right)^{\frac{1-2m}{1+m}} , \quad F_2 \propto \frac{E^*}{R^*}\sigma_u^{-3m} . \tag{4.9}$$

We assume that the Weibull modulus m and the threshold stress σ_u are material constants. As a result of this assumption, F_u depends on the material parameters of two bodies in contact according to Eq. (4.9).

The validation is as follows. The parameters m^{WC}, F_1^{WC} and F_2^{WC} are obtained by fitting the crush load distribution for WC plates in Fig. 2.4 using Eq. (4.8). m^{WC} is assumed to be a constant representing the pebble material alone, and so $m^{AL} = m = m^{WC}$ for AL plates. Prediction of crush load probability for AL plates is made with the parameters F_1^{AL} and F_2^{AL}, which are derived with the relations

$$F_1^{AL} = \left(\frac{E^{*AL}}{E^{*WC}}\right)^{\frac{1-2m}{1+m}} F_1^{WC} , \quad F_2^{AL} = \frac{E^{*AL}}{E^{*WC}} F_2^{WC} \tag{4.10}$$
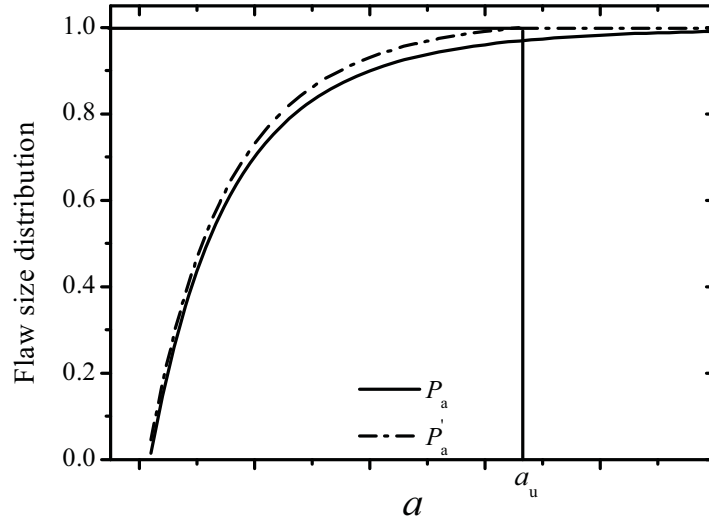
Figure 4.2: Flaw size distribution P_a adopted by Munz and Fett (1999) and proposed flaw size distribution P_a'.
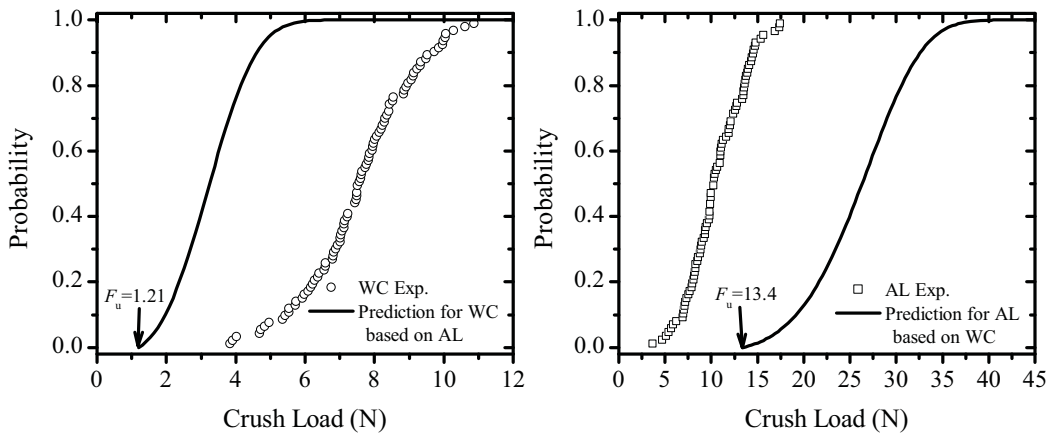
Figure 4.3: Comparison of crush load probability of experiments and the corresponding predictions. The threshold load is introduced into the Weibull distribution of Eq. (4.1) with the modified flaw size distribution P_a'.

according to Eq. (4.9) for the same R^*. The prediction is shown in Fig. 4.3 (right). The predicted threshold load is $F_u^{AL} = 13.4$ N. The prediction of crush load probability for WC plates with parameters derived from fitting parameters for AL plates is also plotted Fig. 4.3 (left). The predicted threshold load is $F_u^{WC} = 1.21$ N. Both the predictions do not agree with the corresponding experimental results. The introduction of the threshold load does not decrease the difference between predictions and corresponding experiments compared to the model in Section 4.2.2. This model is not applicable either.

4.2.4 Weibull approach

The general form of the Weibull distribution to characterize the strength of brittle materials is

$$P_{\text{s}} = 1 - \exp[-B] = 1 - \exp\left[-\int_x n(\sigma_{\text{c}}) dx\right],$$ (4.11)

where the dimensionless parameter B is defined as the risk of rupture by Weibull (1939). The integration domain depends on where failure starts. $\sigma_{\text{c}}(x)$ is a function of characteristic stress, e.g., the maximum tensile stress, at each point in the domain, which is independent of loading history. $n(\sigma_{\text{c}})$, a function characterizing the flaw distribution, is normally given by

$$n(\sigma_{\text{c}}) = \begin{cases} \left(\frac{\sigma_{\text{c}} - \sigma_{\text{u}}}{\sigma_0}\right)^m & \sigma_{\text{c}} \geqslant \sigma_{\text{u}} \\ 0 & \sigma_{\text{c}} < \sigma_{\text{u}} . \end{cases}$$ (4.12)

Jelagin and Larsson (2008) studied the failure initiation of glass plate indented by a spherical indenter with Eqs. (4.11) and (4.12). They assumed that the failure of glass is dominated by the maximum tensile stress $\sigma_{\text{c}}^{\text{h}}$ experienced by each points on the plate surface in loading history. The risk of rupture reads as

$$B = \int_0^\infty n\left(\sigma_{\text{c}}^{\text{h}}(F_{\text{c}}, \rho_1)\right) 2\pi \rho_1 d\rho_1,$$ (4.13)

where ρ_1 is a normalized distance from the contact area center on the plate. F_{c} is the maximum load loading from zero. Moreover, the threshold load σ_{u} is set to zero.

In our case, the crush load of spherical pebbles is of concern rather than the plate. The method used by Jelagin and Larsson (2008) can be extended to our case in principle, i.e, the risk of rupture of Eq. (4.13) is calculated over the maximum tensile stress $\sigma_{\text{c}}^{\text{h}}$ experienced at each point on the pebble surface instead of the plate surface as

$$B = \int_0^{\pi/2} n\left(\sigma_{\text{c}}^{\text{h}}(F_{\text{c}}, \rho_1)\right) 2\pi \rho_1^2 \sin \phi d\phi,$$ (4.14)

where $\rho_1 = R\phi/R_{\text{a}}$ is a normalized distance from the contact area center on the pebble surface as shown in Fig. 3.10. As a result, the crush load probability reads as

$$P_{\text{s}} = \begin{cases} 1 - \exp\left[-\int \left(\frac{\sigma_{\text{c}}^{\text{h}}(F_{\text{c}}, \rho_1) - \sigma_{\text{u}}}{\sigma_0}\right)^m 2\pi \rho_1^2 \sin \phi d\phi\right] & \sigma_{\text{c}}^{\text{h}} \geqslant \sigma_{\text{u}} \\ 0 & \sigma_{\text{c}}^{\text{h}} < \sigma_{\text{u}} , \end{cases}$$ (4.15)

where $\sigma_{\text{u}}, \sigma_0$ and m are material parameters. The threshold strength σ_{u} is set to zero in this section. Thus, there are only two fitting parameters, namely σ_0 and m in Eq. (4.15).

Figure 4.4 shows the difference between σ_{c} for a current load of 4 N and $\sigma_{\text{c}}^{\text{h}}$ for a maximum load of 4 N loading from zero on the pebble surface for WC plates. For an elastic contact, the maximum tensile stress σ_{smax} on the surface of pebble is proportional to the radius of load circle R_{a}, that is,

$$\sigma_{\text{smax}} = \sigma_{\text{c}}^{\text{h}}(R_{\text{a}}) = \frac{2E^*}{\pi R^*} R_{\text{a}}$$ (4.16)

according to the Hertz theory. Therefore, during the loading history, i.e., the load from zero to 4 N in Fig. 4.4, a linear relation between the $\sigma_c^h(\rho_{1\max})$ and ρ_1 in the range of $0 \leqslant \rho_1 < \rho_{1max}$ is used in Fig. 4.4 ($\rho_1 = R\phi/R_a$ as defined in Fig. 3.10). The current $\sigma_{\mathrm{smax}} = \sigma_c^h(\rho_{1\max})$ on surface, which is calculated from FEM simulations, lies a little outside of the contact circle, i.e., $\rho_{1\max} > 1$. The stress outside the load circle is calculated from FEM simulations where the friction between pebbles and plates is not taken into account. The σ_c^h can be obtained from FEM simulation for every crush load F_{ci} in our crush tests. The fitting parameters, namely σ_0 and m in Eq. (4.15) for AL plates can be derived with the crush probability $P_s(F_{ci}^{\mathrm{AL}})$ in Fig. 2.4 and the $\sigma_c^h(F_{ci}^{\mathrm{AL}})$ distributions. Crush load probability prediction for WC plates is then determined with the derived fitting parameters for AL plates and the $\sigma_c^h(F^{\mathrm{WC}})$ distributions for WC plates. Similarly, the fitting parameters for WC plates are derived with the crush probability $P_s(F_{ci}^{\mathrm{WC}})$ in Fig. 2.4 and the $\sigma_c^h(F_{ci}^{\mathrm{WC}})$ distribution. The prediction for AL plates is then obtained with the derived fitting parameters for WC plates and the $\sigma_c^h(F^{\mathrm{AL}})$ distributions for AL plates. Comparison is made between predictions and corresponding experimental results in Fig. 4.5. It can be seen
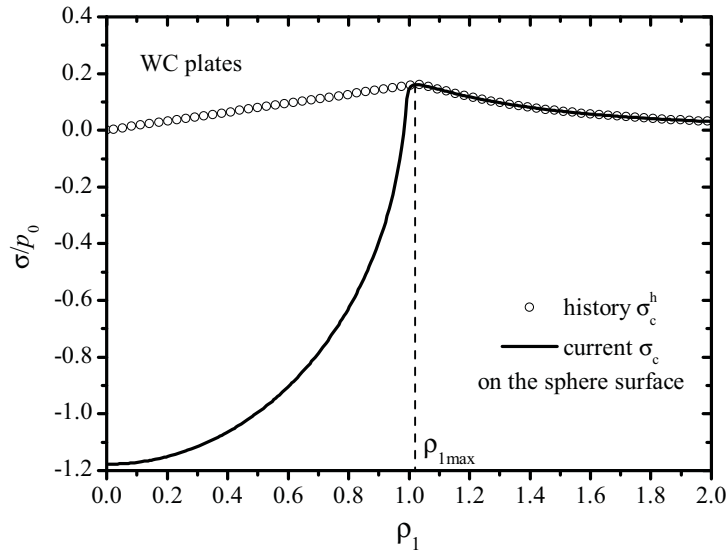
Figure 4.4: History σ_c^h during loading up to 4 N and the current σ_c for WC plates. $p_0 = F/(\pi R_a^2)$ is the mean pressure in the contact circle. $\rho_{1\max}$ is the position where the current maximum σ_{smax} lies. The stresses for $\rho_1 \geqslant \rho_{1\max}$ is obtained from FEM simulation with a surface mesh size 0.125 μm while friction and plasticity is not considered.

that the agreement between prediction and the corresponding experimental result is even worse than for the methods in former sections. The influence of the maximum tensile stress seems to be more exaggerated. Hence, this model is not applicable either.

The σ_c^h on surface is derived from FEM simulations, which is smaller compared to the one calculated from the Hertz theory as shown in Fig. 3.10. It is not clear if the underestimated σ_c^h from FEM simulation has an effect on this model. On the other hand, it is concluded in Chapter 3
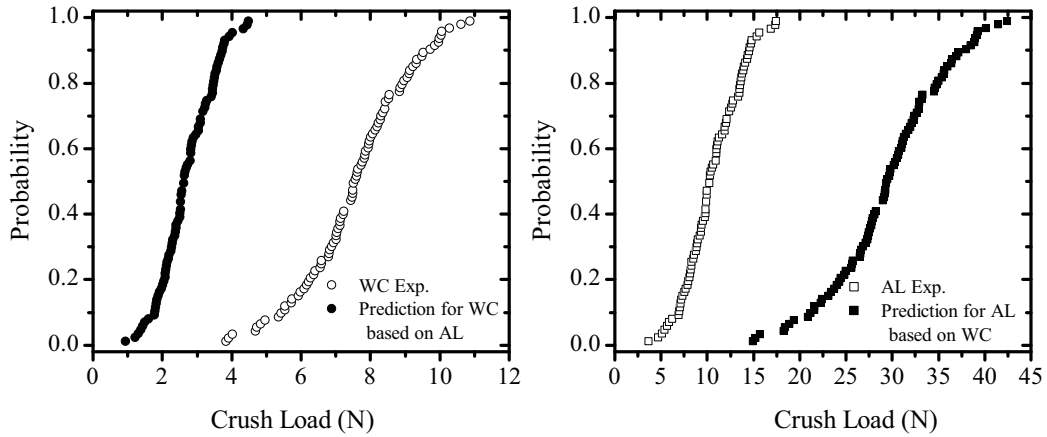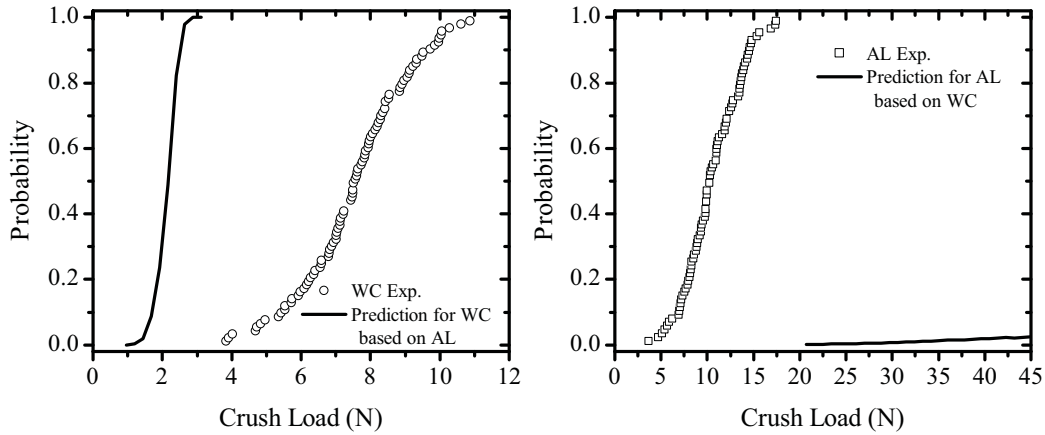
Figure 4.5: Comparison of crush load probability of experiments and the corresponding predictions. It is assumed that the strength of pebbles is dominated by the maximum tensile stress experienced on pebble surface.

that the Hertz theory is preferred to calculate the maximum tensile stress σ_{smax} on surface. Hertz (1881) assumed that each contact body can be regarded as an elastic half-space. Based on this, Hüber (1904) derived the stresses inside the half space. For an elastic contact between a sphere, which is apparently not a half-space, and a plate, the stresses calculated from the Hüber-Hertz solution at points which are far away from the contact area on the sphere side are not reliable any more. Therefore, the maximum tensile stress outside the load area on surface i.e., $\rho_1 > \rho_{1max}$ in Fig. 4.4, cannot be calculated from the Hüber-Hertz solution.

Jelagin and Larsson (2008) have shown the influence of friction on the failure load of brittle plates. Correspondingly, the friction should also play a role in the crush load of ceramic pebbles. However, the friction between plates and pebbles is unknown. The influence of friction on the failure criterion will be discussed later.

4.2.5 Multiaxial Weibull theory

The Weibull parameters σ_0 and m in Eq. (4.1) have been assigned an explicit physical meaning. However, the relation between σ_c and flaw size a in Eq. (4.2) should be not valid in a non-uniform stress field, e.g., high stress gradient around the contact area between pebbles and plates. The multiaxial Weibull theory aims at characterizing the failure of brittle components in a general load case. In other words, assumptions more consistent with practical case are applied in this theory, e.g., flaws have not only random size but also random orientation. The Weibull modulus m is also considered as a material constant characterizing the flaw size distribution. In practice, it is normally derived from simple failure tests like bending test. The other parameter σ_0 depends on the failure criterion, component geometry and loading condition. For a component subjected to

multiaxial loads, the relation between σ_0 and material constants like K_{Ic} will be complex. When the failure of component is dominated by surface flaws the risk of rupture reads as (Brückner-Foit et al., 2000)

$$B = \frac{1}{S_0} \int_S \frac{1}{2\pi} \int_\Omega \left(\frac{\sigma_{\text{eq}}}{\sigma_0'} \right)^m d\Omega dS \,, \tag{4.17}$$

where S indicates surface. S_0 indicates a unit surface area. Ω is the orientation of surface flaws. σ_{eq} is a scalar equivalent stress which is derived with the stress field in the component, usually from FEM simulation, and the selected failure criterion. σ_0' is a material constant for surface flaws.

The risk of rupture in Eq. (4.17) has been implemented into the software package, namely STAU, developed at KIT (Riesch-Oppermann et al., 2008). It is a postprocessor using the stress field from FEM simulation to calculate the failure probability of brittle materials. Surface flaws are modelled as Griffith cracks. Moreover, the risk of rupture for volume failure is also implemented into STAU. Volume flaws are modelled as randomly oriented penny-shaped cracks. The stress at any point $\sigma(x, y, z)$ in the component can be written as

$$\sigma(x, y, z) = \sigma^* g(x, y, z) \,, \tag{4.18}$$

where σ^* is a reference stress characterizing the load level, and g is a geometry function. Substituting Eq. (4.18) into (4.17), the risk of rupture can be reduced to

$$B = \left(\frac{\sigma^*}{b} \right)^m \,, \tag{4.19}$$

where

$$b = \sigma_0' H_S^{-1} = \sigma_0' \left[\frac{1}{S_0} \int_S \frac{1}{2\pi} \int_\Omega \left(\frac{\sigma_{eq}}{\sigma^*} \right)^m d\Omega dS \right]^{-\frac{1}{m}} \,. \tag{4.20}$$

Here H_S is a integral value which is calculated from STAU using the stress field from FEM simulation. Care should be taken that b is a constant only when H_S is independent of load levels. Otherwise, the strength distribution has to be written as

$$P_s = 1 - \exp \left[- \left(\frac{\sigma^*}{\sigma_0' H_S^{-1}(\sigma^*)} \right)^m \right] = 1 - \exp \left[- \left(\frac{\sigma_c}{\sigma_0'} \right)^m \right] \,, \tag{4.21}$$

where $\sigma_c = \sigma^* H_S$ is the characteristic stress which can be calculated from STAU. In view of the expression of H_S in Eq. (4.20), σ_c is independent of σ^* which is introduced in STAU for numerical reason.

In a general case, suppose that b in Eq. (4.20) is independent of load levels, strength prediction for the considered component can be made as follows. For a brittle material, m and b_1 are obtained from a simple failure test. H_{S1} is calculated with the stress field corresponding to this simple load case. A component made of the same material is subjected to different multiaxial loads.

51

The prediction for its failure probability can be made with the Weibull parameters m and $b_2 = b_1 H_{S1}/H_{S2}$. H_{S2} is calculated with the stress field in the component.

The Weibull modulus m for Li_4SiO_4 pebbles cannot be derived because the bulk material for a simple test is not available. As a result, we are not able to predict the failure probability of pebbles. Moreover, the existence of the reference stress σ^* for pebbles is questionable. A constant b in Eq. (4.18) requires that the ratio between stresses at two different points should be independent of the load level, namely σ^*, which would be typical of a linear system. The proportionality is a geometric function

$$\frac{\sigma(x_1, y_1, z_1)}{\sigma(x_2, y_2, z_2)} = \frac{g_1(x_1, y_1, z_1)}{g_2(x_2, y_2, z_2)} . \tag{4.22}$$

For an elastic sphere subjected to uniaxial loading (see Fig. 3.4), the maximum principal stresses $\sigma_1^{'}$ and $\sigma_1^{''}$ at two points $\rho = 0$ and $\rho = 0.81$, respectively, along the loading axis are calculated with our analytical solution for Hertz pressure boudnary condition. Two different load levels, $\phi_i = 5°$ and $3°$ are compared. It turns out that $\sigma_1^{''}/\sigma_1^{'} = 2.88$ for $\phi_i = 5°$ while $\sigma_1^{''}/\sigma_1^{'} = 4.47$ for $\phi_i = 3°$. The two ratios are different, which manifests that there is no such a σ^* for the elastic sphere. This deviation from linear behavior stems from the nonlinear change of the contact area as the load is increased. Consequently, b in Eq. (4.19) will not be a constant for spherical pebbles subjected to different load levels.

Attention should be paid that there are many different failure criteria implemented in STAU. Different criterion will lead to different H. It is difficult to tell which one is suitable for pebbles. Moreover, the failure of pebbles can start from volume or surface, corresponding to H_V and H_S, respectively. Finally, the friction between pebbles and plates is unknown while it is found that H is very sensitive to the friction coefficient between pebbles and plates because of its significant influence on the stress field. The influence of plate material on the crush load cannot be investigated by the complicated multiaxial Weibull theory without the above information.

4.2.6 Energy model

The above models for brittle failure are based on stress criteria. There are also some models based on energy criteria. For example, a Weibull distribution model in terms of absorbed energy by a particle has been recently developed. This model was first used to interpret the failure of particles in impact comminution (Vogel and Peukert, 2002, 2003, 2004). In these analyses, the kinetic energy of flying particles was completely transformed into the absorbed energy of the particle, i.e., a rigid plate is assumed. The applicability of the model even for slow compression comminution was validated by Toneva and Peukert (2007). Meier et al. (2009) have taken into account the influence of plate deformation on the particle energy absorption. According to Toneva

and Peukert (2007), the strength distribution of particles for slow compression reads as

$$
P_{\mathrm{s}} = \begin{cases} 1 - \exp\left[- f_{\mathrm{Mat}} x \left(W_{\mathrm{c}} - W_{\mathrm{u}} \right) \right] & W_{\mathrm{c}} \geqslant W_{\mathrm{u}} \\ 0 & W_{\mathrm{c}} < W_{\mathrm{u}} , \end{cases} \tag{4.23}
$$

where f_{Mat} is a material parameter describing the resistance of particles against failure, x is the initial particle size ($x = D$ for spherical pebbles), W_{c} is a variable for absorbed energy of the particle, and W_{u} is a material parameter characterizing the minimum energy required for failure.

Toneva and Peukert (2007) took the area under the recorded force-deformation curve in slow compression tests as the absorbed energy W_{c} of the particle, which means that the plates would not absorb energy at all. In practice, the actual energy stored in the particle can be calculated for spherical elastic particles using the Hertz theory. When plasticity occurs in the plates, the energy absorbed by the particle can be derived from FEM simulation. The actual energy W_{c} absorbed by the particle in this section is either from the Hertz theory or FEM simulation.
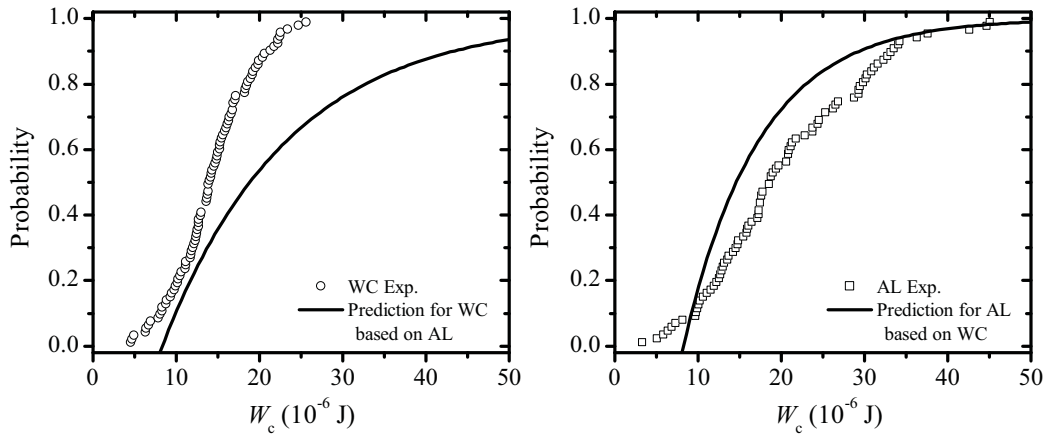
Figure 4.6: Comparison of crush load probability of experiments and the corresponding predictions. The energy model of Eq. (4.23) is used. The absorbed pebble energy is calculated from Hertz theory.

The crush load probability $P_{\mathrm{s}}(W_{ci})$ can be derived from $P_{\mathrm{s}}(F_{ci})$ in Fig. 2.4 using the relation between W_{ci} and F_{ci}. For example, for an elastic contact between a sphere and a plate, the energy absorbed by the sphere can be calculated from Hertz theroy (see Appendix VII). In Fig. 4.6 W_{ci} for spherical pebbles, which is derived from the Hertz theory, corresponds the experimental value F_{ci}. The prediction for WC plates is made with W_c^{WC} and the fitting parameters $f_{\mathrm{Mat}}^{\mathrm{AL}}$ and $W_{\mathrm{u}}^{\mathrm{AL}}$ for AL plates. On the other hand, the prediction for AL plates is made with W_c^{AL} and the corresponding fitting parameters for WC plates. As previously stated, the model is validated only when predictions agree the corresponding experimental results at the same time. The prediction for AL plates is close to the crush load distribution for AL plates. On the other hand, the predicted crush load probability for WC plates is much smaller than the experimental result especially for

bigger W_c^{WC}. In view of the agreement between the predictions and corresponding experimental results, this model is better than the other models in the previous sections.
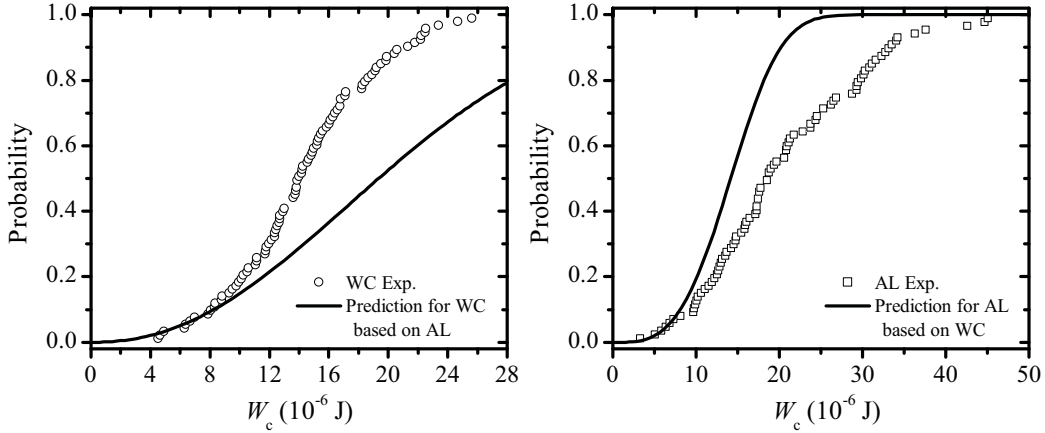
Figure 4.7: Comparison of crush load probability of experiments and the corresponding predictions. The energy model of Eq. (4.24) is used. The absorbed pebble energy is calculated from Hertz theory.
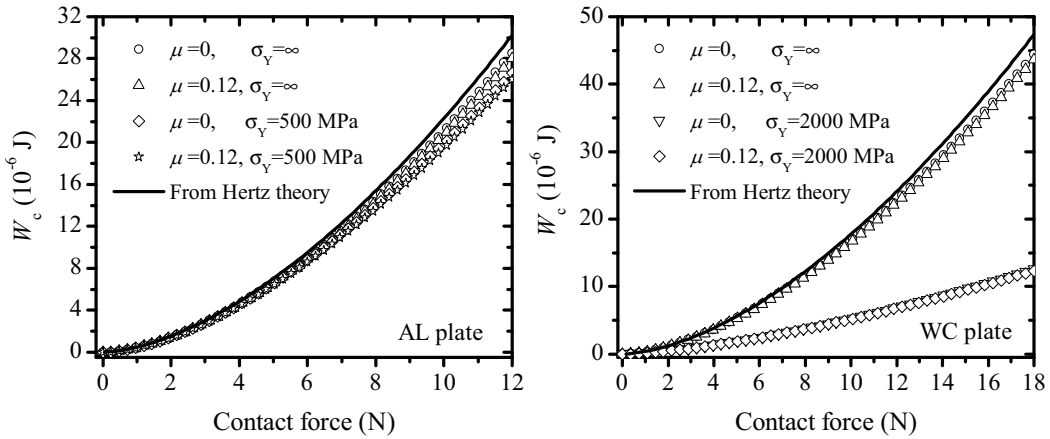
Figure 4.8: The influence of friction and plate plasticity on the energy absorption of pebbles.

The shape of the distribution in Eq. (4.23) is fixed because the Weibull modulus is set to 1. The consequence is that the derivative of P_s alway decreases. This tendency is not consistent with the actual distribution especially for WC plates. Relaxing the restriction on the Weibull modulus can minimize the inconsistency. Therefore, the strength distribution function

$$P_s = 1 - \exp\left[-\left(\frac{W_c}{W_{\text{Mat}}}\right)^m\right] \tag{4.24}$$

is proposed. In this expression, the particle size, which is the same in both tests, is included in W_{Mat} as a factor and is no longer written explicitly.

Figure 4.7 shows the predictions with respect to W_c which is also derived from the Hertz theory. The agreement for small load has improved compared to Fig. 4.6. Anyhow, there is still

a big difference between predictions and the corresponding experimental results for big loads for fitting to both types of experiments.

Figure 4.8 shows the influence of interface friction and potential plasticity of the plates on the absorbed energy of a elastic sphere from FEM simulations. The Hertz result (see Appendix VII) is also shown. Here, μ is the friction coefficient in the contact area, and σ_Y is the Mises yield stress. A perfect plasticity model is used in FEM simulations. The Mises yield stress is set to $\sigma_Y = 2000$ MPa for WC plates and $\sigma_Y = 500$ MPa for AL plates, respectively. The minor difference of W_c calculated from Hertz theory and the corresponding FEM simulation ($\mu = 0, \sigma_Y = \infty$) for big contact force should be due to the large deformation of the plates and sphere. The assumption of small deformation of the contacting bodies in Hertz theory does not hold any longer in this situation. Friction has little influence for both plates irrespective of the consideration of plasticity. Consequently, although we are not able to measure the friction between plates and pebbles in our crush tests, the energy model can be applied to study the plate influence irrespective of the actual friction. Finally, the plasticity of the soft AL plates significantly decreases the energy absorbed by the sphere. Therefore, it is helpful to know whether the agreement becomes better when plasticity of plates is taken into account.
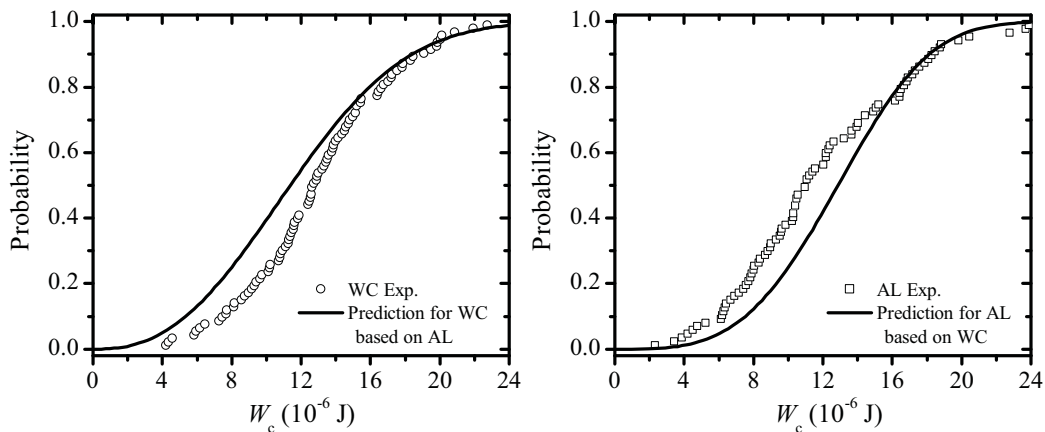
Figure 4.9: Comparison of crush load probability of experiments and the corresponding predictions. The energy model of Eq. (4.24) is used. The absorbed pebble energy is obtained from FEM simulation.

The predictions and corresponding $P_s(W_c)$ are shown in Fig. 4.9 where W_{ci}^{WC} for WC plates is derived from FEM simulation for $\mu = 0$ and $\sigma_Y = 2000$ MPa while W_{ci}^{AL} for AL plates is derived for $\mu = 0$ and $\sigma_Y = 500$ MPa. It can be clearly seen that the agreement has greatly improved for both plates at the same time. This validates the proposed distribution of Eq. (4.24) in terms of absorbed energy.

The main objective of our crush tests in Chapter 2 and the failure analysis of pebbles in this chapter is to find a model which can describe the plate influence on the crush load. Finally, the

proposed energy model in Eq. (4.24) can describe the plate influence, and the pebble-pebble contact strength can be derived with this model subsequently. Moreover, the influence of coordination number of contact loads can be quantitatively incorporated in the model. Assuming that the strain energy for each contact on a pebble is independent of each other, the absorbed energy of the pebble is the summation of the strain energy for every contact. Thus, the influence of the magnitude of every contact load is considered while the influence of load direction is ignored.

4.3 Pebble-pebble contact strength
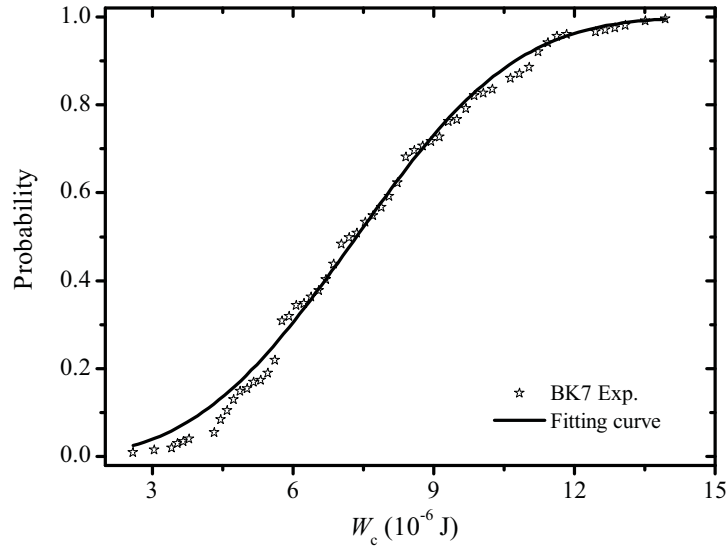
Figure 4.10: The energy strength distribution of conditioned pebbles from the batch OSi 07/1.

The pebble-pebble contact strength of pebbles will be derived from the crush load data from FML, so that the fusion relevant environment with dry inert gas is taken into account. Figure 4.10 shows the energy strength distribution, i.e., pebble absorbed energy distribution. The energy W_c^{BK7} is calculated from Hertz theory for BK7 glass. The fitting function of the energy distribution is then taken as the pebble-pebble contact strength.

The energy strength distribution, namely the fitting function, of Li_4SiO_4 pebbles is

$$P_s = 1 - \exp\left[-\left(121116W_c\right)^{3.17}\right]. \tag{4.25}$$

The corresponding probability denstity function (PDF) reads as

$$p_s = P_s' = 4.12 \times 10^{16} W_c^{2.17} \exp\left[-\left(121116W_c\right)^{3.17}\right]. \tag{4.26}$$

Each pebble in pebble beds will be thus assigned to a critical energy randomly according to this distribution. When any pebble absorbs more energy than its critical energy it fails. The pebble strength can be accordingly incorporated into DEM simulations. Note that Eq. (4.25) corresponds

to the critical strength distribution of pebbles from the batch of OSi 07/1. It might not be valid for pebbles from other batches for which a new fitting of the parameters W_{Mat} and m will be necessary.

4.4 Discussion

4.4.1 Failure mechanism
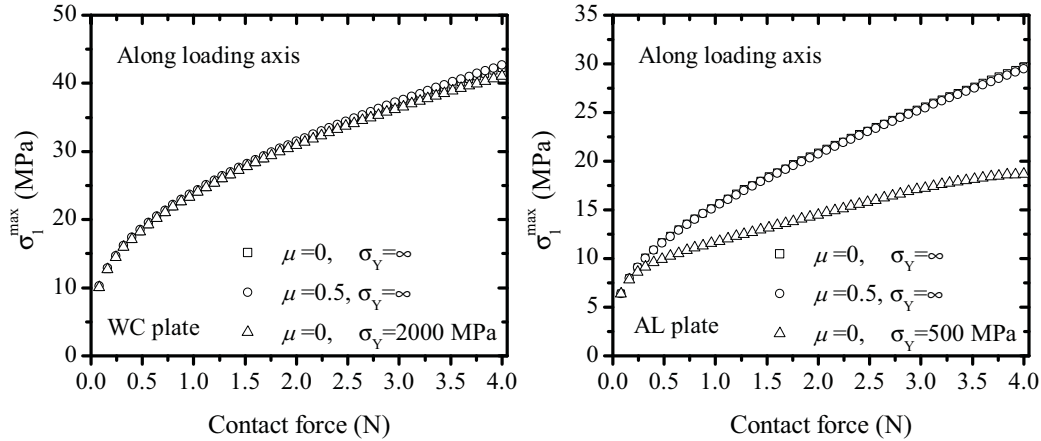
Figure 4.11: The influence of friction and plate plasticity on the maximum tensile stress inside the pebble.

The failure of ceramic pebbles starts when any pre-existing flaw evolves *unstably*. Whether the evolution of a flaw is stable or unstable essentially depends on the stresses near the flaw. The maximum tensile stress, either σ_{vmax} inside the pebble or σ_{smax} on pebble surface, has been considered in the above sections. For the uniaxial loading on a sphere (see Fig. 3.4), Fig. 4.11 shows the influence of friction and plasticity of plates on the maximum tensile stress σ_1^{max} along the loading axis, and Fig. 4.12 shows their influence on σ_1^{max} on the surface. As mentioned in previous section, σ_1^{max} along the loading axis is also the maximum tensile stress inside the sphere. A perfect plasticity model is used in FEM simulations. The Mises yield stresses for AL and WC plates are 500 MPa and 2000 MPa, respectively. The mesh size along the loading axis and on surface is $0.25\ \mu$m. As for the maximum tensile stress σ_1 along the loading axis, friction has little influence for both plates. Accordingly, the failure model in Section 4.2.1 will be independent of friction. On the other hand, the potential plasticity of AL plates decreases the stress to a great extent. This conforms to the qualitative analysis in Section 4.2.1. According to Fig. 4.11, it is expected that the difference between $\sigma_{\mathrm{vmax}}^{\mathrm{AL}}$ and $\sigma_{\mathrm{vmax}}^{\mathrm{WC}}$ will be much larger than 8% when plasticity of plates is considered, which makes the model inapplicable.

As for the maximum tensile stress σ_1 on surface, it is very sensitive to the friction for both plates when the friction coefficient is small, e.g., $\mu < 0.5$ for WC plates and $\mu < 0.1$ for AL
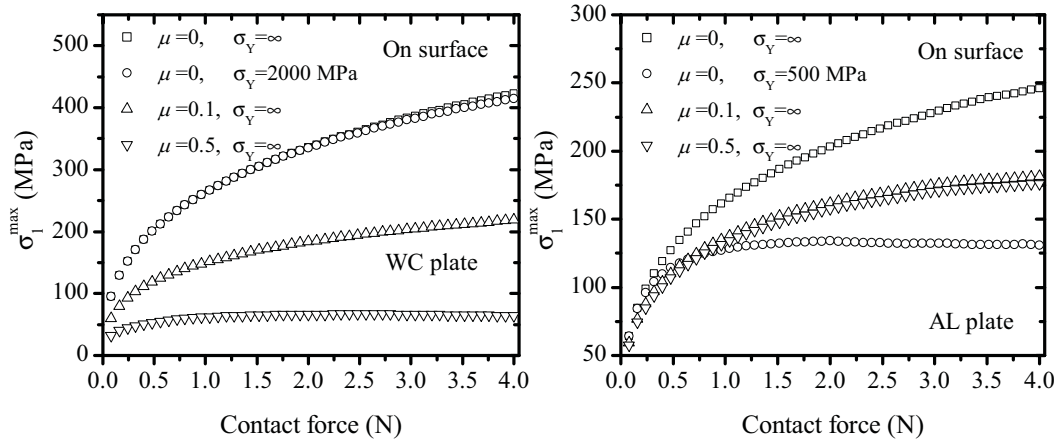
Figure 4.12: The influence of friction and plate plasticity on the maximum tensile stress on pebble surface.

plates. There seems to be a critical friction coefficient above which the stress changes a little for the same contact force. Apparently the critical value for WC plates is bigger than that for AL plates. The plasticity of AL plates decreases the stress drastically.

The qualitative analysis of models in Section 4.2.2 shows that the agreement between predictions and corresponding experimental results will be worse if the potential plasticity of plates is considered. Friction is not taken into account in the failure models in Sections 4.2.2, 4.2.3, 4.2.4, and 4.2.5. The presence of friction is reducing the stresses on surface as well as the presence of plasticity. Thus, it is expected that the agreement between the predictions from these models and the experimental results will also become worse. Consequently, these models would be not applicable yet even if the friction between plates and pebbles is known.

Many investigations have been performed to study the influence of friction on the failure of brittle materials. For example, the failure of a glass plate indented by a spherical indenter has been widely investigated (Fig. 4.13). The influence of plate surface roughness has been studied as well since the roughness will change the friction coefficient and pre-existing flaws at the same time. The conclusion from the tremendous experiments and theory analyses for indentation will help understanding the underlying failure mechanism of pebbles in an analogous manner.

Some spherical indentation tests have been carried out to investigate the friction influence. Argon et al. (1960) investigated the influence of friction by conducting comparative tests with lubricated and non-lubricated indenters with a size of 4.5 mm. No significant difference in failure load was observed. Johnson et al. (1973) performed spherical indentation tests with glass indenter and steel indenter, respectively. The radii of these indenters were selected by calculation so that they would give rise to the same stresses and the same contact area subjected to the same load on a friction-free surface. The difference in failure load should stem from the different friction in interface. They concluded that the influence of friction was significant according to their

experimental results. An abraded glass plate was crushed by harden steel balls by Fischer-Cripps and Collins (1994). Comparison of the failure load was made for lubricated and non-lubricated plate surface. There was little difference for indenter radius bigger than 5 mm while the difference became large for small indenter radius. For the latter case, the failure load for the lubricated plate surface is much smaller than that for the non-lubricated.

The influence of surface roughness was studied by Johnson et al. (1973) as well. The failure load was found to be independent of the plate surface roughness, i.e., the same for an as-received surface and abraded surface. In other words, the failure load was independent of the initial surface flaws. This phenomenon is found by many other experiments, e.g., Fischer-Cripps and Collins (1994); Langitan and Lawn (1969). Meanwhile, the significant influence of surface roughness on the failure load has been found in some indentation tests as well. The failure loads for as-received, 4 minutes etching and 7 minutes etching glass plates, respectively, were greatly different for indenter radius ranging from 1.59 to 31.75 mm (Hamilton and Rawson, 1970). Similarly, Tillett (1956) found that the failure load was the same for both scratched and unscratched glass plate surface when the indenter radius was less than 25.4 mm. However, when the indenter radius increased above 25.4 mm, the failure load became then sensitive to surface roughness.

It can be concluded that the failure of glass plate sometimes depends on friction and surface roughness. On the other hand, the failure is sometimes independent of them. Accordingly, any probabilistic models based on stress and flaw distribution analysis will apparently fail to describe the failure behavior in the cases where failure is independent of friction or surface roughness since the calculated stresses would depend on the friction condition. For example, a probabilistic model based on stresses from the Hüber-Hertz solution was proposed to characterize the failure load distribution (Fischer-Cripps, 1997; Fischer-Cripps and Collins, 1994). The only variable in the model was the maximum tensile stress on the plate surface. An empirical parameter was introduced to account for the friction influence, which should depend on the friction of contact. However, they found in their experiments that the friction had no influence on the failure load (Fischer-Cripps and Collins, 1994), implying that the empirical parameter in their model should be a constant instead of a function of the friction coefficient. The contradiction between the theory and the experiments manifests the invalidity of the model.

There are some theories accounting for the independence of friction and surface roughness on the failure load. Many theories aim to explain the well known phenomenon, namely the so-called Auerbach range. The Auerbach range states that the failure load of plates is proportional to the indenter radius, i.e., $F_c \propto R$, when it is small as shown in Fig. 4.14. Besides, the failure load in the Auerbach range is independent of the surface roughness (Langitan and Lawn, 1969; Tillett, 1956). When the indenter radius is big the failure load is almost proportional to the square of the radius, i.e., $F_c \propto R^2$, which indicates that the plate fails when the maximum tensile stress on surface achieves a critical stress according to Eq. (4.3).
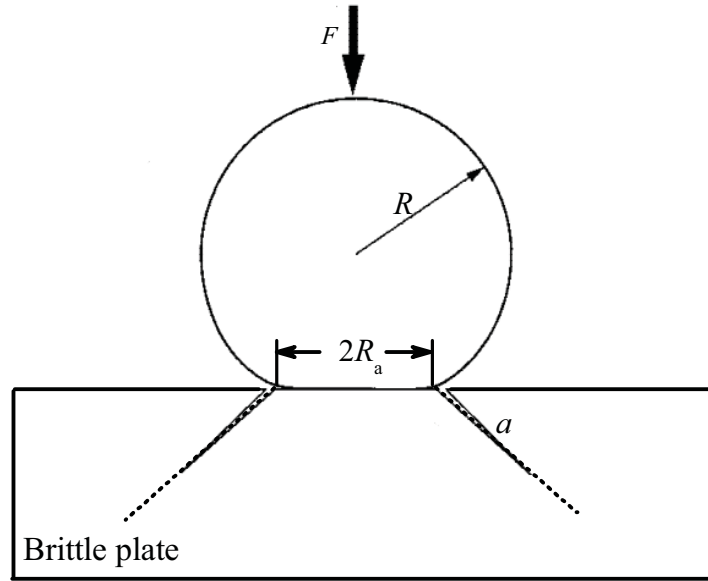
Figure 4.13: Spherical indentation on a brittle plate. The dash line indicates the trajectory of the minimum principal stress σ_3.
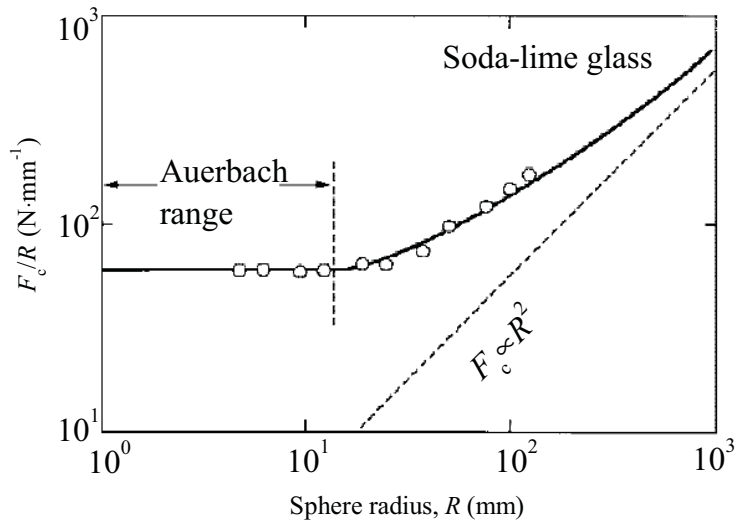
Figure 4.14: Plot of F_c/R vs R for polished soda-lime glass. Plots from Ref. Lawn (1998).

The independence of pre-existing flaw size is successfully explained using Griffith energy concept by Frank and Lawn (1967); Lawn and Wilshaw (1975). The following assumptions are used in their analyses. A brittle plate with a single-valued fracture toughness K_{Ic} is considered. Failure starts from flaws on the plate surface at the contact circle where the tensile stresses are concentrated; the initial flaws, and subsequent evolution, lie along the minimum principal stress σ_3 trajectories in Fig. 4.13. The stress intensity factor K_I is calculated with the stress σ_1 from the Hüber-Hertz solution along this direction starting from $\rho_1 = 1$. It is assumed that the flaw can evolve when $K_I > K_{Ic}$. The calculated K_I with respect to flaw size is plotted in Fig. 4.15.
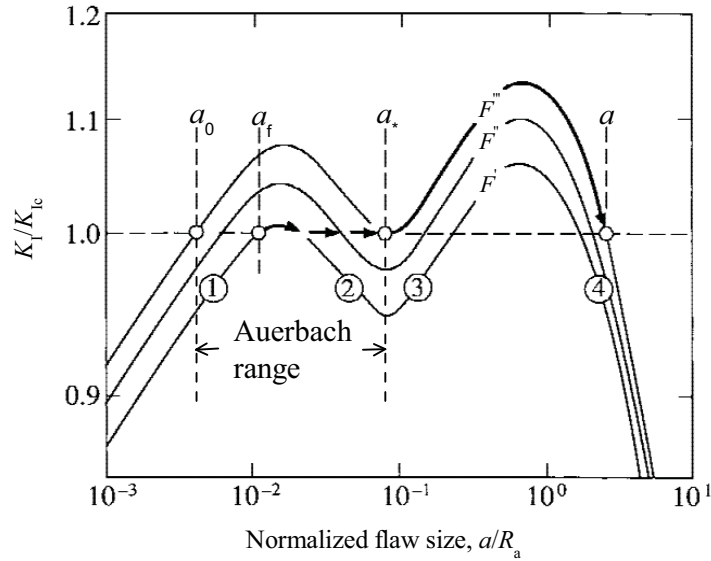
Figure 4.15: Normalized stress intensity factor for $\rho_1 = 1$ and $\nu = 0.3$. Arrows indicate evolution from surface flaw to full cone crack for a load from F' to F'''. Plots from Ref. Lawn (1998).

The decrease of K_I in branch 2 is due to the high stress gradient (from the Hüber-Hertz solution) along the flaw. When the load increases from F' to F''', a_f evolves stably to a_* along the dash line $K/K_{Ic} = 1$. When $F > F'''$, unstable flaw evolution leads to catastrophic failure. It is concluded that pre-existing flaws a_f with a size between a_0 and a_* correspond to the same failure load, i.e., flaw size independence. Moreover, as indicated by Lawn (1998), catastrophic failure is spontaneous from branch 1 to 4 for very small flaws in the range $a_f \ll a_0$ or for large spheres, which corresponds to the asymptotic relation $F_c \propto R^2$ in Fig. 4.14.

The theoretical analysis reveals that the flaw size independence in the Auerbach range is essentially due to the high stress gradient, such that there are stable flaw evolution (branch 2 and 4 in Fig. 4.15). It is expected that these stable branches will also exist when friction is present. Consequently, the failure load can be independent of friction in certain range of a/R_a. Also in the presence of friction, the pre-existing flaw size distribution can be modified in the Auerbach range by stress while the brittle plate will not fail. In other words, the stress distribution and flaw size distribution are not independent events. On the other hand, it is a basic assumption that stress and flaw size in a component are independent before failure occurs in many probabilistic failure theories. It is assumed that catastrophic failure occurs when any critical flaw starts to evolve. Consequently, the failure load of plates will be drastically underestimated for flaws in a high stress gradient field. For example, smaller a_f between a_0 and a_* in Fig. 4.15 would correspond to smaller failure load. In fact, the evolvement of flaw is stable and the plate can sustain more load before catastrophic failure. In such a case, the predicted failure probability for a given load will be much higher than the one from experiments.

A critical issue is subsequently raised, that is, how to quantitatively identify the Auerbach range. Hamilton and Rawson (1970) found that the upper limit of the Auerbach range depends on the strength of the glass plate. For a given brittle plate, the upper limit could be found through checking the surface roughness influence with increasing indenter radius. It is thus important to know whether the failure of brittle components in experiments lies in the Auerbach range or outside.

It can be concluded that the failure load probability of a brittle plate can be characterized by two independent events, namely stress and flaw distributions, only for sphere size far away from the Auerbach range where it holds $F_c \propto R^2$ in Fig. 4.14. In such cases, the friction and surface roughness plays an important role. The probabilistic model based on maximum tensile stress on surface should be applicable, e.g., Jelagin and Larsson (2008). On the other hand, energy criterion is preferred to describe the failure in the Auerbach range (e.g., Roesler (1956a,b)). It is assumed that a critical energy gives rise to the catastrophic failure of plates. Langitan and Lawn (1969) have elaborated the failure mechanism. Anyhow, it is hard to conclude whether stress or energy criterion is suitable for characterizing the failure load if there is only one failure test. There should be at least two comparative tests to find which one is applicable as we did in this chapter. Care should be taken that the comparative tests should lie in the Auerbach range or outside at the same time.

Until now, the failure analysis is restricted to a brittle plate indented by spherical indenters. Analogically, the conclusion can be applied to the failure of spherical pebbles in our case. The key point is whether there also exists an "Auerbach range", in other words, if there are some cases that the failure of brittle spheres are independent of friction or surface roughness. There are few investigations concerning this issue. The influence of surface roughness of lead-glass and sapphire spheres on their failure load has been investigated by Shipway and Hutchings (1993). Many different materials were used as plates. For glass spheres with a size of 0.7 mm, abrasion of their surface decreased the failure load drastically for both AL alloy and SiC plates. On the other hand, for sapphire spheres with a size of 0.794 mm, abrasion of their surface has no effect for the SiC plate, which is a chief characteristic of the Auerbach range. Therefore, a similar Auerbach range does exist for the failure of spheres. However, we cannot say whether the failure of pebbles belongs to this range. As a result, various models based on stress and energy criterion, respectively, have been tried in this chapter. Finally, the applicability of the energy model is validated by the crush load distributions in Chapter 2, which implies the inapplicability of probabilistic models in terms of stress. Care should be taken that the energy model has to be used critically. It might fail for other ceramic pebbles, such as Li_2TiO_3.

4.4.2 Weibull distribution

The Weibull distribution is widely adopted in probabilistic models to characterize the strength of brittle materials. The parameters, m, σ_{u} and σ_0 in the distribution will be discussed in this section. The Weibull modulus m is commonly regarded as a material constant characterizing the flaw or strength distribution. Anyhow, this is questioned by some researchers. It is concluded that the Weibull modulus depends on stress field and geometry of specimen from their experiments (Afferrante et al., 2006; Danzer et al., 2007; Fett and Munz, 2002; Fett et al., 2003; Lamon and Evans, 1983). This dependence should be due to the high stress gradient as explained in the above section. Two parameter Weibull distribution, i.e., $\sigma_{\mathrm{u}} = 0$, was used to fit their experiments. It is noted that using two or three Weibull parameters in the fitting function results in different Weibull parameters. Lu et al. (2002b) investigated the influence of σ_{u} on the estimation of Weibull statistics. Numerical simulation showed that two parameter Weibull distribution ($\sigma_{\mathrm{u}} = 0$) was preferred, provided that the sample data were limited in number and σ_{u} in the three parameter Weibull distribution was not too large. Moreover, Bergman (1984) investigated the influence of probability estimators, i.e, the expression of P_{s} for experimental data. It is concluded that $P_{\mathrm{s}} = i/(N + 1)$ (explained in Chapter 2) is a preferred choice from an engineering point of view. Anyhow, it is expected that different probability estimator will lead to different Weibull parameters although the difference could be small. Finally, failure starting from surface or volume results in different Weibull parameters. Hence, it is useful to know where failure starts and use the corresponding parameters.

As for the Weibull approach, the parameters have no explicit physical basis. Besides, the parameters as well as the variables do not have to be stress (Weibull, 1951). It could be any other variable, e.g., force or energy. Thus, the proposed energy distribution can be regarded as a kind of Weibull approach. As Weibull (1951) has concluded that this approach is not always valid and the applicability should be tested empirically. It is worth following this concept until an applicable model with explicit physical basis is established,

4.5 Summary

In this chapter, various probabilistic models are used to characterize the plate influence on the failure load. The comparative crush load distributions are used to validate these models. Finally, a Weibull distribution model in terms of absorbed energy is validated. The merit of this model is that the influence of coordination number of contact loads has been taken into account. The underlying reason of the applicability is also discussed. Subsequently, the strength distribution of pebbles in pebble beds is derived with the crush load distribution from FML. The strength as a material constant will be imported into DEM.

Chapter 5
Choice of parameters in DEM simulations

In the previous chapters, the pebble-pebble contact strength has been derived. Subsequently, the energy strength will be used in DEM to study the influence of pebble failure on the macroscopic behavior of pebble beds. We will make use of the DEM code developed at KIT (Gan, 2008; Gan and Kamlah, 2010). There are several input parameters in this code. Some of them will be discussed in this chapter.

5.1 Shear stiffness

The tangential contact force between elastic spheres can be described by a non-smooth relation when sliding starts (Bicanic, 2004)

$$F_{\text{T}} = \mu F_{\text{N}} \quad \text{for} \quad \Delta x_{\text{T}}^{'} \neq 0 \,, \tag{5.1}$$

where F_{T} and F_{N} denote the tangential and normal contact forces, respectively. μ is the friction coefficient. The difference between the coefficients for static and dynamic friction is ignored here. F_{T} has a direction opposite to the sliding velocity $\Delta x_{\text{T}}^{'}$ between spheres. Figure 5.1 illustrates the non-smooth relation.
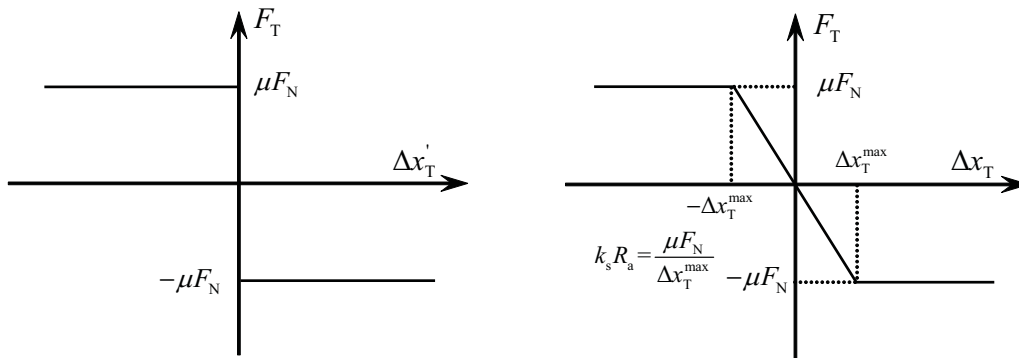
Figure 5.1: Non-smooth (left) and regularized (right) treatment of tangential contact force F_{T}. $\Delta x_{\text{T}}^{'}$ is the sliding velocity. Δx_{T} is the relative displacement.

However, Eq. (5.1) cannot be implemented into DEM because of the singularity of F_{T} at $\Delta x_{\text{T}}^{'} = 0$. The singularity can be removed by a regularized treatment (Bicanic, 2004; Brendel

and Dippel, 1998) as shown in Fig. 5.1, where Δx_T is the relative displacement. As a result of the regularized treatment, the friction force is proportional to Δx_T when it lies in the range $-\Delta x_\mathrm{T}^{\max} \leqslant \Delta x_\mathrm{T} \leqslant \Delta x_\mathrm{T}^{\max}$. This treatment has been implemented into the DEM code. The tangential contact force F_T reads

$$F_\mathrm{T} = -\frac{\Delta x_\mathrm{T}'}{|\Delta x_\mathrm{T}'|} \min\left(\mu F_\mathrm{N}, k_\mathrm{s} R_\mathrm{a} |\Delta x_\mathrm{T}|\right) , \tag{5.2}$$

where k_s is defined as the shear stiffness in this thesis which has a pressure unit. It is different from the notation of k_s used by Bicanic (2004); Gan (2008); Gan and Kamlah (2010). R_a is the radius of the contact circle as used in previous chapters, which depends on F_N. Note that k_s and μ are two input parameters in the code. They are expected to play a substantial role in DEM simulations. k_s is set to 5000 Pa and μ is set to 0.1 in the analyses of Gan (2008); Gan and Kamlah (2010).
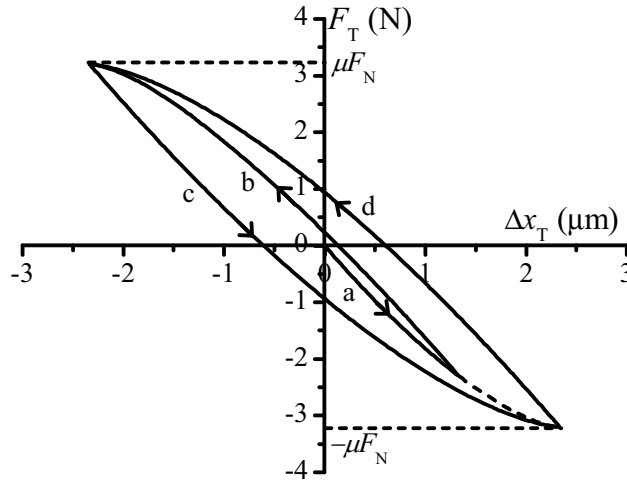
Figure 5.2: Force-displacement relation for two equal spheres in contact. Before sliding starts ($F_\mathrm{T} = \mu F_\mathrm{N}$), the displacement changes to the opposite direction (from branch *a* to *b*).

For the elastic contact between spheres, Mindlin and Deresiewicz (1953) derived the analytical solution for the force-displacement relation of tangential contact. The tangential force calculated from the solution depends not only on the initial state of loading but also on loading history, i.e., the maximum tangential force $|F_\mathrm{T}|$ and the instantaneous relative rates of change of the normal and tangential forces. In this solution, it is assumed that the size of contact circle is independent of the tangential contact force, and slip at a point in the contact circle starts when $\sigma_\mathrm{T} = \mu \sigma_\mathrm{N}$ where σ_N and σ_T are the normal and tangential stresses at the point, and μ is the friction coefficient between spheres. Sliding occurs when all points in the contact circle S start to slip, corresponding the maximum tangential contact force $F_\mathrm{T} = \mu F_\mathrm{N}$ since $F_\mathrm{N} = \int \sigma_\mathrm{N} dS$ and $F_\mathrm{T} = \int \sigma_\mathrm{T} dS = \mu \int \sigma_\mathrm{N} dS$ hold. This solution has been verified by FEM simulations (Vu-Quoc and Zhang, 1999; Vu-Quoc et al., 2001).
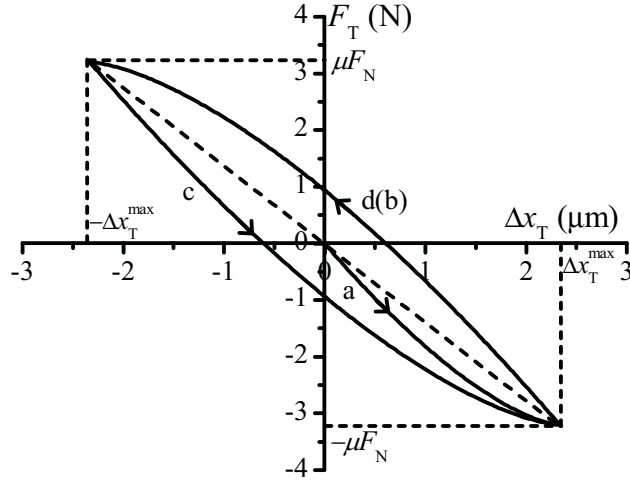
Figure 5.3: Force-displacement relation for two spherical pebbles in contact. The first displacement will then lead to sliding (branch *a*).

Figure 5.2 shows the force-displacement loop calculated from the analytical solution. The loop is calculated for a contact between two elastic spheres. The spheres have a radius of $R = 0.25$ mm with Young's modulus of 90 GPa and Poisson's ratio of 0.25, which are the same as that for Li_4SiO_4 pebbles. The normal contact force is $F_N = 8$ N. The friction coefficient between spheres is set to $\mu = 0.4$. At the beginning of tangential displacement, $\Delta x_T = 0$ and $F_T = 0$ holds. A positive tangential displacement $\Delta x_T > 0$ gives rise to a negative F_T (branch *a*). Before sliding starts, i.e., $|F_T| < \mu F_N$, the displacement can change to the opposite direction, e.g., branch *b*. If the displacement in branch *a* does not change direction before sliding starts, the force-displacement relation continues along the dashed line. Later the pair of $(\Delta x_T, F_T)$ will lie either in branch *c* or *d* since the maximum $|F_T|$ in the load history is a constant μF_N. Figure 5.3 shows the corresponding load loop.

If we set the maximum allowable displacement Δx_T^{max} in Figs. 5.1 and 5.3 equal, the shear stiffness k_s then reads as

$$k_s = \frac{\mu F_N}{\Delta x_T^{max} R_a} \cdot \qquad (5.3)$$

Δx_T^{max} can be derived from the analytical solution (Mindlin and Deresiewicz, 1953) as

$$\Delta x_T^{max} = \frac{3\mu F_N}{16 R_a G^*} , \qquad (5.4)$$

where G^* is the equivalent shear modulus, i.e.,

$$G^* = \left(\frac{2 - \nu_1}{G_1} + \frac{2 - \nu_2}{G_2} \right)^{-1} . \qquad (5.5)$$

G_1 and G_2 are shear moduli for each sphere material, respectively, and ν_1 and ν_2 are the corresponding Poisson's ratios. For the pebble-pebble contact under consideration, it holds $G_1 = G_2$

67

and $\nu_1 = \nu_2$. Substitution of Eq. (5.4) into Eq. (5.3) yields

$$k_{\mathrm{s}} = \frac{16}{3}G^* \, . \tag{5.6}$$
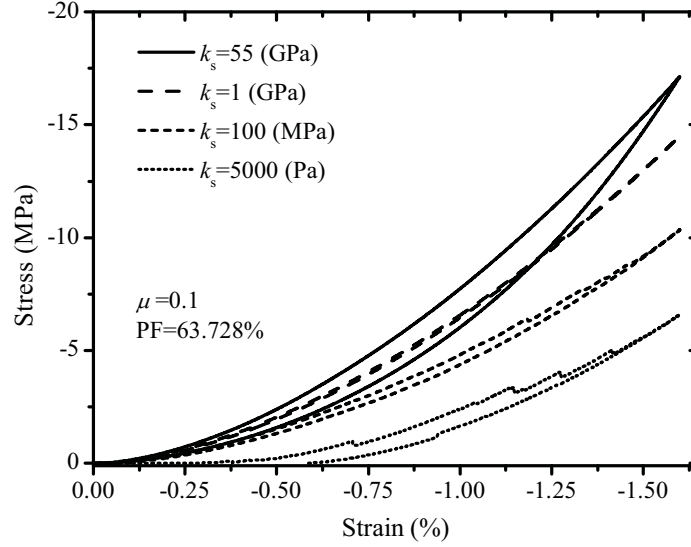
Figure 5.4: The influence of shear stiffness on the macroscopic stress-strain relation of mono-sized spheres in uniaxial compression tests.

The derived k_{s} is independent of F_{N} and F_{T}. It has the same expression as that derived from inclined impact of a particle on a flat wall by Di Renzo and Di Maio (2005). Besides, the slope of branch a at the beginning of the tangential displacement is $8G^*$ which is the shear stiffness proposed by Mindlin (1949). The real stiffness should lie between $16/3G^*$ and $8G^*$ depending on the load history. In this thesis, Eq. (5.6) will be used for DEM simulations. Li$_4$SiO$_4$ pebbles correspond to a shear stiffness of $k_{\mathrm{s}} = 55$ GPa. It can be seen that the $k_{\mathrm{s}} = 5000$ Pa used in the analyses of Gan (2008); Gan and Kamlah (2010) is too small.

For the same R_{a}, namely the same F_{N}, and Δx_{T}, a larger k_{s} leads to an increased $|F_{\mathrm{T}}|$ according to Eq. (5.2) when sliding does not occur. Consequently, spheres having a big tangential contact force in the assembly will be more difficult to move or rotate. The sphere system will behave stiffer. For the same macroscopic strain, it is expected that the macroscopic stress for $k_{\mathrm{s}} = 55$ GPa will be much higher than for $k_{\mathrm{s}} = 5000$ Pa.

Figure 5.4 shows the influence of shear stiffness on the macroscopic stress-strain relation of mono-sized spheres. Spheres are assigned the material parameters of Li$_4$SiO$_4$ pebbles. A failure criterion is not implemented. There are 5000 mono-sized spheres in a cubic box with periodic boundary conditions. The sphere size will not influence the stress-strain relation, which will be discussed later. The box is compressed uniaixally by strain loading, i.e., $\varepsilon_z < 0$ and $\varepsilon_x = \varepsilon_y = 0$. $\varepsilon_x, \varepsilon_y$ and ε_z are macroscopic stains along x, y and z directions, respectively. Negative value of strain and stress indicates compression. The stress-strain curves along the loading direction are
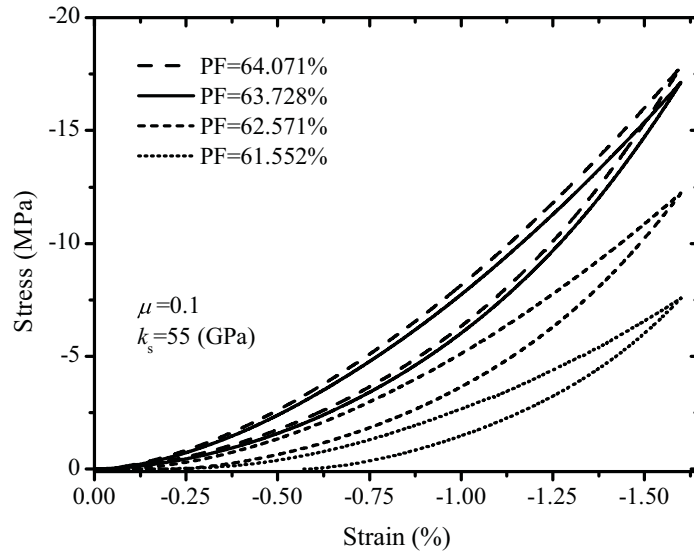
Figure 5.5: The influence of PF on the macroscopic stress-strain relation of mono-sized spheres in uniaxial compression tests.
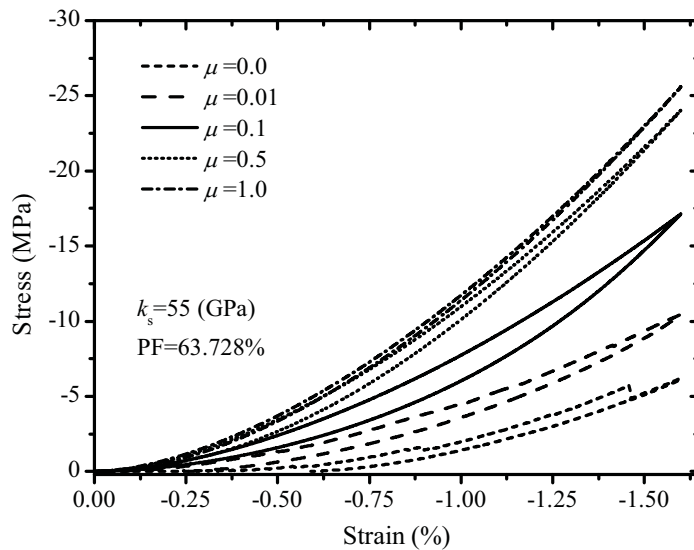
Figure 5.6: The influence of friction coefficient on the macroscopic stress-strain relation of mono-sized spheres in uniaxial compression tests.

plotted, namely σ_z versus ε_z. The friction coefficient between spheres is set to 0.1. The sphere assembly becomes stiffer when k_s increases as expected. The stresses for $k_s = 55$ GPa are about two times larger than that for $k_s = 5000$ Pa for the same strain. It is also found that there is no macroscopic plasticity after unloading for larger k_s. Thus, it is essential to use the derived $k_s = 55$ GPa for pebbles instead of $k_s = 5000$ Pa.

Figure 5.5 shows the influence of packing factor for the same $k_s = 55$ GPa and $\mu = 0.1$. Compared to the results for $k_s = 5000$ Pa and $\mu = 0.1$ (Gan, 2008; Gan and Kamlah, 2010), the

sensitivity of stress-strain relation to PF has decreased. Table 5.1 shows the compressive stress σ_z along the loading direction at a strain of $\varepsilon_z = -1.25\%$. For the result in Gan's thesis (Gan, 2008), the macroscopic stress reported for a PF of 63.8% is almost 50% of the system with a PF of 64.0%. However, with the modified shear stiffness ($k_s = 55$ GPa) the difference is only 2%.

Table 5.1: The compressive macroscopic stress σ_z at $\varepsilon_z = -1.25\%$ from DEM simulations of mono-sized spheres in uniaxial compression tests, i.e., $\varepsilon_x = \varepsilon_y = 0$. Both results are from the loading branch.

	PF$\approx 64.0\%$	PF$\approx 63.8\%$
$k_s = 5000$ Pa *	≈ 6.5 MPa	≈ 3.5 MPa
$k_s = 55$ GPa	11.8 MPa	11.6 MPa

* Data from Ref. Gan (2008).

Figure 5.6 shows the effect of the friction coefficient on the stress-strain relation from DEM simulations of uniaxial compression tests for $k_s = 55$ GPa. For the same ε_z, a low friction coefficient corresponds to a low macroscopic stress, which conforms to the finding by Procopio and Zavaliangos (2005). The variation of small friction coefficient like $\mu < 0.5$ has a strong impact on the stress-strain relation, e.g., the case for μ changing from 0 to 0.01. On the other hand, when μ is large enough, the response becomes insensitive to μ, e.g., the case for μ changing from 0.5 to 1. Thus, it is important to known the friction coefficient between pebbles to avoid the large errors in the range of small friction coefficient.

5.2 Influence of sphere size

The initial configuration of mono-sized spheres is generated using the algorithm proposed by Jodrey and Tory (1985) in a unit space like $l \times l \times l$ cubic box. The configuration includes the relative radius R_r, the relative center position of each sphere and the corresponding PF. They are related to the dimension of the box except of PF. The relation between PF and l, R_r and the number of spheres N is PF$= 4N\pi R_r^3/(3l^3)$. For the same PF and N, R_r/l is a constant, and hence spheres can be assinged a true size by scaling R_r and l at the same time. For example, for Li$_4$SiO$_4$ pebbles with a size of $R = 0.25$ mm, the position for each sphere and the dimension of the unit box have to be resized by multiplying by $l_r = R/R_r$ such that the topology and PF of spheres stays the same as the initial configuration. Therefore, DEM simulation can be performed for different sphere size for the same initial configuration. The size influence on the macroscopic stress-strain relation and internal contact force for the same initial configuration will be discussed.

We will compare two cases for mono-sized spheres for the same initial configuration. Parameters and values with a subscript 1, such as l_1 and R_1, indicate the first case and those with a

subscript 2, such as l_2 and R_2 indicate the second case, respectively. The ratio of length parameters for case 2 to that for case 1 is l_r, e.g., $l_2/l_1 = l_r$ and $R_2/R_1 = l_r$.

The strategy for uniaxial strain loading is that for a small strain ε_z all spheres are initially moved by

$$\Delta x_z = \varepsilon_z x_z \,, \tag{5.7}$$

where x_z is the coordinate of sphere center along the loading direction. After that the spheres are moved according to the Newton's second law until the system reaches an equilibrium state. The gravity of spheres is not taken into account.

Right after the spheres have been moved *initially* according to Eq. (5.7), the topology should be the same for both cases. For any corresponding contact pair in both cases, the relation

$$\frac{R_2^*}{R_1^*} = \frac{\delta_2}{\delta_1} = \frac{R_{a2}}{R_{a1}} = l_r \tag{5.8}$$

holds. R^* is the radius of relative curvature and R_a is the radius of the contact circle. δ is the overlapping between two spheres. The normal contact force

$$F_N = -\frac{4}{3} E^* \sqrt{R^*} \delta^{3/2} \tag{5.9}$$

is calculated from Hertz theory. Here E^* is the equivalent Young's modulus. Substitution of Eq. (5.8) into (5.9) yields

$$\frac{F_{N2}}{F_{N1}} = l_r^2 \,. \tag{5.10}$$

Δx_T in Eq. (5.2) denotes the relative tangential displacement. The ratio of its length for case 2 to that for case 1 should be also l_r, i.e.,

$$\frac{\Delta x_{T2}}{\Delta x_{T1}} = l_r \,. \tag{5.11}$$

Substitution of Eqs. (5.8), (5.10) and (5.11) into (5.2) yields

$$\frac{F_{T2}}{F_{T1}} = l_r^2 \,. \tag{5.12}$$

That is, when all spheres have been moved *initially* by Δx_z, the contact force $F = \sqrt{F_N^2 + F_T^2}$ for any corresponding contact pair in both cases will satisfy $F_2/F_1 = l_r^2$ according to Eqs. (5.10) and (5.12). If P_{c1} and P_{c2} denote the contact force distributions in the sphere assembly, it will hold

$$P_{c1}(F_1) = P_{c2}(F_2) \,. \tag{5.13}$$

Let us set the relation of the density used in case 1 and case 2

$$\rho_1 = l_r^2 \rho_2 \,. \tag{5.14}$$

As a result, the acceleration a for each sphere when they have been moved *initially* satisfies

$$\frac{a_2}{a_1} = l_{\mathrm{r}} \tag{5.15}$$

using Eqs. (5.10), (5.12) and (5.14).

When the same time step is used in both cases, the displacement of every sphere at each time step will satisfy the relation $x_2/x_1 = l_{\mathrm{r}}$ and is along the same direction. Accordingly, the topology for both cases will be the same. There are two input parameters for the convergence control, i.e., a maximum allowable unbalanced force δf_{m} and a maximum allowable average kinetic energy $\mathcal{K}_{\mathrm{m}}$. It is assumed that the equilibrium state is reached when $\delta f \leqslant \delta f_{\mathrm{m}}$ and $\mathcal{K} \leqslant \mathcal{K}_{\mathrm{m}}$ are satisfied at the same time. δf and $\mathcal{K}$ are the average contact force and kinetic energy, respectively, calculated after each time step. When the parameters used in both cases satisfy

$$\frac{\delta f_{\mathrm{m2}}}{\delta f_{\mathrm{m1}}} = l_{\mathrm{r}}^2, \quad \frac{\mathcal{K}_{\mathrm{m2}}}{\mathcal{K}_{\mathrm{m1}}} = l_{\mathrm{r}}^3 \,, \tag{5.16}$$

it is expected that the topology at the corresponding equilibrium state will be still the same. This means Eqs. (5.10), (5.12) and (5.13) will also hold at the final equilibrium state.

The average macroscopic stress reads as (Gan, 2008; Gan and Kamlah, 2010)

$$\bar{\sigma}_{ij} = \frac{1}{V} \oint_A \tilde{F}_j x_i dA \,, \tag{5.17}$$

where V is the volume of the representative volume element (RVE) containing all spheres, A indicates the surface of volume V. $\tilde{F}$ indicates the external forces distribution on the surface A of the considered body. The volume relation is straightforward, i.e.,

$$\frac{V_2}{V_1} = l_{\mathrm{r}}^3 \,. \tag{5.18}$$

Substitution of Eq. (5.10), (5.12) and (5.18) into (5.17) yields the average stress tensor $\bar{\sigma}$ relation

$$\bar{\sigma}_1 = \bar{\sigma}_2 \,. \tag{5.19}$$

Eq. (5.19) indicates that $\bar{\sigma}$ is independent of sphere size.

The mass of sphere does not influence the contact force between spheres according to Eqs. (5.2) and (5.9). Nevertheless, the mass will change the acceleration of every sphere, and hence affect the convergence rate. For the RVE containing a large number of spheres, the simulation results should be the same for different time steps, provided that convergence can be reached with δf_{m} and $\mathcal{K}_{\mathrm{m}}$ which are small enough in both cases. The same result means the same statistic information, such as the contact force distributions P_c, rather than the topology of spheres in the final equilibrium state. The independence of mass and time steps has been confirmed by DEM simulations for $N = 5000$ mono-sized spheres with a periodic boundary condition. Furthermore, although Eq. (5.13) and (5.19) are derived with a specific mass relation (i.e., Eq. (5.14)) and

the same time steps, they are found to be valid, as expected, in DEM simulations for the same initial configuration but different size of spheres. On the other hand, the results also indicate that $N = 5000$ is a large enough number to obtain a turely representative volume element (Kanit et al., 2003).

5.3 Influence of sphere material

The influence of sphere material can be obtained by performing a similar analysis as in the above section. We will compare two cases for the same initial configuration including size, position and PF. The difference between them is the Young's modulus of sphere material, i.e., E_1 for case 1 is not equal to E_2 for case 2. The relation

$$E^* = \frac{E}{2(1 - \nu)}, \quad G^* = \frac{E}{4(1 + \nu)(2 - \nu)}$$

(5.20)

holds for the same sphere materials in each case. For the same Poisson's ratio $\nu_1 = \nu_2 = \nu$, E^* and G^* will be proportional to the Young's modulus. As a result, the derived shear stiffness k_s in Eq. (5.3) will be also proportional to the Young's modulus.

When the spheres have been moved *initially*, substitution of Eq. (5.20) into (5.9) and (5.2) yields

$$\frac{F_{N1}}{F_{N2}} = \frac{E_1}{E_2}, \quad \frac{F_{T1}}{F_{T2}} = \frac{E_1}{E_2}$$

(5.21)

for any corresponding contact pair in both cases for the same ν. That is, the contact force is proportional to the Young's modulus of the sphere material.
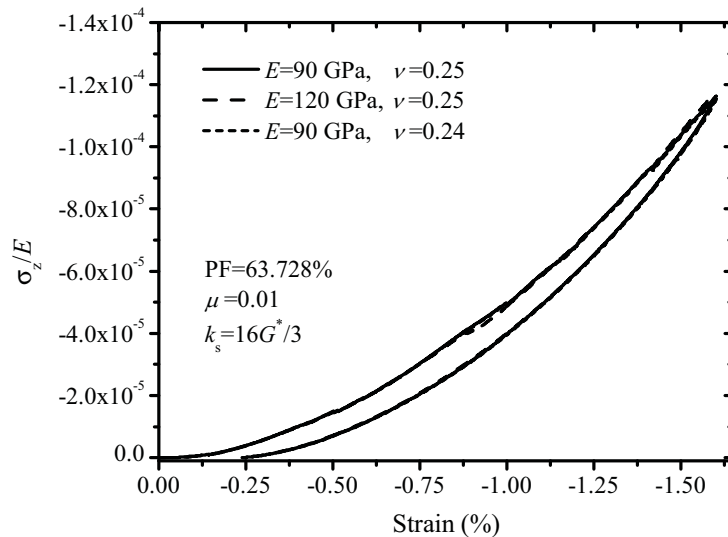
Figure 5.7: Normalized stress-strain relation for different sphere material parameters. DEM simulation for uniaxial compression tests.

As discussed in the above section, appropriate mass and time steps can be selected so that the topology in both cases is alway the same until the equilibrium state is reached. Equation (5.21) is valid in the whole procedure of sphere movement. Accordingly, the average macroscopic stress for both cases in the equilibrium state satisfies

$$\bar{\boldsymbol{\sigma}}_1 = \frac{E_1}{E_2} \bar{\boldsymbol{\sigma}}_2 \qquad (5.22)$$

according to Eq. (5.17). When $F_1/F_2 = E_1/E_2$ holds, the contact force distribution satisfies

$$P_{\text{c1}}(F_1) = P_{\text{c2}}(F_2) \,. \qquad (5.23)$$

Figure 5.7 shows the stress-strain curves along the loading direction for three cases. They correspond to the same initial configuration and the same friction coefficient, $\mu = 0.01$. The spheres in each case have different Young's moduli and Poisson's ratios. The agreement of the curves for the same Poisson's ratio validates Eq. (5.22). The curves for $\nu = 0.25$ and $\nu = 0.24$, which are most frequently used Poisson's ratios for Li_4SiO_4 pebbles, has little difference. Besides, it is found that Eq. (5.23) holds for these cases although their topology in equilibrium state is different. Note that using a big μ will give rise to better agreement between these curves.

The Poisson's ratio of Li_4SiO_4 pebbles, either 0.24 or 0.25, is found in literature, while its Young's modulus varies significantly from 50 to 120 GPa as measured from experiments (Chu et al., 1989; Dienst and Zimmermann, 1988; Johnson et al., 1988; Vollath et al., 1990). When the simulation results for a special Young's modulus are obtained, the results for other Young's moduli for the same initial configuration can be derived with the help of Eqs. (5.22) and (5.23). It is expected that $\nu = 0.25$ or $\nu = 0.24$ hardly has effect on the relation.

5.4 Discussion

The influence of size and material on stress-strain response is studied for mono-sized spheres with a periodic boundary condition subjected to uniaxial strain loading, i.e., Eq. (5.7). However, similar analysis can be applied to a generalized case, that is, multiaixal loading, multi-sized spheres and generalized boundary condition. For example, for the same initial configuration for multi-sized spheres, let the ratio of the size of corresponding spheres in the two cases be denoted by a constant l_r. As for the size influence, Eqs. (5.8) to (5.13) will still be valid when spheres have been initially moved by either uniaxial or multiaxial loading. These relations are also independent of boundary conditions. Consequently, with the specific relation of mass in these cases, i.e., Eq. (5.14), and the same time step, Eqs. (5.13) and (5.19) can also be derived when both cases reach the equilibrium state. As for the material influence, Eq. (5.22) and (5.23) can be derived as well since Eq. (5.21) is independent of the kind of loading, sphere size and boundary conditions.

5.5 Summary

An appropriate shear stiffness in the tangential contact model is identified from an analytical solution. It depends on material parameters of two contact bodies rather than a input parameter as used before. The influence of friction coefficient between spheres is studied with the derived shear stiffness. The friction will play an important role in DEM simulations. Finally, it is shown that the true size of spheres does not influence the macroscopic stress-strain relation and the contact force distribution in the sphere assembly. The relation between macroscopic stresses for different Young's modulus of spheres for the same initial configuration is derived as well.

Chapter 6
Pebble failure

The pebble-pebble contact strength in terms of critical energy is derived in Chapter 4. The distribution of critical energy for pebbles can be imported into DEM. The influence of pebble failure on the macroscopic stress-strain relation can be subsequently investigated. This chapter reports the influence of failure initiation and propagation of pebbles on the macroscopic stress-strain relation for pebble beds. It is assumed that pebbles have a spherical shape with an equal radius of $R = 0.25$ mm, and only elastic deformation of pebbles is taken into account. The material parameters in Table 2.1 will be used in this chapter. A periodic boundary condition is used for each initial configuration of sphere assembly with $N = 5000$ spheres. The proper shear stiffness k_s in the tangential contact model, i.e., Eq. (5.6), will be used, and the friction coefficient between pebbles is set to 0.1 as adopted by Gan (2008). The gravity of pebbles is not taken into account.

6.1   Failure initiation

A pebble fails when it absorbs more energy (strain energy) than its critical value. In pebble beds the energy absorbed by each pebble is given by

$$W_\mathrm{p} = \sum_{i=1}^{N_\mathrm{c}} c F_i^{\frac{5}{3}} \, , \tag{6.1}$$

where N_c is the coordination number of the pebble, F_i is the force of i-th contact ($i = 1, 2, \cdots, N_\mathrm{c}$), and c is a constant derived from Hertz theory given by

$$c = \frac{1}{5} \left(\frac{9}{16R^*} \right)^{\frac{1}{3}} \frac{1}{E^{*\frac{2}{3}}} \, . \tag{6.2}$$

Here, R^* is the relative radius of curvature, and E^* is the equivalent Young's modulus. For a contact between mono-sized spherical pebbles, $R^* = R/2$ and $E^* = E/(2(1 - \nu^2))$, where R, E and ν are the radius, Young's modulus and Poisson's ratio of pebbles, respectively. Failure initiation can be defined by the number of crushed pebbles N_f. In other words, failure initiation starts when N_f pebbles have failed in pebble beds. The load level in terms of either macroscopic stress or the average contact force F_ave is investigated when failure initiation starts. F_ave is defined as the sum of the normal contact force divided by the number of contact pairs (Gan, 2008).

77

There are basically two methods to study failure initiation. The first one is a numerical method. The number N_f has to be prescribed before simulations. In DEM simulations, when the number of crushed pebbles reaches N_f, the corresponding load level is then exported as the load level for failure initiation. Many simulations for different initial configuration of pebbles are performed to obtain the statistical information of the load level for failure initiation. The second one is a numerical-analytical method. This method is based on the distribution of the strain energy absorbed by non-crushable pebbles and the derived critical energy distribution. They are assumed to be independent events and are not influenced by the failure of a small number of pebbles.

6.1.1 Numerical method

In this method, a critical energy W_c is prescribed to each pebble at the beginning. For any pebble in DEM simulations, it fails when $W_p > W_c$. The distribution of W_c for all pebbles has to satisfy the derived critical energy distribution P_s in Chapter 4, i.e., Eq. (4.25).

Every pebble in simulations has a unique ID number such that we can record the information of the pebble during loading. Monte Carlo method is used to assign each pebble a critical energy. A pair of statistically independent random numbers (W_c, p) is generated in the range of $0 \leqslant W_c \leqslant$
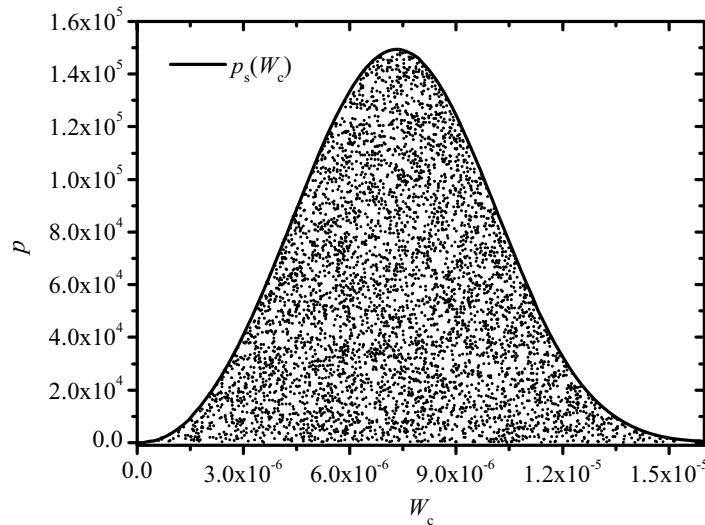
Figure 6.1: Random numbers satisfying $p \leqslant p_s(W_c)$, and p_s is the PDF of the critical energy for pebbles.

0.000016 and $0 \leqslant p \leqslant 160000$. If $p \leqslant p_s(W_c)$ holds, the first pebble (ID=1) is assigned the W_c as its critical energy, where $p_s(W_c)$ is the probability density function (PDF) of the critical energy for pebbles, namely Eq. (4.26). Subsequently, we regenerate another pair of random numbers in the area, the W_c will be assigned to the second pebble (ID=2) if $p \leqslant p_s(W_c)$. This procedure is repeated until every pebble has a prescribed critical energy. Figure 6.1 shows 5000 pairs of (W_c, p) satisfying $p \leqslant p_s(W_c)$ together with $p_s(W_c)$. The distribution of W_c for all pebbles will

satisfy the distribution of the critical energy, i.e., Eq. (4.25), consequently.

The random number W_c should be generated in the range of $0 \leqslant W_c < \infty$, in principle. Anyhow, it is necessary to select a upper limit of W_c in the Monto Carlo method. An appropriate value of the upper limit W_c^u has to be selected so that $\int_0^{W_c^u} p_s(W_c)dW_c \approx 1$, such as $W_c^u = 0.000016$ in our case. The upper limit of the random number p in this method is, at least, larger than the maximum $p_s(W_c)$ for any possible W_c. Care should be taken that the P_s, as well as p_s, depends on the batch of pebbles. The $P_s(W_c)$ used in this chapter is derived for pebbles from the batch OSi 07/1.

A unique ID number for each pebble is given randomly. On the other hand, the pair of (W_c, p) is also randomly generated using the Monte Carlo method. Both ID number assignment and the critical energy generation are two independent and random events. Consequently, it can be regarded that pebbles are randomly assigned a critical energy, and the energy distribution satisfies the critical energy distribution for pebbles.

After each pebble is assigned a critical energy, the load level for failure initiation can be derived from numerical simulations with a specified N_f as mentioned above. N_f corresponds to a failure probability $P_f = N_f/N$. Note that N_f/N can not be an arbitrary value since both N_f and N are integers. P_f is set to 0.02% in our simulations. This corresponds to one crushed pebble out of 5000 pebbles in a unit box.

Sphere assemblies are compressed uniaxially, i.e., $\varepsilon_x = \varepsilon_y = 0, \varepsilon_z < 0$, or triaxially, i.e, $\varepsilon_x = \varepsilon_y = \varepsilon_z < 0$, by strain loading. When the first pebble fails, the corresponding macroscopic stress σ_z along the loading direction and the average contact force F_{ave} are taken as the load level for failure initiation. As will be discussed later, many simulations are performed so as to obtain the statistical information for the load level for failure initiation.

Table 6.1: The mean load level with standard deviation (SD) for $P_f = 0.02\%$. For each PF, there are 1000 simulations. 5000 spheres are compressed uniaxially (Uni) and triaxially (Tri).

$N = 5000, N_f = 1$		$\bar{F}_{ave}$ (N)	$\bar{\sigma}_z$ (MPa)
Uni	PF $\approx$ 62.6%	0.450±0.099	2.410±0.568
	PF $\approx$ 63.4%	0.447±0.099	2.547±0.602
	PF $\approx$ 64.0%	0.449±0.097	2.752±0.630
Tri	PF $\approx$ 64.0%	0.518±0.114	2.544±0.583

Table 6.1 shows the mean value of F_{ave} and σ_z along the loading axis, and their standard deviations. For each PF, there are 1000 load levels corresponding to 1000 simulations. For uniaxial loading PF has no influence on $\bar{F}_{ave}$ for failure initiation. $\bar{\sigma}_z$ becomes higher with increasing PF. Since $\bar{F}_{ave}$ and $\bar{\sigma}_z$ denote the same load level, the relation between them thus depends on PF. The loading method will influence both of them. Compared to the uniaxial loading for the same cases

(PF$\approx 64.0\%$), $\bar{F}_{\text{ave}}$ for triaxial loading has increased significantly, but the stress which is the same along each direction decreases to some extent.
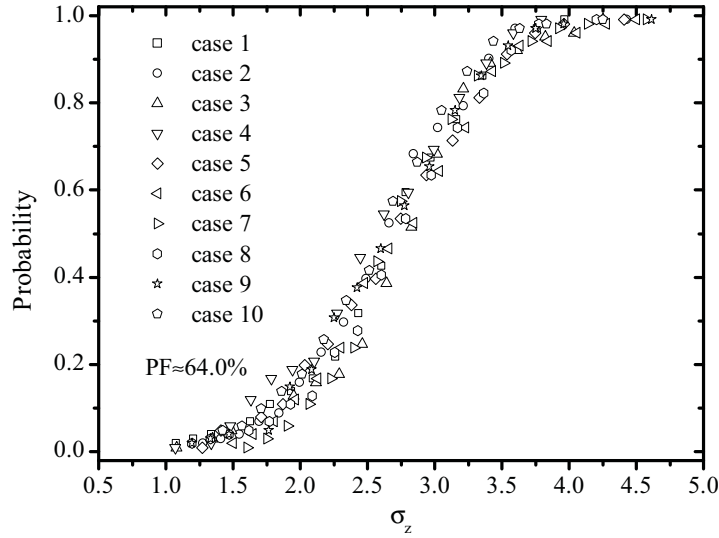
Figure 6.2: Distribution of load levels for $P_{\text{f}} = 0.02\%$. σ_z is the macroscopic stress along the loading axis for uniaxial loading. There are 100 load levels for each case.
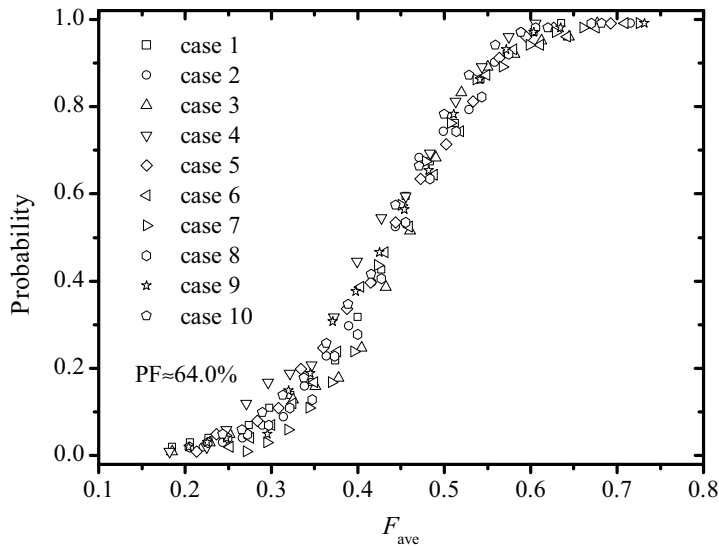
Figure 6.3: Distribution of load levels for $P_{\text{f}} = 0.02\%$. F_{ave} is the average contact force. There are 100 load levels for each case.

The distribution of σ_z for PF$\approx 64.0\%$ subjected to uniaxial loading is shown in Fig. 6.2, and the corresponding F_{ave} is shown in Fig. 6.3. There are ten cases, corresponding to ten different initial configurations with approximately the same packing factor PF$\approx 64.0\%$. For each case, when every sphere is assigned a critical energy using the Monte Carlo method, a load level can be derived from the simulation. If every pebble in the same initial configuration is *randomly* assigned

a critical energy again, the corresponding load level would be different from the former value. For each case in Figs. 6.2 and 6.3 there are 100 load levels for failure initiation since all spheres are randomly assigned critical energies 100 times. The probability estimator $P_i = i/(N+1)$ is the same as the one used in Chapter 2. One can see that the failure initiation could start under a small load level, and the load levels are distributed in a wide range, e.g., σ_z ranging from 1 to 4.6 MPa.

The load level should be exported when only one pebble fails in simulations, in principle. In practice, the strain loading is applied gradually. The failure check of pebbles is made after each load step when the assembly of pebbles reachs an equilibrium state. Although each load step is small, it is found that there are sometimes more than one pebble crushed after a load step. This means the derived load level for $P_f = 0.02\%$ is slightly overestimated.

6.1.2 Numerical-analytical method

The basic assumption of this method is that the distribution of strain energy absorbed by pebbles and the distribution of the strength of singe pebbles are two independent events. Both events are not affected by the failure of pebbles. This assumption seems to be acceptable when a small number of pebbles fail in pebble beds.

Assuming that the failure of spheres is dominated by the maximum contact force, Marketos and Bolton (2007) formulated the failure probability of spheres,

$$P_f = \int_{F_{\min}}^{F_{\max}} p_s(F = \Phi)p(F > \Phi)d\Phi , \tag{6.3}$$

where Φ is the critical contact force, $F_{\min}$ and $F_{\max}$ are the minimum and maximum contact strength (critical contact force) for spheres. p_s is the PDF of the contact strength, and p is the PDF of the maximum contact force in DEM simulations. Equation (6.3) can be extended for other strength distributions, such as, the critical energy distribution in our case,

$$P_f = \int_{W_{\mathrm{cmin}}}^{W_{\mathrm{cmax}}} p_s(W_c = \Phi)p_e(W_a > \Phi)d\Phi = \int_{W_{\mathrm{cmin}}}^{W_{\mathrm{cmax}}} p_s(\Phi)(1 - P_e(\Phi))d\Phi , \tag{6.4}$$

where Φ is the critical energy of pebbles, W_{cmin} and W_{cmax} are the minimum and maximum critical energy for pebbles, and p_e and P_e are the probability density function and the cumulative density function, respectively, for the absorbed strain energy W_a in pebble beds. The failure probability can also be written as

$$P_f = \int_{W_{\mathrm{amin}}}^{W_{\mathrm{amax}}} p_s(W_c < \Phi)p_e(W_a = \Phi)d\Phi = \int_{W_{\mathrm{amin}}}^{W_{\mathrm{amax}}} P_s(\Phi)p_e(\Phi)d\Phi . \tag{6.5}$$

Here, and W_{amin} and W_{amax} are the minimum and maximum strain energy absorbed by pebbles. The cumulative density function $P_s(\Phi) = p_s(W_c \leqslant \Phi) = p_s(W_c < \Phi)$ holds for the continuous distribution function of Eq. (4.26).

The physical meaning of Eq. (6.4) is that for a given critical energy, namely W_c, the pebbles with an absorbed strain energy larger than W_c, i.e., $W_a > W_c$, will fail. The physical meaning of Eq. (6.5) is that for a given strain energy, namely W_a, the pebbles with a critical energy less than W_a, i.e., $W_c < W_a$, will fail. It can be seen that both equations describe the same event in fact. Therefore, they are equivalent.

It should be noted that the necessary condition for Eqs. (6.4) and (6.5) are

$$\int_{W_{cmin}}^{W_{cmax}} p_s d\Phi = 1 \quad \text{and} \quad \int_{W_{amin}}^{W_{amax}} p_e d\Phi = 1 . \tag{6.6}$$

In our case p_s and p_e are fitting functions that are derived from crush tests and DEM simulations, respectively. The fitting parameter W_{cmin} corresponding to the minimum crush load found in crush tests is larger than zero. On the other hand, the derived lower limit W_{amin} could be a negative value. However, the possible W_a can not be negative in practice. Thus, attention should be paid on the integration domain in both Eqs. (6.4) and (6.5). In view of $p_s(\Phi < W_{cmin}) =$
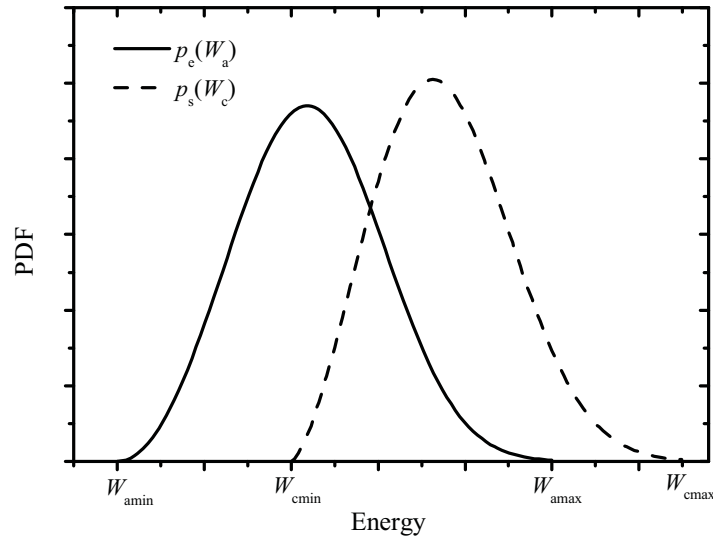
Figure 6.4: Sketch of p_s and p_e.

$p_e(\Phi < W_{amin}) = p_s(\Phi > W_{cmax}) = p_e(\Phi > W_{amax}) = 0$ as shown in Fig. 6.4, the interval in both Eqs. (6.4) and (6.5) can be reduced to $[W_{min}, W_{max}] = [W_{cmin}, W_{cmax}] \cap [W_{amin}, W_{amax}]$. Since W_{cmin} is a positive value, W_{min} is no less than zero as well. If the intersection $[W_{min}, W_{max}]$ is an empty set, the probability P_f is either 0, i.e., for $W_{amax} < W_{cmin}$, or 1, i.e., for $W_{amin} > W_{cmax}$.

Suppose that pebbles will not fail during loading, the strain energy distribution can be obtained in DEM simulations. Figure 6.5 shows the strain energy distribution P_e for different load levels under uniaxial loading. The energy is normalized by W_n corresponding to the strain energy absorbed by a pair of contacting pebbles subjected to a normal load of F_{ave}. There seems to be a master curve for any load level for this case with a PF=64.141%. This master curve has been confirmed for further load levels, and even for other PF for uniaxial loading. The probability at
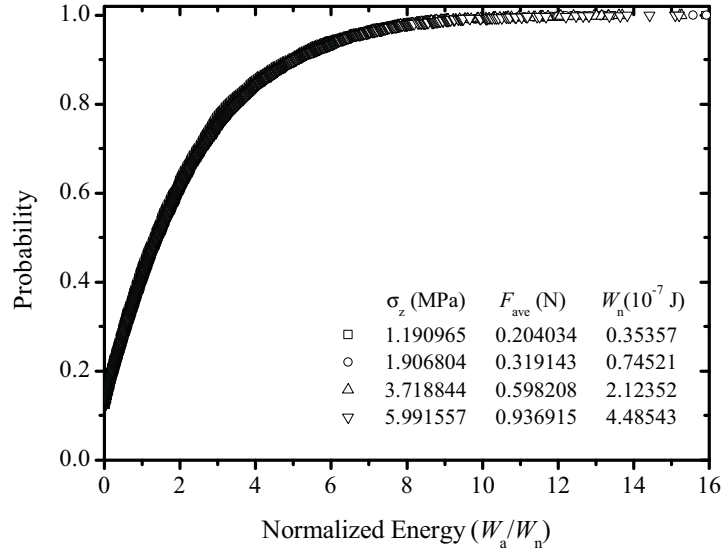
Figure 6.5: Normalized strain energy distribution P_e under different load levels for uniaxial loading.
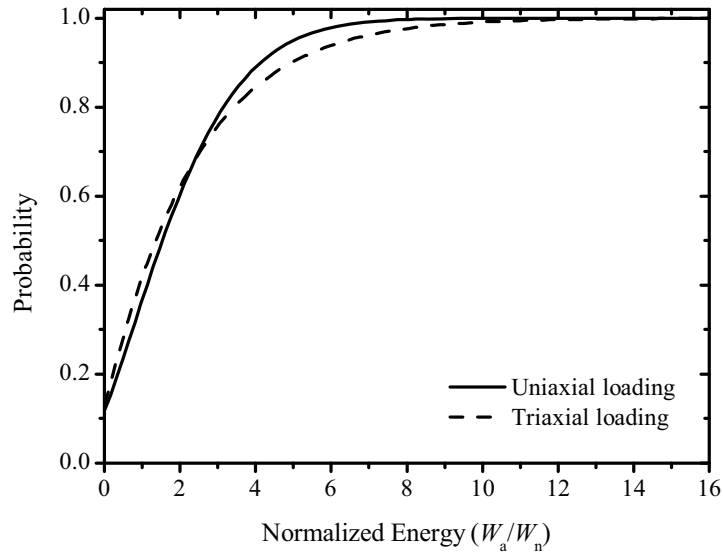
Figure 6.6: Fitting curves for normalized strain energy distribution P_e for uniaxial and triaxial loading.

$W_a = 0$ is approximately 0.12, meaning that about 12% pebbles have no contacts at all during loading. This is possible since gravity is not taken into account. The master curve of P_e for triaxial loading is different from the one for uniaxial loading. Both master curves are fitted by a three parameter Weibull distribution. The fitting curves are shown in Fig. 6.6, and the fitting functions are given by

$$P_e = 1 - \exp\left[-(0.340(W_a + 0.809))^{1.61}\right] \quad \text{for uniaxial loading} \tag{6.7}$$

$$P_e = 1 - \exp\left[-(0.406(W_a + 0.398))^{1.08}\right] \quad \text{for triaxial loading} \tag{6.8}$$
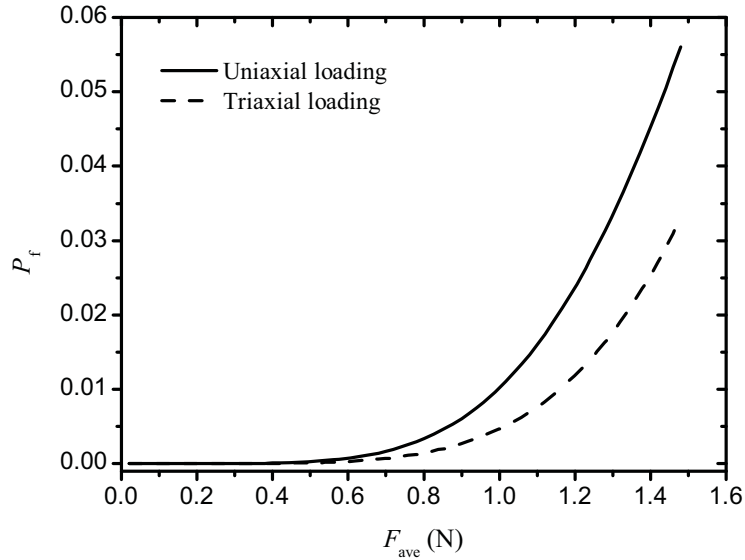
Figure 6.7: Predicted failure probability P_f for pebbles from the batch OSi 07/1 in pebble beds.

Substitution of Eqs. (6.7) and (6.8), respectively, and p_s of (4.26) into (6.4) yields the failure probability P_f for uniaixal and triaxial loading. The results are shown in Fig. 6.7. Besides, the same results can be derived when substituting the PDF of Eqs. (6.7) and (6.8) into (6.4), respectively. It should be noted that the failure probability P_f becomes unreliable with increasing F_{ave} because the true distribution P_e will be modified by crushed pebbles.

6.1.3 Discussion of both methods

The numerical method gives the distribution of load levels for failure initiation. The results correspond to a failure probability P_f or N_f/N given before simulations. This method takes more time since many simulations are required to obtain the statistical information. On the other hand, the numerical-analytical method gives the average load level for failure initiation for any small P_f. This method requires few simulations to derive the energy distribution. Compared to the numerical method, this method supplies less information about the load level, and it is unknown when the prediction is not reliable, i.e., when the energy distribution has greatly changed because of crushed pebbles.

For a failure probability $P_f = 0.02\%$, the predicted load level using the numerical-analytical method is $F_{ave} = 0.466$ N for uniaxial loading, and $F_{ave} = 0.549$ N for triaxial loading. Both of them are a little greater than the corresponding values reported in Table 6.1. This probability may be beyond the applicability of the numerical-analytical method.

6.2 Failure propagation

The pebbles can fail under a small load level according to Fig. 6.2. In other words, the failure of pebbles is almost unavoidable during mechanical loading. Hence, it is essential to study the influence of failure propagation on the macroscopic response. For example, it is of concern how large a fraction of crushed pebbles can influence the macroscopic stress-strain relation.

6.2.1 Characterization of crushed pebble

Two important assumptions are made in this study about the shape of crushed pebbles and their critical energy. As for the shape of crushed pebbles, different failure forms of Li_4SiO_4 pebbles have been found in crush test as reported in Chapter 2. In this chapter it is assumed that the crushed pebbles still have a spherical shape but with a smaller size. A reduction ratio r, defined as the ratio of pebble size after and before failure, is introduced. The ratio ranges from 0 to 1. $r = 0$ corresponds to the case that crushed pebbles are removed, and $r = 1$ corresponds to the case that no failure of pebbles occurs in pebble beds. As for the critical energy for crushed pebbles, it is assumed to be same as before failure. As a result of this assumption, pebbles could fail several times during loading.
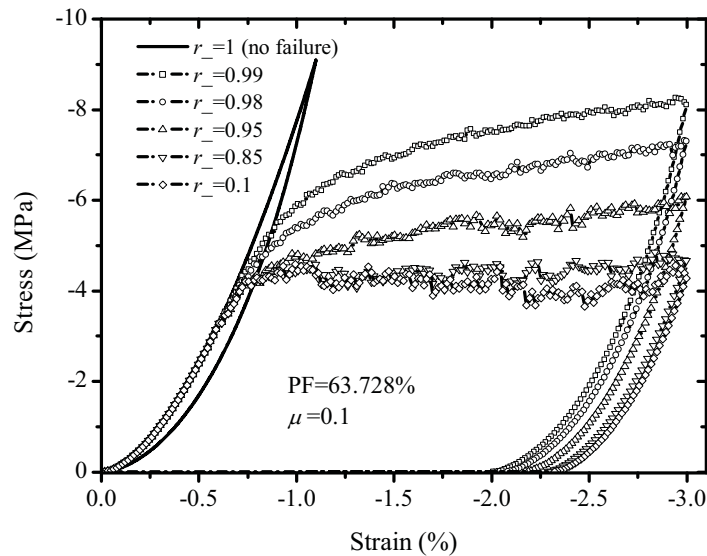
Figure 6.8: Influence of reduction ratio on the stress-strain relation along the loading axis for uniaixal loading.

Figure 6.8 shows the influence of r on the macroscopic stress-strain relation for uniaxial loading. When the size of crushed pebbles is slightly reduced, such as $r = 0.99$, the stress-strain relation changes significantly compared to $r = 1$, i.e., pebbles are non-crushable. A large r can represent that a small fragment of the pebble peels off. It can be seen that the pebble assembly can sustain more load for a big r with increasing strain. On the other hand, a stress plateau

85

is reached beyond a strain of about 0.7% for a r_- less than 0.85. It is found that for a small r_- the crushed pebbles will not fail again, or even have no contacts after failure. Their existence has no contribution to the force chains in pebble beds, and so the macroscopic stress will not be influenced. Therefore, the stress-strain response, i.e., the stress plateau, should be independent of the crushed pebbles for small r_-. It is thus expected that this plateau will exist for the limit case $r_- = 0$, i.e., crushed pebbles are removed. Note that the stress plateau for a smaller r_- will not last forever with increasing strain in real case as the fragments of crushed pebbles will still stay in pebble beds. They can carry load (contact forces) again when the macroscopic strain is very large.

6.2.2 Simulation results
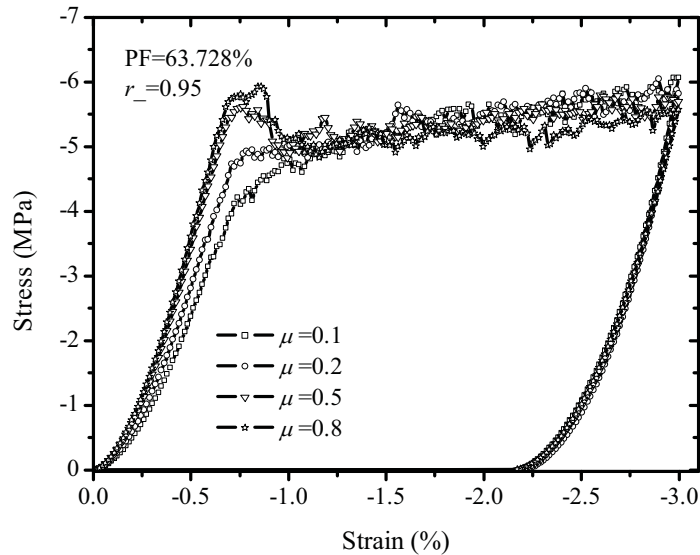
Figure 6.9: Influence of friction coefficient between pebbles on the stress-strain relation along the loading axis for unixial loading for a reduction ratio $r_- = 0.95$

In the following analysis, $r_- = 0.95$ and $r_- = 0.1$ will be considered which correspond to that a small fragment of the pebble peels off and that crushed pebbles have no influence on the stress-strain relation, respectively. Figures 6.9 and 6.10 show the influence of the friction coefficient between pebbles. For both reduction ratios, a large friction coefficient μ gives rise to a high peak stress before the stress plateau. However, the peak stress almost stays the same for $\mu > 0.5$. The effect that stress-strain relation is insensitive to a big μ is similar to that for non-crushable pebbles reported in Chapter 5. The stress plateau becomes independent of the friction coefficient for a large strain.

Figures 6.11 and 6.12 show the influence of PF on the stress-strain relation along the loading axis. For $r_- = 0.95$, a higher initial PF leads to a larger stress at the same strain. The unloading curves show the same stiffness for different initial PF. This should be due to the influence of
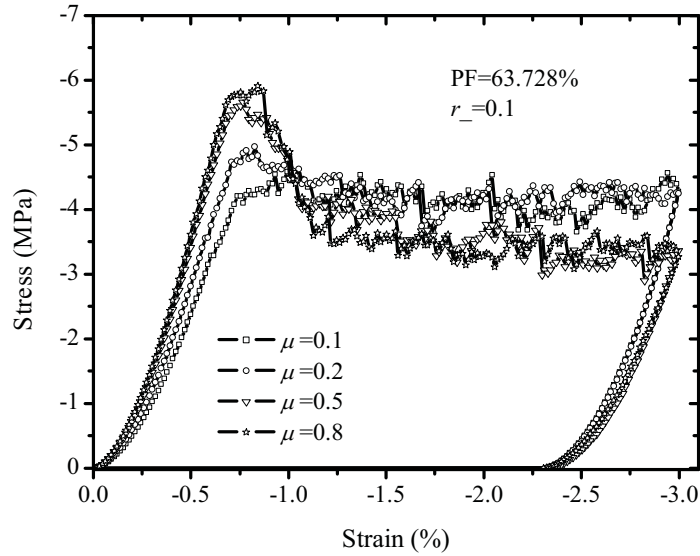
Figure 6.10: Influence of friction coefficient between pebbles on the macroscopic stress-strain relation along the loading axis for a reduction ratio $r_- = 0.1$.
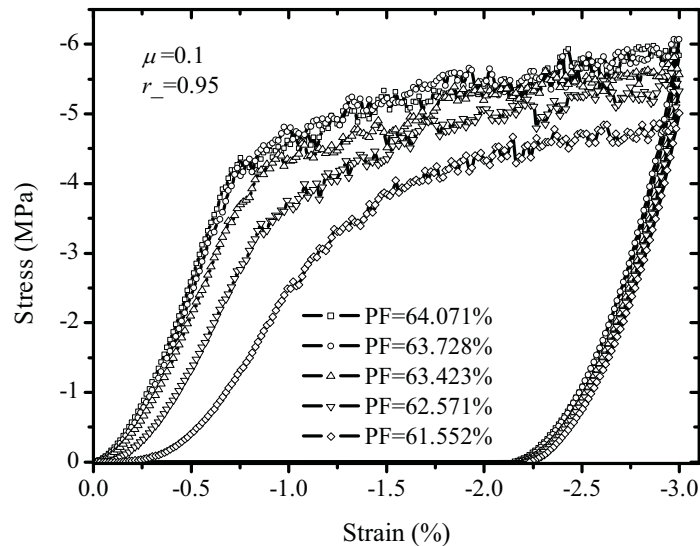
Figure 6.11: Influence of the initial packing factor on the macroscopic stress-strain relation along the loading axis for unixial loading for a reduction ratio $r_- = 0.95$.

crushed pebbles during loading. For $r_- = 0.1$, different PF gives the same stress plateau which begins at different strain.

It is of interest to know how large a fraction of crushed pebbles can affect the macroscopic stress-strain relation. Whether crushed pebbles have influenced the relation can be characterized by giving a critical difference between the stresses for crushable and non-crushable pebbles at the same strain. For example, we can set the critical difference is 5%. For PF=64.071% in Fig. 6.11, there are 11 pebbles crushed during loading to $\varepsilon_z = 0.67\%$ or $\sigma_z = 4.02$ MPa before the
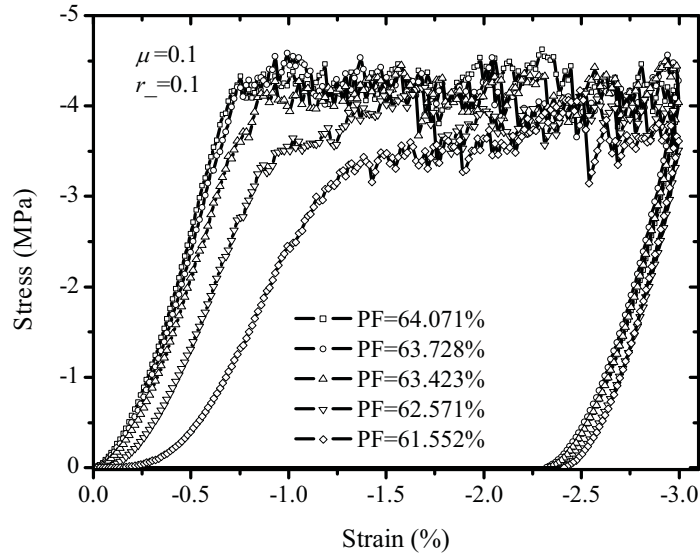
Figure 6.12: Influence of the initial packing factor on the macroscopic stress-strain relation along the loading axis for unixial loading for a reduction ratio $r_- = 0.1$.

stress difference at the same strain reaches 5%. For the same PF with $r_- = 0.1$ in Fig. 6.12, the corresponding P_f is about 0.2% for 10 crushed pebble during loading to $\varepsilon_z = 0.67\%$ or $\sigma_z = 4.0$ MPa.

For a low initial packing factor PF=61.552% in Figs. 6.11 and 6.12, there are 5 pebbles corresponding to $P_f = 0.1\%$ crushed during loading up to $\varepsilon_z = 1\%$ or $\sigma_z = 2.5$ MPa for both $r_- = 0.95$ and 0.1. The stress of pebble beds at $\varepsilon_z = 1\%$ for non-crushable pebbles is about 2.67 MPa. It can be seen that the fraction of crushed pebbles that can affect the stress-strain relation is almost independent of reduction ratios for both PFs. The fraction should depend on the given critical difference, which has to be reasonably small, and PFs.
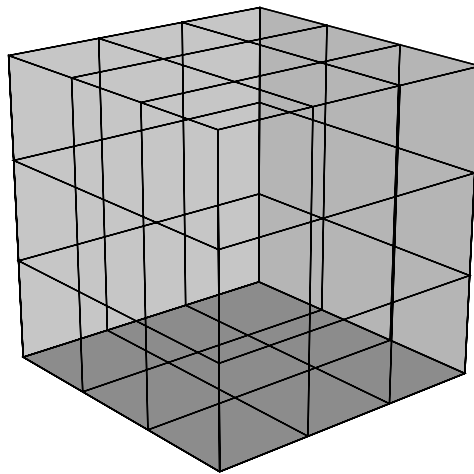
Figure 6.13: 27 equal sub-boxes of the unit box containing all pebbles.

6.2.3 Position distribution

The stress-strain relation exhibits instabilities for a large strain. The drop of stresses corresponds to the failure of pebbles. It is beneficial to know the distribution of the position of crushed pebbles. Marketos and Bolton (2005) have shown the localization of crushed spheres for multi-sized spheres subjected to uniaxial loading. In this chapter we characterize the distribution of the position of crushed pebbles statistically. At first, the unit box containing all pebbles is divided into 27 equal "sub-boxs" as shown in Fig. 6.13. The number of crushed pebbles distributed in each sub-box is counted according to their center position. The mean number of crushed pebbles in each sub-domain is $N_f/27$, and the standard deviation (SD) indicates the scatter of their positions. A small SD denotes that crushed pebbles are distributed uniformly. Table 6.2 shows the statistical information of crushed pebbles.

Table 6.2: Statistic information of the number of crushed pebbles or points falling into each sub-box. N_f crushed pebbles are found during loading up to the maximum strain 3% for PF=63.728%. N_f points are randomly generated in the unit box 2000 times.

r_-	N_f	$N_f/27$	SD*	SD**
0.95	528	19.6	4.11	(2.49, 6.39)
0.1	269	9.96	3.44	(1.83, 4.64)

* SD for DEM simulations; ** miminum and maximum SD for N_f points randomly generated 2000 times.

To indicate the SD for crushed pebbles is small or big, N_f points are randomly generated in the unit box, such that the points satisfy a uniform distribution. The number of these points in each sub-domain is also counted. 2000 SDs are derived by generating N_f points 2000 times. The minimum and maximum values are shown in Table 6.2 for comparison. One can see that the SD for crushed pebbles lies between the minimum and maximum one for uniform distributions, meaning that the distribution of the position of crushed pebbles is fairly uniformly. Localization of crushed pebbles does not happen.

6.3 Summary

The influence of pebble failure is investigated in this chapter. Failure initiation is studied with both a numerical and a numerical-analytical method. According to the results from the numerical method, failure can happen under a very small load level. Therefore, the subsequent failure propagation is studied by introducing a reduction ratio, describing the size of crushed pebbles. A slight reduction of the size of crushed pebble, such as $r_- = 0.99$, will greatly influence the stress-strain relation. On the other hand, below a certain r_- the relation is hardly influenced by crushed pebbles and a stress plateau appears. For large and small reduction ratios, the unloading stiffness

is almost the same. Moreover, the influence of the friction coefficient and PF is also investigated. A biger friction coefficient leads to a larger peak stress before the stress plateau. A lower PF leads to a smaller stress for the same strain. Finally, it is found that there is no localization of crushed pebbles.

Chapter 7
Thermal properties

The volume of pebbles in HCPB blankets will expand mainly because of high temperature and neutron-induced swelling. This will cause thermal stresses in pebble beds as the pebble expansion will be hindered by the structural wall of the breeder unit. Besides, the material parameters like Young's modulus depend on temperature and the porosity of the bulk material (Billone et al., 1993). The reduction of Young's modulus due to high temperature will relieve the thermal stresses. This chapter will investigate the thermal stresses by increasing the size of pebbles while reducing their Young's modulus in DEM. Failure, creep and plastic deformation of pebbles is not taken into account.

The thermal conductivity (TC) of pebble beds is an important design parameter. It depends not only on the TC of the bulk material of pebbles and purge gas, but also the contacts between pebbles. An average method can be used to link the information of individual contacts and the average TC of pebble beds, which is similar to the method to link individual contact forces and the average stress $\bar{\sigma}$ (Gan, 2008). The predicted TC of Li_4SiO_4 pebble beds is validated by experimental results.

Pebbles will be modeled as mono-sized elastic spheres. This should be justified only for Li_4SiO_4 pebbles because Li_2TiO_3 pebbles are of ellipsoidal shape and beryllium pebbles have plastic deformation. Except of the Young's modulus, we will use the material parameters in Table 2.1 for this chapter. The initial sphere size is set to $D = 0.5$ mm.

7.1 Thermal stress

7.1.1 Pebble expansion and Young's modulus decrease

The thermal stresses in pebble beds can be derived from DEM simulations by increasing the sphere size and reducing Young's modulus at the same time. The size of spherical pebbles depends on temperature. The linear thermal expansion for Li_4SiO_4 material is given by (Billone et al., 1993)

$$\frac{\Delta l}{l_0} = 1.267 \times 10^{-5}[1 + 1.065 \times 10^{-3}(T + 273)](T - 25) \,, \tag{7.1}$$

where l_0 is the initial length at room temperature, Δl is the length change, T is the temperature in Celsius. The Young's modulus is given by (Billone et al., 1993)

$$E = 110(1 - \tilde{p})^3 \times [1 - 2.5 \times 10^{-4}(T - 20)] \, (\text{GPa}) \,, \qquad (7.2)$$

where $\tilde{p}$ is the porosity of the bulk material. The porosity of Li_4SiO_4 pebbles ranges from 5% to 6% (Knitter and Alm, 2005). The other material properties of pebbles, such as the Poisson's ratio, are assumed to be independent of temperature and neutron irradiation.

Since the size of pebbles is small compared to the dimension of pebble beds, it is assumed that the temperature in one pebble is uniform while the temperature between pebbles can be different. The temperature of pebbles is expressed as a function of position of their center in this section. The radius of each homogeneous pebble having a uniform temperature will expand according to Eq. (7.1) (Lutz and Zimmerman, 1996). The Young's modulus of each pebble will decrease with increasing temperature according to Eq. (7.2). Accordingly, the thermal stresses of pebble beds can be obtained with respect to temperature. Moreover, the pebble beds can be subjected to thermal loading and strain loading at the same time.
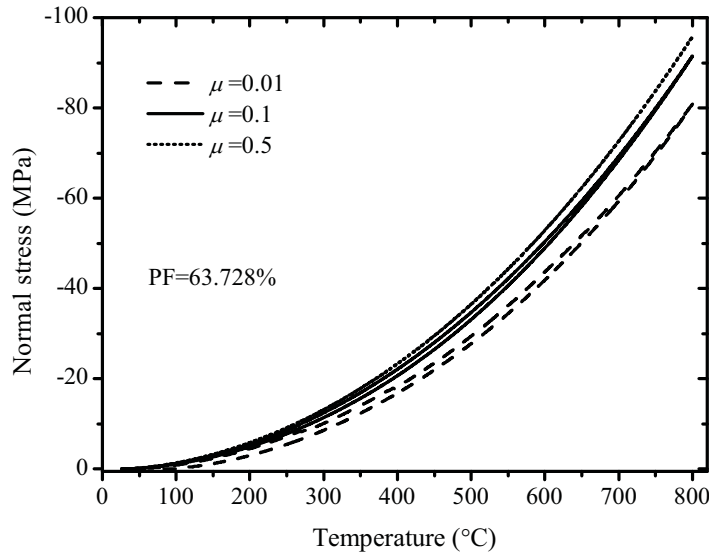
Figure 7.1: Thermal stresses vs temperature for various friction coefficient μ. The normal stresses along each direction are the same, i.e., $\sigma_x = \sigma_y = \sigma_z$. The boudary condition is $\varepsilon_x = \varepsilon_y = \varepsilon_z = 0$. Temperature in pebble beds has a uniform distribution.

The thermal stresses versus temperature for several cases are shown in Figs. 7.1 and 7.2 for 5000 spheres in a cubic box with periodic boundary condition. For these cases, the strain boundary is fixed, i.e., $\varepsilon_x = \varepsilon_y = \varepsilon_z = 0$, during the thermal loading, and a uniform temperature distribution in pebble beds is used, that is, the temperature of every pebble is the same at the same time. Therefore, the macroscopic stresses along each direction are the same.
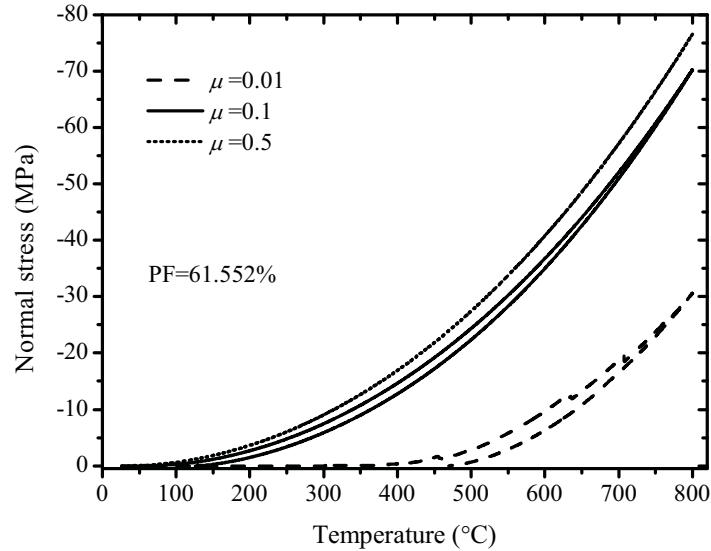
Figure 7.2: Thermal stresses vs temperature for various friction coefficient μ. The normal stresses along each direction are the same, i.e., $\sigma_x = \sigma_y = \sigma_z$. The boudary condition is $\varepsilon_x = \varepsilon_y = \varepsilon_z = 0$. Temperature in pebble beds has a uniform distribution.

At $T = 800\,^{\circ}\text{C}$ the radius of spherical pebbles has increased by about 2.1% compared to its original length at room temperature according to Eq. (7.1). Simulation shows the large thermal stresses due to the expansion of pebbles. It is most probable that some pebbles will fail during loading, which can relieve the thermal stresses to some extent. As a result of failure of pebbles, for the real case at $T = 800\,^{\circ}\text{C}$ the stress will be much lower than that shown in Figs. 7.1 and 7.2. For the relative high packing factor, i.e., PF=63.728%, friction coefficient μ has a small effect on the stress-temperature relation as shown in Fig. 7.1. On the other hand, small friction has an impact on the stress-temperature relation for PF=61.552% as shown in Fig. 7.2. In this case, the stresses are almost zero below $T = 400\,^{\circ}\text{C}$ for $\mu = 0.01$ while it is about 15 MPa at $T = 400\,^{\circ}\text{C}$ for $\mu = 0.1$.

7.1.2 Significance of the thermal analysis

The above thermal analysis for pebble beds is important for the first loading when the effect of plasticity and creep of pebbles is not significant. It is expected that some pebbles start to fail at the stress level reached at a low temperature like $T = 300\,^{\circ}\text{C}$ in view of the failure analysis in Chapter 6. Only the influence of temperature on sphere size and Young's modulus is considered in Fig. 7.1 and 7.2. The effect of neutron irradiation on sphere size and material parameters can be also incorporated in the code, provided that they can quantitatively described like Eqs. (7.1) and (7.2). Moreover, a temperature distribution with respect to positions can be incorporated in the code as well.

7.2 Thermal conductivity

7.2.1 Average method

Volume average of the heat flux over a representative volume V can be written as (Batchelor and O'Brien, 1977)

$$\langle \boldsymbol{q} \rangle = -\boldsymbol{k}^* \cdot \langle \nabla T \rangle \, , \tag{7.3}$$

where $\boldsymbol{q}$ is the local heat flux, the effective TC $\boldsymbol{k}^*$ is a second-rank tensor, ∇T is the temperature gradient at a point in the medium under consideration, and $\langle \boldsymbol{X} \rangle = \frac{1}{V} \int_V \boldsymbol{X} \, dV$ is the volume average of quantity $\boldsymbol{X}$.

In a granular medium, using the Fourier's law $\boldsymbol{q} = -k\nabla T$ on the local scale the average heat flux can be decomposed into

$$
\begin{aligned}
\langle \boldsymbol{q} \rangle =& \frac{1}{V} \int_{V_{\mathrm{m}}} \boldsymbol{q} \, dV + \frac{1}{V} \sum_p \int_{V_{\mathrm{p}}} \boldsymbol{q} \, dV \\
=& -\frac{k}{V} \int_{V_{\mathrm{m}}} \nabla T \, dV - \frac{\alpha k}{V} \sum_p \int_{V_{\mathrm{p}}} \nabla T \, dV \, .
\end{aligned} \tag{7.4}
$$

Here, $V = V_{\mathrm{m}} + \sum V_{\mathrm{p}}$, V_{m} is the volume of the matrix corresponding to the volume of gas in pebble beds, V_{p} is the volume of a particle, and the summation is over all particles in the volume V, k is the isotropic TC of the matrix, and αk is the TC of particles. The above equation can be further simplified as

$$
\begin{aligned}
\langle \boldsymbol{q} \rangle =& -\frac{k}{V} \int_{V_{\mathrm{m}}} \nabla T \, dV - \frac{k}{V} \sum_p \int_{V_{\mathrm{p}}} \nabla T \, dV + \frac{k}{V} \sum_p \int_{V_{\mathrm{p}}} \nabla T \, dV - \frac{\alpha k}{V} \sum_p \int_{V_{\mathrm{p}}} \nabla T \, dV \\
=& -k \langle \nabla T \rangle + \frac{1}{V} \sum_{I=1}^N -(\alpha - 1)k \int_{V_{\mathrm{p}}} \nabla T \, dV \\
=& -k \langle \nabla T \rangle + \frac{1}{V} \sum_{I=1}^N \boldsymbol{S}^I \, ,
\end{aligned} \tag{7.5}
$$

where N is the number of particles in the volume V, and $\boldsymbol{S}^I$ is called the thermal dipole strength of the I-th particle. It indicates the excess of heat flux to that of the matrix material occupying the same volume of I-th particle according to Eq. (7.5). Using the Gauss divergence theorem the dipole stress $\boldsymbol{S}^I$ reads as

$$\boldsymbol{S}^I = -(\alpha - 1)k \int_{V_{\mathrm{p}}} \nabla T \, dV = (1 - \alpha^{-1}) \int_{A_{\mathrm{p}}} \boldsymbol{x} \otimes \boldsymbol{q} \cdot \boldsymbol{n} \, dA \, . \tag{7.6}$$

Here, A_{p} is the surface of the I-th particle, $\boldsymbol{n}$ is the unit vector outward normal to A_{p}, and $\boldsymbol{x}$ is the position vector of a point on A_{p}. The relation $\nabla \cdot \boldsymbol{q} = 0$ corresponding to a steady state has been used to derive Eq. (7.6).
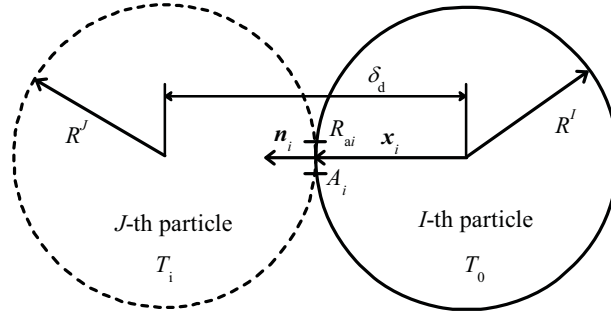
Figure 7.3: i-th contact on the I-th particle. $\boldsymbol{x}_i$ is the local coordinate from the particle center to the contact point. R_{ai} is the radius of the contact area A_i. δ_d is the distance between particle centers. Particles have a homogenous temperature T_0 and T_i, respectively.

Batchelor and O'Brien (1977) derived Eqs. (7.4), (7.5) and (7.6) and concluded that they were exact, and valid for any shape, orientation, and spatial arrangement of the particles which are either randomly or regularly packed. Moreover, for $\alpha \gg 1$ as in our case, Batchelor and O'Brien (1977) have derived the corresponding $\boldsymbol{S}^I$

$$\boldsymbol{S}^I \approx (1 - \alpha^{-1}) \sum_i \boldsymbol{x}_i \int_{A_i} \boldsymbol{q}_i \cdot \boldsymbol{n}_i dA_i = (1 - \alpha^{-1}) \sum_i \boldsymbol{x}_i H_i \,, \tag{7.7}$$

where A_i is the neighborhood of the contact point $\boldsymbol{x}_i$ for the i-th contact on the surface of a particle. It is assumed that $\boldsymbol{x}$ in the area A_i is approximately a constant, i.e., $\boldsymbol{x} = \boldsymbol{x}_i$. The flux H_i depends on the difference between temperatures of two contact particles, i.e., $\Delta T = T_0 - T_i$, as shown in Fig. 7.3. $\sum_i H_i = 0$ holds for every particle in the steady state. A non-dimensional outward heat flux for the i-th contact on the I-th particle between I-th and J-th particles

$$\mathcal{H}^{(I,J)} = H^{(I,J)} / \pi k (T_0 - T_i) 2 R^{*(I,J)} \tag{7.8}$$

was adopted by Batchelor and O'Brien (1977) for spherical particles. $R^{*(I,J)}$ is the radius of relative curvature between the I-th and J-th particles in contact. Batchelor and O'Brien (1977) have derived the analytical solution $\mathcal{H}$ for particles in, or nearly in, contact

$$\mathcal{H} = \mathcal{H}_e(\beta) + \Delta \mathcal{H}_m(\beta) + \ln \alpha^2 + K - 3.9 \,, \tag{7.9}$$

where $\mathcal{H}_e$ is the flux across the contact circle, and $\Delta \mathcal{H}_m$ is the difference between the flux across the matrix layer and the total flux between particles in point contact. Furthermore, $\beta = \alpha R_a / (2R^*)$ is a dimensionless radius of contact circel where R_a is the radius of contact circle (Fig. 7.3), and K is a constant and is independent of whether the particles are actually touching. Both $\mathcal{H}_e$ and $\Delta \mathcal{H}_m$ are non-dimensional quantities which are analytically dervied by Batchelor and O'Brien (1977).

Care should be taken that Eq. (7.7) is valid only when $\alpha \gg 1$. As a result of such an assumption, the temperature within one particle is approximately uniform. More importantly, the heat flux across the contact areas is much larger than across other points on the surface, and hence the flux across the surface points, which are *not* near or in contact areas, is ignored in Eq. (7.7). Besides, the relation $\boldsymbol{x} = \boldsymbol{x}_i$ holds when the contact area is small.

The effective TC can be derived in both local and global coordinate systems. In the local coordinate system, the origin lies in the center of the particle (Fig. 7.3),

$$\boldsymbol{x}_i \approx \frac{R^I}{R^I + R^J} \delta_d \boldsymbol{n}_i \, , \tag{7.10}$$

where δ_d is the distance between the centers of two contacting particles. Equation (7.10) approximately holds when the contact area is small, which has been assumed in Eq. (7.7). With the assumption that the difference between the temperatures at the two sphere centers in a temperature field is exactly linear with the average temperature gradient $\langle \nabla T \rangle$,

$$\Delta T = T_0 - T_i = -\delta_d \boldsymbol{n}_i \cdot \langle \nabla T \rangle \, , \tag{7.11}$$

Substitution of Eqs. (7.10) and (7.11) into (7.8) and (7.7) subsequently yields

$$\boldsymbol{S}^{(I,J)} = -\pi k (1 - \alpha^{-1}) \frac{2R^{*(I,J)} R^I}{R^I + R^J} \sum_i \delta_d^2 \mathcal{H}^{(I,J)} \boldsymbol{n}_i \otimes \boldsymbol{n}_i \cdot \langle \nabla T \rangle \, . \tag{7.12}$$

Note that $\mathcal{H}^{(I,J)} = \mathcal{H}^{(J,I)}$ for the contact pair between I-th and J-th particles according to Eq. (7.8). Substitution Eqs. (7.3) and (7.12) into (7.5) yields

$$\boldsymbol{k}^* = k\mathbf{I} + \frac{\pi k (1 - \alpha^{-1})}{V} 2R^{*(I,J)} \sum_{I<J} \delta_d^2 \mathcal{H}^{(I,J)} \boldsymbol{n} \otimes \boldsymbol{n} \, , \tag{7.13}$$

for an assembly of particles in a periodic boundary condition. $\mathbf{I}$ is the identity matrix. When mono-sized spheres with a radius R are considered, then $2R^{*(I,J)} = R$ (Gan, 2009).

In the global coordinate system, substitution of the global coordinate $\boldsymbol{x}_i$ and Eq. (7.11) into (7.8) and (7.7) subsequently yields

$$\boldsymbol{S}^{(I,J)} = -\pi k (1 - \alpha^{-1}) 2R^{*(I,J)} \sum_i \delta_d \mathcal{H}^{(I,J)} \boldsymbol{x}_i \otimes \boldsymbol{n}_i \cdot \langle \nabla T \rangle \, . \tag{7.14}$$

The terms for contact pairs *inside* the boundaries can be cancelled becasue $\boldsymbol{S}^{(I,J)} = -\boldsymbol{S}^{(J,I)}$ in the global coordinate system. Consequently, compared to the calculation with local coordinates the assumption $\nabla T = \langle \nabla T \rangle$ has to be applied only on the boundaries rather than in the whole medium, meaning that the local gradient ∇T inside the medium and $\langle \nabla T \rangle$ do not have to be equal. For an assembly of particles having a periodic boundary condition, substituting Eqs. (7.3) and (7.14) into (7.5) the effective TC is given by

$$\boldsymbol{k}^* = k\mathbf{I} + \frac{\pi k (1 - \alpha^{-1})}{V} \sum_{I<J} 2R^{*(I,J)} \delta_d \mathcal{H}^{(I,J),\mathrm{BC}} \tilde{\mathbf{L}}^{(J)} \otimes \boldsymbol{n} \, . \tag{7.15}$$

$\mathcal{H}^{(I,J),\mathrm{BC}}$ means the contact across the boundary. The J-th particle has been moved by the periodic length vector $\tilde{\mathbf{L}}^{(J)}$. For mono-sized spheres $2R^{*(I,J)}$ is substituted by R (Gan, 2009).

7.2.2 Thermal conductivity of pebble beds

In pebble beds, gas between pebbles corresponds to the matrix while pebbles correspond to the particles. The TC of bulk material of gas and pebbles can be obtained from experiments. The information of contacts, such as δ_d, β and orientations of contacts, can be obtained from DEM simulation. Therefore, the effective TC can be derived from either Eq. (7.13) or (7.15), provided that $\mathcal{H}(\beta)$ in Eq. (7.9) is known.
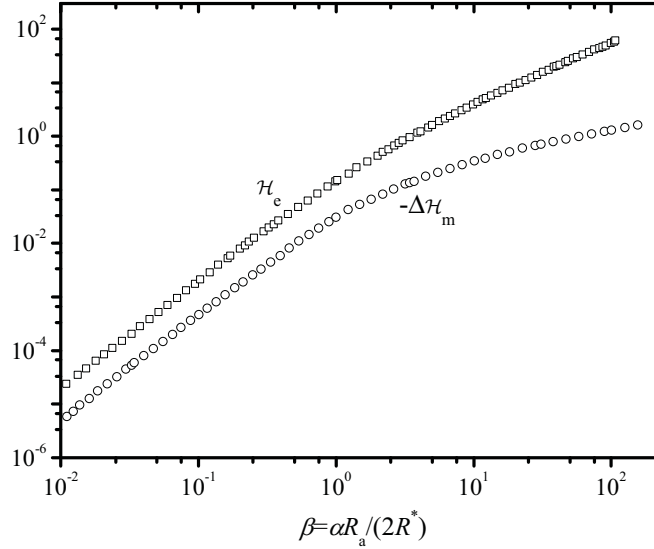
Figure 7.4: Digitalized data of $\mathcal{H}_e$ and $\Delta\mathcal{H}_m$ from the paper Batchelor and O'Brien (1977).

Batchelor and O'Brien (1977) have derived the analytical solution for $\mathcal{H}_e$ and $\Delta\mathcal{H}_m$. This solution has a complicated form. They also provided simple approximation expressions for both of them for two limit cases, i.e., $\beta \to \infty$ and $\beta \ll 1$. Instead of the numerical evaluation of the complicated solution, we digitalize $\mathcal{H}_e$ and $\Delta\mathcal{H}_m$ from the plot in their paper. The curves for the digitalized discrete data are shown in Fig. 7.4. For the limit case $\beta = 0$ both $\mathcal{H}_e$ and $\Delta\mathcal{H}_m$ are equal 0. The values for other β can be obtained by either linear interpolation or extrapolation of the discrete data.

For convenience, the average TC $\boldsymbol{k}^*$ can be rewritten as

$$\boldsymbol{k}^* = \boldsymbol{k}^*_{\text{ini}} + \boldsymbol{k}^*_{\text{inc}} . \tag{7.16}$$

Here, $\boldsymbol{k}^*_{\text{ini}}$ corresponds to the TC before loading while $\boldsymbol{k}^*_{\text{inc}}$ corresponds to the increase of TC induced by loading. In the local coordinate systerm they are given by

$$\boldsymbol{k}^*_{\text{inc}} = \frac{\pi k R(1 - \alpha^{-1})}{V} \sum_{I<J} \delta_d^2 (\mathcal{H}_e^{(I,J)} + \Delta\mathcal{H}_m^{(I,J)}) \boldsymbol{n} \otimes \boldsymbol{n} \tag{7.17}$$

$$\boldsymbol{k}^*_{\text{ini}} = k_{\text{ini}}\mathbf{I} = k\mathbf{I} + \frac{\pi k R(1 - \alpha^{-1})}{V} \sum_{I<J} \delta_d^2 (\ln \alpha^2 + K - 3.9) \boldsymbol{n} \otimes \boldsymbol{n} . \tag{7.18}$$

97

In the global coordinate systerm they are given by

$$\boldsymbol{k}^*_{\mathrm{inc}} = \frac{\pi k R (1 - \alpha^{-1})}{V} \sum_{I < J} \delta_d (\mathcal{H}^{(I,J),\mathrm{BC}}_{\mathrm{e}} + \Delta \mathcal{H}^{(I,J),\mathrm{BC}}_{\mathrm{m}}) \tilde{L} \otimes \boldsymbol{n} \qquad (7.19)$$

$$\boldsymbol{k}^*_{\mathrm{ini}} = k_{\mathrm{ini}} \mathbf{I} = k \mathbf{I} + \frac{\pi k R (1 - \alpha^{-1})}{V} \sum_{I < J} \delta_d (\ln \alpha^2 + K - 3.9) \tilde{L} \otimes \boldsymbol{n} . \qquad (7.20)$$

Here, δ_d is the distance between pebble centers (Fig. 7.3). The corresponding heat flux contribution is considered in $\boldsymbol{k}^*_{\mathrm{ini}}$ and $\boldsymbol{k}^*_{\mathrm{inc}}$ only when the overlapping $\delta = \delta_d - R^I - R^J$ is smaller than or equal to a positive critical value δ_0, i.e., $\delta \leqslant \delta_0$. It is found that $\boldsymbol{k}^*_{\mathrm{ini}}$ highly depends on δ_0. However, δ_0 is not given in the analyses of Batchelor and O'Brien (1977). Furthermore, they did not give a theoretical method to derive the constant K either. On the other hand, when $\delta \geqslant 0$ the dimensionless radius of contact circle β is 0. $\mathcal{H}_{\mathrm{e}}(0) = \Delta \mathcal{H}_{\mathrm{m}}(0) = 0$ for $\beta = 0$ as previously mentioned. Thus, $\boldsymbol{k}^*_{\mathrm{inc}}$ is independent of δ_0. In practice, heat flux between contact pairs having non-zero contact force in the DEM simulations is taken into account in $\boldsymbol{k}^*_{\mathrm{inc}}$. Therefore, $\boldsymbol{k}^*_{\mathrm{inc}}$ can be derived under different mechanical loadings on pebble beds.

In this chapter, the influence of mechanical loading on the heat flux in Li_4SiO_4 pebble beds is investigated by means of the increase of $\boldsymbol{k}^*_{\mathrm{inc}}$. It will be compared to the experimental result $k^{\mathrm{exp}}_{\mathrm{inc}} = k^{\mathrm{exp}} - k^{\mathrm{exp}}_{\mathrm{ini}}$, where $k^{\mathrm{exp}}_{\mathrm{ini}}$ corresponds to the TC of pebble beds before any loading, and k^{exp} corresponds to the TC with respect to macroscopic stresses or strains (Aquaro and Zaccari, 2007; Reimann and Hermsmeyer, 2002). It should be noted that $\boldsymbol{k}^*_{\mathrm{inc}}$ in Eqs. (7.17) and (7.19) is a tensor while the measured TC in experiments is normally a scalar.

A hot wire method has been used by Reimann and Hermsmeyer (2002) to measure the TC of pebbles in a cylindrical container. The equation they used is, in principle, valid for homogeneous isotropic material (Carslaw and Jaeger, 1959; Prelovsek and Uran, 1984). Note that the TC of pebble beds is approximately isotropic before any loading, and the mechanical loading will increase the TC along the loading direction, giving pebble beds an anisotropic TC. The measured data can be regarded as an average TC. Aquaro and Zaccari (2007) used another method to measure the TC of pebble beds. In this case, the TC is calculated from the temperature difference of two plates perpendicular to the loading direction and the heat flux across the plates in a steady state. It corresponds to the component of $\boldsymbol{k}^*$ along the loading direction. The measured $k^{\mathrm{exp}}_{\mathrm{ini}}$ from both experiments is 0.24 W/mK at room temperature in air. Moreover, the maximum k^{exp} at a stress of approximately 6.5 MPa is also the same, i.e., $k^{\mathrm{exp}} = 0.3$ W/mK. The measured data by Reimann and Hermsmeyer (2002) is shown in Fig. 7.5.

The stress-strain relations from both experiments have only a small difference in spite of the significantly different PFs of pebble beds, i.e, PF=64% in Reimann and Hermsmeyer (2002) and 62.5% in Aquaro and Zaccari (2007). Such a difference of PF in DEM will give rise to a big difference between the stress-strain relations. Furthermore, using any practical friction coefficient μ in DEM simulation can not derive comparible stress-strain relation from experiments
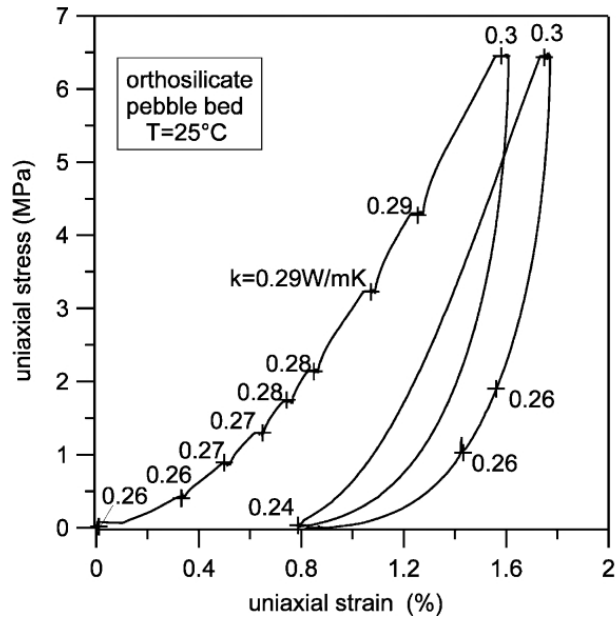
Figure 7.5: Thermal conductivity of Li_4SiO_4 pebble beds subjected to uniaixal loading in air at room temperature. Plot from Ref. Reimann and Hermsmeyer (2002).
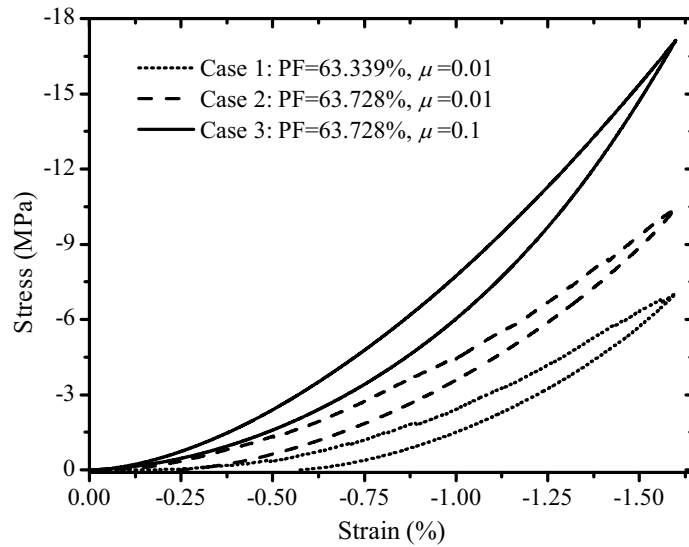
Figure 7.6: Stress-Strain relations along the loading direction derived from DEM for uniaxial loading.

for eitehr PF. Figure 7.6 shows the stress-strain relations for three cases for different PF and friction coefficient subjected to uniaxial loading. The loading curve for PF=63.339% and $\mu = 0.01$ is close to the first loading curve of experiments as shown in Fig. 7.5. Otherwise, the curves show differences. As a result, it is foreseen that a comparison between $k(\varepsilon)$ (calculated or predicted) and $k^{\text{exp}}(\varepsilon)$ for the same strain, and between $k(\sigma)$ and $k^{\text{exp}}(\sigma)$ for the same stress, cannot be satisfied at the same time.
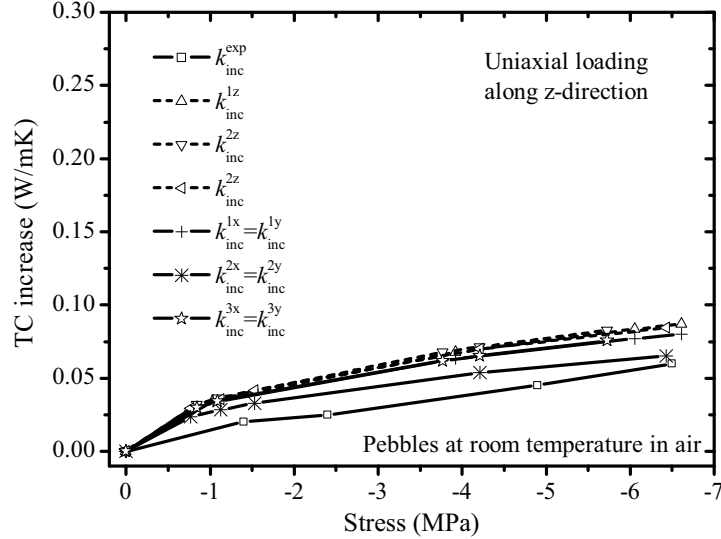
Figure 7.7: Comparison of $k_{\text{inc}}^{\text{exp}}$ (Aquaro and Zaccari, 2007) and predicted increase of TC. k_{inc}^{ix}, k_{inc}^{iy} and k_{inc}^{iz} are the eigenvalues of $\boldsymbol{k}_{\text{inc}}^{*}$ using the contact information of the i-th case in Fig. 7.6.

7.2.3 Validation

At first, the same value for $\boldsymbol{k}_{\text{inc}}^{*}$ can be derived from both local and global coordinate system. The increase of TC because of loading $\boldsymbol{k}_{\text{inc}}^{*}$ is calculated for the three cases whose stress-strain relations are shown in Fig. 7.6. For each case i ($i = 1, 2, 3$), there are three eigenvalues of $\boldsymbol{k}_{\text{inc}}^{*}$, i.e., k_{inc}^{ix}, k_{inc}^{iy} and k_{inc}^{iz}. Uniaxial loading is applied along z-direction, and so $k_{\text{inc}}^{ix} = k_{\text{inc}}^{iy}$. The TC of pebbles and air are 2.8 and 0.025 W/mK, respectively, at room temperature. $k_{\text{ini}}^{\text{exp}}$ is equal to 0.24 W/mK as found in both experiments (Aquaro and Zaccari, 2007; Reimann and Hermsmeyer, 2002).

Figure 7.7 shows the calculated eigenvalues of $\boldsymbol{k}_{\text{inc}}^{*}$ with respected to macroscopic stresses for three stress-strain relations with the three cases. The experimental data $k_{\text{inc}}^{\text{exp}} = k^{\text{exp}} - k_{\text{ini}}^{\text{exp}}$ measured by Aquaro and Zaccari (2007) are also shown in Fig. 7.7. As previously mentioned, the k^{exp} measured by Reimann and Hermsmeyer (2002) is an average value, and that measured by Aquaro and Zaccari (2007) is the component along the loading direction. Nevertheless, they were the same for the same macroscopic stress found in both experiments. It can be seen in Fig. 7.7 that k_{inc}^{z} along the loading direction is a little higher than k_{inc}^{x} and k_{inc}^{y} for the same stress. However, all of them agree well with the experimental results unlike the predictions of the models adopted by Reimann and Hermsmeyer (2002) and Aquaro and Zaccari (2007). It seems that k_{inc} can be characterized in terms of the stress level. Meanwhile, $k_{\text{inc}}(\varepsilon)$ does not agree with $k_{\text{inc}}^{\text{exp}}(\varepsilon)$ for the same strain since the simulated stress-strain relation can be different from the experimental results.

7.2.4 Discussion

The microscopic stress is induced by the contact forces between pebbles. The pebbles that are not in contact with other pebbles will not contribute to the stress. Similarly, only the pebbles in contact, that is, there is a contact force, will be considered into k_{inc}^* according to Eqs. (7.17) and (7.19). Thus, there should be a monotonic relation between stress and k_{inc}^*. It is expected that the increase of new contact pairs and of contact force for existing contact pairs will increase both stress and k_{inc}^* at the same time. On the other hand, the macroscopic strain is composed of combinations from the rearrangement and deformation of pebbles. The rearrangement may decrease the overlapping between pebbles without creating new contact pairs. Such a rearrangement will not influence the macroscopic stress and thermal conductivity. This can be found for pebble beds with a low PF. Applying a small macroscopic strain hardly leads to a macroscopic stress, as well as the thermal conductivity, because of the rearrangement of pebbles. Therefore, it is essential to express the thermal conductivity with respect to stress rather than strain.

The contact information from DEM used for TC calculation includes the distance between pebbles and the size of the contact circles. The dependence on stress of TC implies that the contacts for different PFs and friction coefficient should be statistically the same at the same macroscopic stress. Moreover, the conclusion of a size-independent TC that TC is not affected by the true size of pebbles can be drawn from a similar analysis as performed in Chapter 5.

The failure of pebbles is not taken into account in this chapter. It could have an impact on the prediction. As previously discussed, the macroscopic stress can represent the contact information which decides the average thermal conductivity of pebble beds. Therefore, it is expected that the increase of thermal conductivity can be considered as a stress-dependent value if the failure of pebble is taken into account.

7.3 Summary

Size expansion and change of material parameters have been implemented in the code, which can represent the influence of thermal expansion and neutron-induced swelling. It is shown that the size expansion due to temperature gives rise to significant thermal stresses. It is expected that failure of pebbles, thermal creep and potential plasticity will relieve the stresses. The thermal conductivity of pebble beds is derived using an average method and the contact information from DEM simulations. The predicted increae with stress of the TC at room temperature agrees well with the experimental results.

Chapter 8
Conclusion

First of all, the strength of single Li_4SiO_4 pebbles is analyzed in this work. Crush tests have been carried out so as to supply the necessary experimental results to validate the proposed failure or strength models for pebbles. Since there exist many different theories and models describing the failure of brittle spheres, much effort has been made to find the appropriate models for Li_4SiO_4 pebbles. To utilize the models based on stresses inside an elastic sphere, an analytical solution for the stresses is solved. Anyhow, it is found that all models based on stresses fail to describe the pebble strength. Instead, a proposed probabilistic model with respect to strain energy absorbed by pebbles is validated. Moreover, the underlying mechanism for the failure of pebbles is explained. The applicability of the energy model arises from the stable propagation of the microflaws because of the high stress gradient around the contact circle.

The objective of the crush tests and the analysis of failure models for pebbles is to derive the pebble-pebble contact strength for pebbles in pebble beds. The distribution of critical energy for pebbles is derived with the crush load distribution from Fusion Material Lab (FML) at KIT and the proposed energy model. The pebbles in FML were crushed in dry inert gas, which is similar to the fusion relevant environment, while our crush tests were performed in air. Using the results from FML can exclude the influence of air on the pebble strength. Subsequently, the property of the critical energy for pebbles is imported into DEM. The influence of failure initiation and propagation on the macroscopic stress-strain relation of pebble beds is studied. It is found that pebbles could fail under a small load level, but the macroscopic stress-strain relation is not affected until a number of pebbles are crushed. The crushed pebbles are distributed in the unit box uniformly.

Some input parameters in the DEM code have been investigated. The shear stiffness in the tangential contact model is correlated with the material parameters of pebbles, and so it is not a fitting parameter anymore. It is found that even a small friction coefficient between pebbles has an impact on the stress-strain response for pebble beds. Finally, the relation between the macroscopic stress-strain curves for pebble beds with different mass, size and Young's modulus has been established. This enables the comparison of simulation results derived from other DEM codes.

The thermal stress of pebble beds is investigated by the expansion of pebbles and the decrease

of Young's modulus with increasing temperature. Both size expansion and decrease of Young's modulus depend on temperature. The temperature can have a distribution, i.e., the temperature for each pebble does not have to be always the same. It is found that the thermal stress is very high at a fusion relevant temperature. The other thermal property, i.e., thermal conductivity, is studied using the contact information in pebble beds derived from DEM simulations. The prediction of its increase with stress agrees well with the experimental results.

In the future, several directions seem to be important for thermomechanics of pebble beds. As for the characterization of pebbles, more crush tests for Li_4SiO_4 as well as Li_2TiO_3 pebbles need to be performed so as to further validate the proposed energy model. According to the analysis in Chapter 4, the energy model could fail for pebbles with other sizes. Secondly, the measurement of the friction coefficient between pebbles is very important not only for the failure analysis for pebbles but also for DEM simulations. Finally, the quantitative description of the change of size and material parameters with respect to irradiation is essential for the thermal stress analysis.

As for the DEM code, the ability of the present DEM code needs to be improved. Firstly, multi-sized pebbles can be taken into account. Secondly, ellipsoidal shape for pebbles can be considered. Thirdly, other contact models need to be implemented into the code, such as the Hertz-Mindlin contact model. The contact model plays a substantial role in the DEM analysis. Finally, implementation of different failure criteria of pebbles can be realized. This is mainly related to the characterization of crushed pebbles, such as size, shape, and strength.

Bibliography

A. Abou-Sena, A. Ying, and M. Abdou. Effective thermal conductivity of lithium ceramic pebble beds for fusion blankets: a review. *Fusion Science and Technology*, 47(4):1094–1100, 2005.

L. Afferrante, M. Ciavarella, and E. Valenza. Is Weibull's modulus really a material constant? Example case with interacting collinear cracks. *International Journal of Solids and Structures*, 43(17):5147–5157, 2006.

Z. An, A. Ying, and M. Abdou. Application of discrete element method to study mechanical behaviors of ceramic breeder pebble beds. *Fusion Engineering and Design*, 82(15-24):2233–2238, 2007a.

Z. An, A. Ying, and M. Abdou. Numerical characterization of thermo-mechanical performance of breeder pebble beds. *Journal of Nuclear Materials*, 367-370(Part 2):1393–1397, 2007b.

D. Aquaro. Thermal mechanical analysis of a solid breeding blanket. *Fusion Engineering and Design*, 69(1-4):511–518, 2003.

D. Aquaro and N. Zaccari. Pebble bed thermal-mechanical theoretical model: application at the geometry of test blanket module of ITER-FEAT nuclear fusion reactor. *Fusion Engineering and Design*, 75-79:903–909, 2005.

D. Aquaro and N. Zaccari. Experimental and numerical analysis on pebble beds used in an ITER Test Module Blanket. *Fusion Engineering and Design*, 81(1-7):707–712, 2006.

D. Aquaro and N. Zaccari. Experimental and numerical analyses on $Li_{(4)}SiO_4$ and Li_2TiO_3 pebble beds used in a ITER test blanket module. *Journal of Nuclear Materials*, 367-370(Part 2):1293–1297, 2007.

A.S. Argon, Y. Hori, and E. Orowan. Indentation strength of glass. *Journal of the American Ceramic Society*, 43(2):86–96, 1960.

G.K. Batchelor and R.W. O'Brien. Thermal or electrical conduction through a granular material. *Proceedings of the Royal Society of London. Series A, Mathematical and Physical Sciences*, 355(1682):313–333, 1977.

S.B. Batdorf and J.G. Crose. A statistical theory for the fracture of brittle structures subjected to nonuniform polyaxial stresses. *Journal of Applied Mechanics*, 41:459–464, 1974.

S.B. Batdorf and H.L. Heinisch Jr. Weakest link theory reformulated for arbitrary fracture criterion. *Journal of the American Ceramic Society*, 61(7-8):355–358, 1978.

B. Bergman. On the estimation of the Weibull modulus. *Journal of Materials Science Letters*, 3 (8):689–692, 1984.

N Bicanic. Discrete element methods. In *Encyclopedia of Computational Mechancis*, volume 1, pages 311–337. 2004.

M.C. Billone, W. Dienst, T. Flament, P. Lorenzetto, K. Noda, and N. Roux. ITER solid breeder blanket materials database. ANL/FPP/TM–263, Argonne National Lab., IL (United States), 1993.

L.V. Boccaccini, J.-F. Salavy, O. Bede, H. Neuberger, I. Ricapito, P. Sardain, L. Sedano, and K. Splichal. The EU TBM systems: design and development programme. *Fusion Engineering and Design*, 84(2-6):333–337, 2009.

L. Brendel and S. Dippel. Lasting contacts in molecular dynamics simulations. *NATO ASI Series E Applied Sciences-Advanced Study Institute*, 350:313–318, 1998.

A. Brückner-Foit, P. Hülsmeier, M. Sckuhr, and H. Riesch-Oppermann. Limitations of the Weibull theory in stress fields with pronounced stress gradients. *Proceedings of ASME TUR-BOEXPO 2000, Munich, Germany*, 2000.

L. Bühler. Continuum models for pebble beds in fusion blankets. Report on TW5-TTBB-006-D1, FZK Fusion Nr. 248, 2002.

H.S. Carslaw and J.C. Jaeger. *Conduction of heat in solids*. Oxford University Press, 1959.

K.T. Chau and X.X. Wei. Spherically isotropic, elastic spheres subject to diametral point load strength test. *International Journal of Solids and Structures*, 36(29):4473–4496, 1999.

K.T. Chau, X.X. Wei, R.H.C. Wong, and T.X. Yu. Fragmentation of brittle spheres under static and dynamic compressions: experiments and analyses. *Mechanics of Materials*, 32(9):543–554, 2000.

C.-Y. Chu, K. Bär, J.P. Singh, K.C. Goretta, M.C. Billone, R.B. Poeppel, and J.L. Routbort. Mechanical properties of polycrystalline lithium orthosilicate. *Journal of the American Ceramic Society*, 72(9):1643–1648, 1989.

P.A. Cundall and O.D.L. Strack. A discrete numerical model for granular assemblies. *Geotechnique*, 29(1):47–65, 1979.

M. Dalle Donne and G. Sordon. Heat-transfer in pebble beds for fusion blankets. *Fusion Technology*, 17(4):597–635, 1990.

R. Danzer, P. Supancic, J. Pascual, and T. Lube. Fracture statistics of ceramics-Weibull statistics and deviations from Weibull statistics. *Engineering Fracture Mechanics*, 74(18):2919–2932, 2007.

B.W. Darvell. Uniaxial compression tests and the validity of indirect tensile strength. *Journal of Materials Science*, 25(2):757–780, 1990.

G. Dell'Orco, A. Ancona, A. DiMaio, M. Simoncini, and G. Vella. Thermo-mechanical testing of Li-ceramic for the helium cooled pebble bed (HCPB) breeding blanket. *Journal of Nuclear Materials*, 329-333(Part 2):1305–1308, 2004.

A. Di Renzo and F.P. Di Maio. An improved integral non-linear model for the contact of particles in distinct element simulations. *Chemical engineering science*, 60(5):1303–1312, 2005.

W. Dienst and H. Zimmermann. Investigation of the mechanical properties of ceramic breeder materials. *Journal of Nuclear Materials*, 155-157(Part 1):476–479, 1988.

R.H. Doremus. Fracture statistics: A comparison of the normal, Weibull, and Type I extreme value distributions. *Journal of Applied Physics*, 54(1):193–198, 1983.

A.G. Evans. A general approach for the statistical analysis of multiaxial fracture. *Journal of the American Ceramic Society*, 61(7-8):302–308, 1978.

A.G. Evans. Structural reliability: a processing-dependent phenomenon. *Journal of the American Ceramic Society*, 65(3):127–137, 1982.

T. Fett and D. Munz. Influence of stress gradients on failure in contact strength tests with cylinder loading. *Engineering Fracture Mechanics*, 69(12):1353–1361, 2002.

T. Fett, E. Ernst, D. Munz, D. Badenheim, and R. Oberacker. Weibull analysis of ceramics under high stress gradients. *Journal of the European Ceramic Society*, 23(12):2031–2037, 2003.

A.C. Fischer-Cripps. Predicting Hertzian fracture. *Journal of Materials Science*, 32(5):1277–1285, 1997.

A.C. Fischer-Cripps and R.E. Collins. The probability of Hertzian fracture. *Journal of Materials Science*, 29(8):2216–2230, 1994.

F.C. Frank and B.R. Lawn. On the theory of Hertzian fracture. *Proceedings of the Royal Society of London. Series A, Mathematical and Physical Sciences*, 299(1458):291–306, 1967.

Y. Gan. *Thermo-mechanics of pebble beds in fusion blankets*. PhD Thesis, Universität Karlsruhe (TH), 2008.

Y. Gan. Work report No. 17 in group discussion, 2009.

Y. Gan and M. Kamlah. Identification of material parameters of a thermo-mechanical model for pebble beds in fusion blankets. *Fusion Engineering and Design*, 82(2):189–206, 2007.

Y. Gan and M. Kamlah. Discrete element modelling of pebble beds: with application to uniaxial compression tests of ceramic breeder pebble beds. *Journal of the Mechanics and Physics of Solids*, 58(2):129–144, 2010.

L. Giancarli, M. Ferrari, M.A. Fütterer, and S. Malang. Candidate blanket concepts for a European fusion power plant study. *Fusion Engineering and Design*, 49-50:445–456, 2000.

F.A. Gilabert, J.-N. Roux, and A. Castellanos. Computer simulation of model cohesive powders: influence of assembling procedure and contact laws on low consolidation states. *Physical Review E*, 75(1):011303, 2007.

A.A. Griffith. The phenomena of rupture and flow in solids. *Philosophical Transactions of the Royal Society of London. Series A*, 221:163–198, 1921.

M.K. Gundepudi, B.V. Sankar, J.J. Mecholsky, and D.C. Clupper. Stress analysis of brittle spheres under multiaxial loading. *Powder Technology*, 94(2):153–161, 1997.

J.P. Gyekenyesi and N.N. Nemeth. Surface flaw reliability analysis of ceramic components with the SCARE finite element postprocessor program. *Journal of Engineering for Gas Turbines and Power*, 109:274, 1987.

B. Hamilton and H. Rawson. The determination of the flaw distributions on various glass surfaces from Hertz fracture experiments. *Journal of the Mechanics and Physics of Solids*, 18(2):127–146, 1970.

S. Hermsmeyer and J. Reimann. Particle flow of ceramic breeder pebble beds in bi-axial compression experiments. *Fusion Engineering and Design*, 61-62:367–373, 2002.

H. Hertz. Über die Berührung fester elastischer Körper. *Journal für die reine und angewandte Mathematik*, 92:156–171, 1881.

Y. Hiramatsu and Y. Oka. Determination of the tensile strength of rock by a compression test of an irregular test piece. *International Journal of Rock Mechanics and Mining Sciences*, 3(2): 89–90, 1966.

D. Hofer and M. Kamlah. Drucker-Prager-Cap creep modelling of pebble beds in fusion blankets. *Fusion Engineering and Design*, 73(2-4):105–117, 2005.

H.-C. Hu. On the general theory of elasticity for a spherically isotropic medium. *Acta Scientia Sinica*, 3:247–260, 1954.

M.T. Hüber. Zur Theorie der Berührung fester elastischer Körper. *Annalen der Physik*, 14:153, 1904.

G.R. Irwin. Analysis of stresses and strains near the end of a crack traversing a plate. *AMSE Journal of Applied Mechanics*, 24:361–364, 1957.

H.M. Jaeger, S.R. Nagel, and R.P. Behringer. Granular solids, liquids, and gases. *Reviews of Modern Physics*, 68(4):1259–1273, 1996.

J.C. Jaeger. Failure of rocks under tensile conditions. *International Journal of Rock Mechanics and Mining Science & Geomechanics Abstracts*, 4(2):219–227, 1967.

D. Jelagin and P.L. Larsson. On indentation and initiation of fracture in glass. *International Journal of Solids and Structures*, 45(10):2993–3008, 2008.

W.S. Jodrey and E.M. Tory. Computer simulation of close random packing of equal spheres. *Physical review A*, 32(4):2347–2351, 1985.

C.E. Johnson, K.R. Kummerer, and E. Roth. Ceramic breeder materials. *Journal of Nuclear Materials*, 155-157(Part 1):188–201, 1988.

K.L. Johnson. *Contact mechanics*. Cambridge University Press, 1987.

K.L. Johnson, J.J. O'Connor, and A.C. Woodward. The effect of the indenter elasticity on the Hertzian fracture of brittle materials. *Proceedings of the Royal Society of London. Series A, Mathematical and Physical Sciences*, 334(1596):95–117, 1973.

T. Kanit, S. Forest, I. Galliet, V. Mounoury, and D. Jeulin. Determination of the size of the representative volume element for random composites: statistical and numerical approach. *International Journal of Solids and Structures*, 40(13-14):3647–3679, 2003.

M. Kato, S. Yoshikawa, and K. Nakagawa. Carbon dioxide absorption by lithium orthosilicate in a wide range of temperature and carbon dioxide concentrations. *Journal of Materials Science Letters*, 21(6):485–487, 2002.

R. Knitter. Quality control of lithium orthosilicate pebbles and long-term annealing behavoiur of ceramic breeder materials. Report on TW2-TTBB-002b-D2, FZK Fusion Nr. 220, 2003.

R. Knitter. Fabrication of lithium orthosilicate by melt-spraying: yield and reproducibility. Report on TW4-TTBB-005-D2, FZK Fusion Nr. 231, 2004.

R. Knitter. personal communication, unpublished results, 2010.

R. Knitter and B. Alm. Production and characterisation of lithium orthosilicate pebbles in support of HELICA and HEXCALIBER experiments. Report on TW5-TTBB-006-D1, FZK Fusion Nr. 248, 2005.

R. Knitter, B. Alm, and G. Roth. Crystallisation and microstructure of lithium orthosilicate pebbles. *Journal of Nuclear Materials*, 367-370(Part 2):1387–1392, 2007.

J. Lamon. Statistical approaches to failure for ceramic reliability assessment. *Journal of the American Ceramic Society*, 71(2):106–112, 1988.

J. Lamon and A.G. Evans. Statistical analysis of bending strengths for brittle solids: a multiaxial fracture problem. *Journal of the American Ceramic Society*, 66(3):177–182, 1983.

F.B. Langitan and B.R. Lawn. Hertzian fracture experiments on abraded glass surfaces as definitive evidence for an energy balance explanation of Auerbach's law. *Journal of Applied Physics*, 40(10):4009, 1969.

B. Lawn and R. Wilshaw. Indentation fracture: principles and applications. *Journal of Materials Science*, 10(6):1049–1081, 1975.

B.R. Lawn. Indentation of ceramics with spheres: a century after Hertz. *Journal of the American Ceramic Society*, 81(8):1977–1994, 1998.

B. Löbbecke and R. Knitter. Procurement and quality control of Li_4SiO_4 pebbles for testing of breeder unit mock-ups. Report on TW6-TTBB-006-D2, FZK Fusion Nr. 311, 2007.

B. Löbbecke and R. Knitter. Procurement and quality control of Li_4SiO_4 pebbles for testing of breeder unit mock-ups-OSi 08. FZK Fusion Nr. 338, 2009.

C. Lu, R. Danzer, and F.D. Fischer. Fracture statistics of brittle materials: Weibull or normal distribution. *Physical Review E*, 65(6):67102, 2002a.

C. Lu, R. Danzer, and F.D. Fischer. Influence of threshold stress on the estimation of the Weibull statistics. *Journal of the American Ceramic Society*, 85(6):1640–1642, 2002b.

Z. Lu, A. Ying, and M. Abdou. Numerical and experimental prediction of the thermomechanical performance of pebble beds for solid breeder blanket. *Fusion Engineering and Design*, 49-50: 605–611, 2000.

M.P. Lutz and R.W. Zimmerman. Thermal stresses and effective thermal expansion coefficient of a functionally gradient sphere. *Journal of Thermal Stresses*, 19(1):39–54, 1996.

G. Marketos and M.D. Bolton. Compaction bands as observed in DEM simulations. In *Proceedings of the 5th International Conference on Micromechanics of Granular Media, Powders and Grains*, pages 1405–1409, 2005.

G. Marketos and M.D. Bolton. Quantifying the extent of crushing in granular materials: a probability-based predictive method. *Journal of the Mechanics and Physics of Solids*, 55(10): 2142–2156, 2007.

G.R. McDowell and A. Amon. The application of weibull statistics to the fracture of soil particles. *Soils and foundations*, 40(5):133–141, 2000.

M. Meier, E. John, D. Wieckhusen, W. Wirth, and W. Peukert. Influence of mechanical properties on impact fracture: prediction of the milling behaviour of pharmaceutical powders by nanoindentation. *Powder Technology*, 188(3):301–313, 2009.

R.D. Mindlin. Compliance of elastic bodies in contact. *Journal of Applied Mechanics*, 16(3): 259–268, 1949.

R.D. Mindlin and H. Deresiewicz. Elastic spheres in contact under varying oblique forces. *Journal of Applied Mechanics*, 20(3):327–344, 1953.

M.A. Mooney, R.J. Finno, and M.G. Viggiani. A unique critical state for sand? *Journal of Geotechnical and Geoenvironmental Engineering*, 124(11):1100–1108, 1998.

D. Munz and T. Fett. *Ceramics: mechanical properties, failure behaviour, materials selection.* Springer Verlag, 1999.

M. Oda, H. Kazama, and J. Konishi. Effects of induced anisotropy on the development of shear bands in granular materials. *Mechanics of Materials*, 28(1-4):103–111, 1998.

G. Piazza, M. Enoeda, and A. Ying. Measurements of effective thermal conductivity of ceramic breeder pebble beds. *Fusion Engineering and Design*, 58-59:661–666, 2001a.

G. Piazza, J. Reimann, E. Günther, R. Knitter, N. Roux, and J.D. Lulewicz. Behaviour of ceramic breeder materials in long time annealing experiments. *Fusion Engineering and Design*, 58-59: 653–659, 2001b.

G. Piazza, J. Reimann, E. Günther, R. Knitter, N. Roux, and J.D. Lulewicz. Characterisation of ceramic breeder materials for the helium cooled pebble bed blanket. *Journal of Nuclear Materials*, 307:811–816, 2002.

G. Piazza, A. Erbe, R. Rolli, and O. Romer. Post-irradiation examinations of Li_4SiO_4 pebbles irradiated in the EXOTIC-8 experiment. *Journal of Nuclear Materials*, 329-333(Part 2):1260–1265, 2004.

Y. Poitevin, L.V. Boccaccini, A. Cardella, L. Giancarli, R. Meyder, E. Diegele, R. Laesser, and G. Benamati. The European breeding blankets development and the test strategy in ITER. *Fusion Engineering and Design*, 75-79:741–749, 2005.

P. Prelovsek and B. Uran. Generalised hot wire method for thermal conductivity measurements. *Journal of Physics E: Scientific Instruments*, 17:674, 1984.

A.T. Procopio and A. Zavaliangos. Simulation of multi-axial compaction of granular media from loose to high relative densities. *Journal of the Mechanics and Physics of Solids*, 53(7):1523–1551, 2005.

J. Reimann and S. Hermsmeyer. Thermal conductivity of compressed ceramic breeder pebble beds. *Fusion Engineering and Design*, 61-62:345–351, 2002.

J. Reimann and G. Wörner. Thermal creep of ceramic breeder pebble beds. CBBI-9, 9th Intern. Workshop on Ceramic Breeder Blanket Interactions, Toki, Japan, Sep. 27-29, 2000.

J. Reimann and G. Wörner. Thermal creep of Li_4SiO_4 pebble beds. *Fusion Engineering and Design*, 58-59:647–651, 2001.

J. Reimann, E. Arbogast, M. Behnke, S. Müller, and K. Thomauske. Thermomechanical behaviour of ceramic breeder and beryllium pebble beds. *Fusion Engineering and Design*, 49: 643–649, 2000.

J. Reimann, L. Boccaccini, M. Enoeda, and A. Ying. Thermomechanics of solid breeder and Be pebble bed materials. *Fusion Engineering and Design*, 61-62:319–331, 2002a.

J. Reimann, J.D. Lulewicz, N. Roux, and G. Wörner. Thermal creep of metatitanate ceramic breeder pebble beds. CBBI-10, 10th Intern. Workshop on Ceramic Breeder Blanket Interactions, Karlsruhe, Germany, Oct. 22-24, 2001, FZKA 6720, June, 2002b.

J. Reimann, D. Ericher, and G. Wörner. Influence of pebble bed dimensions and filling factor on mechanical pebble bed properties. *Fusion Engineering and Design*, 69(1-4):241–244, 2003.

J. Reimann, R. Knitter, and G. Piazza. New compilation of the material data base and the material assessment report. Report on TW5-TTBB-006-D2, IKET-Nr. 13/05, 2005.

J. Reimann, R.A. Pieritz, and R. Rolli. Topology of compressed pebble beds. *Fusion Engineering and Design*, 81(1-7):653–658, 2006.

J. Reimann, R.A. Pieritz, C. Ferrero, M. di Michiel, and R. Rolli. X-ray tomography investigations on pebble bed structures. *Fusion Engineering and Design*, 83(7-9):1326–1330, 2008.

H. Riesch-Oppermann, M. Hartelt, and O. Kraft. STAU-a review of the Karlsruhe weakest link finite element postprocessor with extensive capabilities. *Zeitschrift fur Metallkunde/International Journal of Materials Research*, 99(10), 2008.

F.C. Roesler. Indentation hardness of glass as an energy scaling law. *Proceedings of the Physical Society. Section B*, 69:55, 1956a.

F.C. Roesler. Brittle fractures near equilibrium. *Proceedings of the Physical Society. Section B*, 69:981, 1956b.

R. Rolli. personal communication, unpublished results, 2008.

C. Ruggieri and R.H. Dodds. Numerical evaluation of probabilistic fracture parameters using WSTRESS. *Engineering Computations*, 15(1):49–73, 1998.

G. Schumacher, M. Dalle Donne, and S. Dorner. Properties of lithium orthosilicate spheres. *Journal of Nuclear Materials*, 155-157(Part 1):451–454, 1988.

P.H. Shipway and I.M. Hutchings. Fracture of brittle spheres under compression and impact loading. II. Results for lead-glass and sapphire spheres. *Philosophical Magazine A*, 67(6): 1405–1421, 1993.

H. Tanigawa, T. Hatano, M. Enoeda, and M. Akiba. Effective thermal conductivity of a compressed Li_2TiO_3 pebble bed. *Fusion Engineering and Design*, 75:801–805, 2005.

F. Tehranian and M.A. Abdou. Experimental study of the effect of external pressure on particle bed effective thermal properties. *Fusion Technology*, 27(3):298–313, 1995.

F. Tehranian, M.A. Abdou, and M.S. Tillack. Effect of external pressure on particle bed effective thermal conductivity. *Journal of Nuclear Materials*, 212:885–890, 1994.

J.P.A. Tillett. Fracture of glass by spherical indenters. *Proceedings of the Physical Society. Section B*, 69:47, 1956.

P. Toneva and W. Peukert. A general approach for the characterization of fragmentation problems. *Advanced Powder Technology*, 18(1):39–51, 2007.

K. Tsuchiya, H. Kawamura, T. Takayama, and S. Kato. Control of particle size and density of Li_2TiO_3 pebbles fabricated by indirect wet processes. *Journal of Nuclear Materials*, 345(2-3): 239–244, 2005.

K. Tsuchiya, H. Kawamura, and S. Tanaka. Evaluation of contact strength of Li_2TiO_3 pebbles with different diameters. *Fusion Engineering and Design*, 81(8-14):1065–1069, 2006.

M. Übeyli. On the tritium breeding capability of flibe, flinabe, and $Li_{20}Sn_{80}$ in a fusion-fission (hybrid) reactor. *Journal of Fusion Energy*, 22(1):51–57, 2003.

J.G. van der Laan and R.P. Muis. Properties of lithium metatitanate pebbles produced by a wet process. *Journal of Nuclear Materials*, 271-272:401–404, 1999.

L. Vogel and W. Peukert. Characterisation of grinding-relevant particle properties by inverting a population balance model. *Particle & Particle Systems Characterization*, 19(3):149–157, 2002.

L. Vogel and W. Peukert. Breakage behaviour of different materials–construction of a mastercurve for the breakage probability. *Powder Technology*, 129(1-3):101–110, 2003.

L. Vogel and W. Peukert. Determination of material properties relevant to grinding by practicable labscale milling tests. *International Journal of Mineral Processing*, 74:S329–S338, 2004.

D. Vollath, H. Wedemeyer, H. Zimmermann, and H. Werle. Doped lithium orthosilicate: preparation and properties. *Journal of Nuclear Materials*, 174(1):86–91, 1990.

L. Vu-Quoc and X. Zhang. An accurate and efficient tangential force-displacement model for elastic frictional contact in particle-flow simulations. *Mechanics of materials*, 31(4):235–269, 1999.

L. Vu-Quoc, X. Zhang, and L. Lesburg. Normal and tangential force-displacement relations for frictional elasto-plastic contact of spheres. *International journal of solids and structures*, 38 (36-37):6455–6489, 2001.

W. Weibull. A statistical theory of the strength of material. *Ingeniors Vetenskap Akademins, Stockholm*, Handlingar Nr 151, 1939.

W. Weibull. A statistical distribution function of wide applicability. *Journal of Applied Mechanics-transactions of the Asme*, 18(3):293–297, 1951.

G. Wijk. Some new theoretical aspects of indirect measurements of the tensile strength of rocks. *International Journal of Rock Mechanics and Mining Sciences and Geomechanics Abstract*, 15 (4):149–160, 1978.

A. Ying, H. Huang, and M. Abdou. Numerical simulation of ceramic breeder pebble bed thermal creep behavior. *Journal of Nuclear Materials*, 307-311(Part 1):827–831, 2002.

N. Zaccari and D. Aquaro. Mechanical characterization of Li_2TiO_3 and Li_4SiO_4 pebble beds: experimental determination of the material properties and of the pebble bed effective values. *Fusion Engineering and Design*, 82(15-24):2375–2382, 2007.

N. Zaccari and D. Aquaro. Experimental characterization of ceramic pebble beds. *Journal of Nuclear Materials*, 386-388:1078–1082, 2009.

Appendices

I Displacement potential functions

The displacement potential functions Z and Φ are derived by Chau and Wei (1999). The way how they are derived is shown below.

Hu (1954) proposed that the displacements under consideration can be resolved into two parts

$$u_r = u_r^I + u_r^{II} = 0 + w \tag{I.1}$$

$$u_\theta = u_\theta^I + u_\theta^{II} = -\frac{1}{r\sin\theta}\frac{\partial \Psi}{\partial \varphi} - \frac{1}{r}\frac{\partial G}{\partial \theta} \tag{I.2}$$

$$u_\varphi = u_\varphi^I + u_\varphi^{II} = \frac{1}{r}\frac{\partial \Psi}{\partial \theta} - \frac{1}{r\sin\theta}\frac{\partial G}{\partial \varphi}\,, \tag{I.3}$$

where Ψ and G are two displacement functions.

Substitution of the above equations into Eqs.(3.4) and (3.6) subsequently yields

$$\frac{2(a+b)}{r^3}\nabla_1^2 G - \frac{d}{r^2}\nabla_1^2\frac{\partial G}{\partial r} + \frac{2g}{r^2}w + \frac{c}{r^2}\frac{\partial}{\partial r}\left(r^2\frac{\partial w}{\partial r}\right) + \frac{h}{r^2}\nabla_1^2 w = 0 \tag{I.4}$$

$$\frac{1}{r}\frac{\partial B}{\partial \theta} + \frac{1}{r\sin\theta}\frac{\partial A}{\partial \varphi} = 0,\ \frac{1}{r}\frac{\partial A}{\partial \theta} - \frac{1}{r\sin\theta}\frac{\partial B}{\partial \varphi} = 0\,, \tag{I.5}$$

where

$$A = -\frac{a}{r^2}\nabla_1^2 G + \frac{2b}{r^2}G - h\frac{\partial^2 G}{\partial r^2} + \frac{2(a+b)}{r}w + d\frac{\partial w}{\partial r}$$
$$B = (h-b)\left(\frac{1}{r^2}\nabla_1^2\Psi + \frac{2\Psi}{r^2}\right) + h\left(\frac{\partial^2\Psi}{\partial r^2} - \frac{2\Psi}{r^2}\right) \tag{I.6}$$

$$a = A_{12} + 2A_{66},\ b = A_{44} - A_{66},\ c = A_{33}$$
$$d = A_{13} + A_{44},\ h = A_{44},\ g = d + h - 2(a+b)\,. \tag{I.7}$$

It has been proved that both A and B can be set to zero:

$$A = 0,\ B = 0\,. \tag{I.8}$$

The following change of variables is introduced

$$r = Re^\eta, \ \Psi = RZe^\eta, \ G = RFe^\eta, \ w = -r\frac{\partial H}{\partial r} = -\frac{\partial H}{\partial \eta} \ , \tag{I.9}$$

where Z,F and H are displacement functions with respect to the dimensionless radial variable η.

Substitution of the above variables into Eqs. (I.4), (I.6) and (I.8) yields Eq. (3.18)

$$A_{44}\Big(\frac{\partial^2 Z}{\partial \eta^2} + \frac{\partial Z}{\partial \eta}\Big) + A_{66}\nabla_1^2 Z - 2(A_{44} - A_{66})Z = 0$$

and

$$\Big[h\Big(\frac{\partial^2}{\partial \eta^2} + \frac{\partial}{\partial \eta}\Big) + a\nabla_1^2 - 2b\Big]F + \Big[d\frac{\partial^2}{\partial \eta^2} + 2(a+b)\frac{\partial}{\partial \eta}\Big]H = 0 \tag{I.10}$$

$$\Big[(h-g)\nabla_1^2 - d\nabla_1^2\frac{\partial}{\partial \eta}\Big]F - \Big[c\Big(\frac{\partial^3}{\partial \eta^3} + \frac{\partial^2}{\partial \eta^2}\Big) + h\nabla_1^2\frac{\partial}{\partial \eta} + 2g\frac{\partial}{\partial \eta}\Big]H = 0 \ . \tag{I.11}$$

Another displacement function ϕ is introduced to uncouple F and H in Eqs. (I.10) and (I.11):

$$F = \Big[d\frac{\partial^2}{\partial \eta^2} + 2(a+b)\frac{\partial}{\partial \eta}\Big]\phi \tag{I.12}$$

$$H = -\Big[h\Big(\frac{\partial^2}{\partial \eta^2} + \frac{\partial}{\partial \eta}\Big) + a\nabla_1^2 - 2b\Big]\phi \ . \tag{I.13}$$

It can be seen that such ϕ does satisfy Eq. (I.10). Substitution of Eqs. (I.12) and (I.13) into Eq. (I.11) leads to Eq. (3.19), i.e.,

$$\Big[\Big(\frac{\partial^2}{\partial \eta^2} + \frac{\partial}{\partial \eta}\Big)^2 + 2D\Big(\frac{\partial^2}{\partial \eta^2} + \frac{\partial}{\partial \eta}\Big) + M\nabla_1^2\Big(\frac{\partial^2}{\partial \eta^2} + \frac{\partial}{\partial \eta}\Big) - 4L + 2(N-L)\nabla_1^2 + N\nabla_1^2\nabla_1^2\Big]\Phi = 0 \ ,$$

where

$$D = \frac{hg-bc}{ch}, \ L = \frac{bg}{ch}, \ M = \frac{ac+h^2-d^2}{ch}, \ N = \frac{a}{c} \ , \tag{I.14}$$

and Φ is defined as

$$\Phi = -\frac{\partial \phi}{\partial \eta} \ . \tag{I.15}$$

Subsequently, the displacement functions can be expressed by Z and Φ, i.e., Eq. (3.20).

II Fourier associated Legendre series

For the asymmetric boundary conditions, the piecewise pressure function, $p(\theta, \varphi)(0 \leqslant \theta \leqslant \pi, 0 \leqslant \varphi \leqslant 2\pi,)$, can be expanded with the orthogonal functions

$$\left\{ P_n^m(\cos\theta)\cos m\varphi \; (n \geqslant 0, n \geqslant m \geqslant 0), P_k^l(\cos\theta)\sin l\varphi \; (k > 0, k \geqslant l > 0) \right\} \tag{II.1}$$

where P_n^m and P_k^l are the associated Legendre functions, and n, m, k, l are integers.

The orthogonality relations for any two functions in the above system are

$$\int_0^\pi \int_0^{2\pi} P_n^m(\cos\theta)\cos m\varphi P_k^l(\cos\theta)\sin l\varphi \sin\theta d\varphi d\theta = 0 \tag{II.2}$$

$$\int_0^\pi \int_0^{2\pi} \left(P_n^m(\cos\theta)\cos m\varphi \right)^2 \sin\theta d\varphi d\theta = \frac{2\pi\delta_m(n+m)!}{(2n+1)(n-m)!} \tag{II.3}$$

$$\int_0^\pi \int_0^{2\pi} \left(P_k^l(\cos\theta)\sin l\varphi \right)^2 \sin\theta d\varphi d\theta = \frac{2\pi(k+l)!}{(2k+1)(k-l)!}\,, \tag{II.4}$$

where $\sin\theta$ is a wight function and

$$\delta_m = \begin{cases} 2 & m = 0 \\ 1 & m \neq 0\,. \end{cases} \tag{II.5}$$

So the function p can be expanded as

$$p(\theta, \varphi) = \sum_{n=0}^{\infty} \sum_{m=0}^{m=n} \left(A_n^m \cos m\varphi + B_n^m \sin m\varphi \right) P_n^m(\cos\theta)\,, \tag{II.6}$$

where

$$\begin{aligned} A_n^m &= \frac{(2n+1)(n-m)!}{2\pi\delta_m(n+m)!} \int_0^\pi \int_0^{2\pi} p(\theta, \varphi) P_n^m(\cos\theta)\cos m\varphi \sin\theta d\varphi d\theta \\ B_n^m &= \frac{(2n+1)(n-m)!}{2\pi(n+m)!} \int_0^\pi \int_0^{2\pi} p(\theta, \varphi) P_n^m(\cos\theta)\sin m\varphi \sin\theta d\varphi d\theta\,. \end{aligned} \tag{II.7}$$
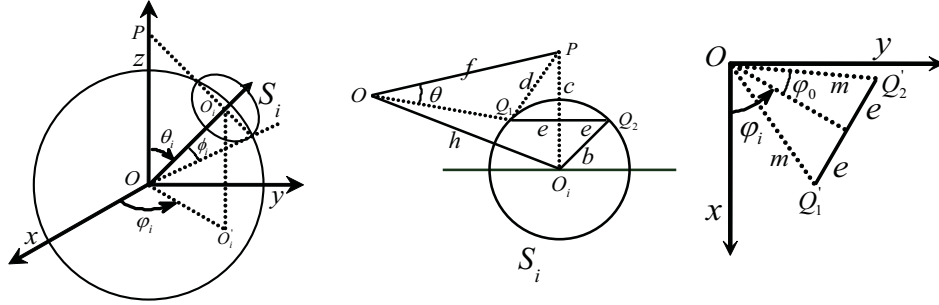
III   The domain of integration

Figure III.1: The domain of the load area.

The load circle, S_i, is represented by an ellipse in the left sketch of Fig. III.1. O_i is the center of the load circle correponding to $(R\cos\phi_i, \theta_i, \varphi_i)$ in the spherical coordinate system, where R is the sphere radius. The spherical load circle subtends an angle of $2\phi_i$. O is the center of the sphere and P is a point in the z-axis. O_i' is the projection of O_i in the x-y plane. The line across the points O_i and P lie in the plane containing the load circle. The plane cross the points O, P and O_i is perpendicular to the load circle. The points Q_1 and Q_2 corresponding to the same θ locate at the edge of S_i. The line across the points Q_1 and Q_2 is parallel to the x-y plane. Q_1' and Q_2' in the right sketch are the projection of Q_1 and Q_2 in the x-y plane. It is aimed to find the function of $\varphi_0(\theta)$.

Care should be taken that the spherical coordinate system must be appropriately chosen so that every load lies in $\phi_i < \theta_i < \pi - \phi_i$. Otherwise, *if z-axis goes through the inner of load circle, the following construction will not work.* Nevertheless, an appropriate coordinate system can be normally found due to the limited coordination number and the small load area. The coordination number is limited for spheres with a similar size. For example, the maximum coordination number in a three dimensional space is 12 for mono-sized spheres. Besides, for ceramic spherical pebbles compressed by plates, the ϕ_i which is related to the i-th load area is relatively small before failure occurs. Therefore, it will not be a big issue to identify the available coordinate system.

The geometrical relations read as

$$b = R\sin\phi_i, \ h = R\cos\phi_i, \ c = h|\tan\theta_i|, \ f = h|\sec\theta_i|, \ d = \sqrt{R^2 + f^2 - 2Rf|\cos\theta|}$$

$$p = \frac{b+c+d}{2}, \ e = \frac{2\sqrt{p(p-c)(p-b)(p-d)}}{c}, \ m = R\sin\theta, \ \varphi_0(\theta) = \arcsin\frac{e}{m} \ .$$

$$\tag{III.1}$$

There is a special case for the load area with $\theta_i = \pi/2$. In this case,

$$\varphi_0(\theta) = \arcsin \frac{\sqrt{b^2 - (R\cos\theta)^2}}{m} = \frac{\sqrt{\sin^2\phi_i - \cos^2\theta}}{\sin\theta} \; . \qquad \text{(III.2)}$$

As a result, the integral domain is $[\theta_i - \theta_0, \theta_i + \theta_0]$ and $[\varphi_i - \varphi_0(\theta), \varphi_i - \varphi_0(\theta)]$.

V

IV Hertz pressure distribution

The Hertz pressure in Eq. (3.11) is expressed as a function of ϕ while the coefficients, A_n^m and B_n^m, in Eq. (3.47) are derived with the pressure in terms of (θ, φ). Therefore, it is essential to obtain the angle between (r, θ_i, φ_i) and (r, θ, φ). Note that for any point (R, θ, φ) in the load area, $|\varphi - \varphi_i|$ is much smaller than $\pi/2$ because the load normally is very small. According, $0 < \phi \ll \pi/2$.
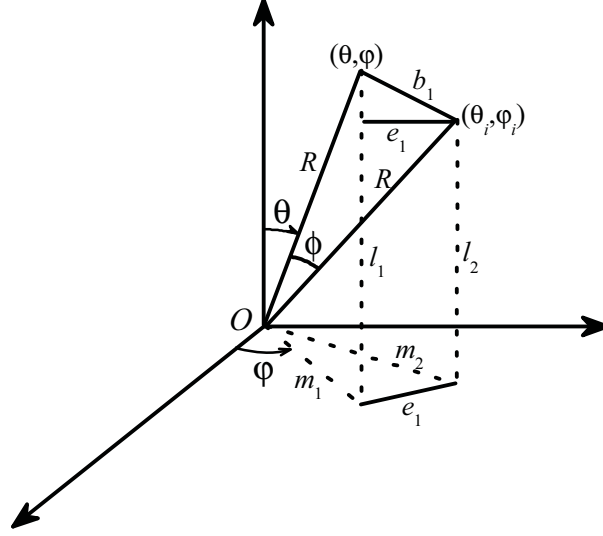

Figure IV.1: The acute angle between the lines (r, θ, φ) and (r, θ_i, φ_i).

$$m_1 = R\sin\theta, \ l_1 = R|\cos\theta|, \ m_2 = R\sin\theta_i, \ l_2 = R|\cos\theta_i| \tag{IV.1}$$

$$\begin{aligned}
e_1 &= \sqrt{m_1^2 + m_2^2 - 2m_1 m_2 \cos(|\varphi - \varphi_i|)} \\
&= R\sqrt{\sin^2\theta + \sin^2\theta_i - 2\sin\theta\sin\theta_i\cos(|\varphi - \varphi_i|)}
\end{aligned} \tag{IV.2}$$

$$b_1 = \sqrt{(l_1 - l_2)^2 + e_1^2} = R\sqrt{2}\sqrt{1 - |\cos\theta\cos\theta_i| - \sin\theta\sin\theta_i\cos(|\varphi - \varphi_i|)}. \tag{IV.3}$$

The angle between the line (r, θ, φ) and the line (r, θ_i, φ_i) is

$$\phi(\theta, \varphi, \theta_i, \varphi_i) = 2\arcsin\left(\frac{b_1}{2R}\right). \tag{IV.4}$$

V The relations between coefficients

The shear stress is 0 at any point on sphere surface. It is thus independent of θ and φ.

For $\sigma_{r\varphi}|_{r=R} = \sigma_{r\varphi}|_{\rho=1} = 0$, the θ independence yields

$$D_{h1}^m(\lambda_{h1} - 1)\cos m\varphi + D_{h2}^m(\lambda_{h2} - 1)\sin m\varphi = 0 \tag{V.1}$$

$$-(C_{l1}^m T_{l1} + C_{l2}^m T_{l2})\sin m\varphi + (C_{l3}^m T_{l1} + C_{l4}^m T_{l2})\cos m\varphi = 0 \tag{V.2}$$

$$-\Pi(R_{n1}^m, I_{n1}^m)\sin m\varphi + \Pi(R_{n2}^m, I_{n2}^m)\cos m\varphi = 0 , \tag{V.3}$$

and for $\sigma_{r\theta}|_{r=R} = \sigma_{r\theta}|_{\rho=1} = 0$, the θ independence yields

$$-D_{h1}^m(\lambda_{h1} - 1)\sin m\varphi + D_{h2}^m(\lambda_{h2} - 1)\cos m\varphi = 0 \tag{V.4}$$

$$(C_{l1}^m T_{l1} + C_{l2}^m T_{l2})\cos m\varphi + (C_{l3}^m T_{l1} + C_{l4}^m T_{l2})\sin m\varphi = 0 \tag{V.5}$$

$$\Pi(R_{n1}^m, I_{n1}^m)\cos m\varphi + \Pi(R_{n2}^m, I_{n2}^m)\sin m\varphi = 0 , \tag{V.6}$$

where $T_{li} = (1 - \mu_{li})\Gamma_{li} + \Lambda_{li}$ $(i = 1, 2)$.

For Eqs. (V.1) and (V.4), the φ independence yields

$$D_{h1}^m(\lambda_{h1} - 1) = 0, \ D_{h2}^m(\lambda_{h2} - 1) = 0 , \tag{V.7}$$

however, λ_h depends on h. As a result

$$D_{h1}^m = 0, \ D_{h2}^m = 0 . \tag{V.8}$$

For Eqs. (V.2) and (V.5), the φ independence yields

$$\begin{cases} C_{l1}^m T_{l1} + C_{l2} T_{l2} = 0 \\ C_{l3}^m T_{l1} + C_{l4}^m T_{l2} = 0 , \end{cases} \tag{V.9}$$

that is,

$$C_{l1}^m = -\frac{T_{l2}}{T_{l1}}C_{l2}^m = L_{l12}C_{l2}^m, \ C_{l3}^m = -\frac{T_{l2}}{T_{l1}}C_{l2}^m = L_{l12}C_{l4}^m . \tag{V.10}$$

For Eqs. (V.3) and (V.6), the φ independence yields

$$\Pi(R_{n1}^m, I_{n1}^m) = 0, \ \Pi(R_{n2}^m, I_{n2}^m) = 0 , \tag{V.11}$$

that is

$$I_{n1}^m = \frac{\Pi(1, 0)}{\Pi(0, -1)} = K_{n12}R_{n1}^m, \ I_{n2}^m = \frac{\Pi(1, 0)}{\Pi(0, -1)} = K_{n12}R_{n2}^m . \tag{V.12}$$

σ_{rr} can be obtained by replacing A_{12}, $(2A_{66})$ and A_{13} in Eq. (3.40) by A_{13}, 0 and A_{33}. For $\rho = 1$, σ_{rr} read as

$$\sigma_{rr} = -\frac{1}{R} \sum_l \sum_{m=0}^l \begin{bmatrix} (C_{l1}^m J_{l1} + C_{l2}^m J_{l2}) \cos m\varphi \\ (C_{l3}^m J_{l1} + C_{l4}^m J_{l2}) \sin m\varphi \end{bmatrix} P_l^m(\cos\theta) \tag{V.13}$$
$$+ \frac{1}{R} \sum_n \sum_{m=0}^n [\Omega_1(R_{n1}^m, I_{n1}^m) \cos m\varphi + \Omega_1(R_{n2}^m, I_{n2}^m) \sin m\varphi] P_n^m(\cos\theta),$$

where Eq. (V.8) has been used.

Applying the boundary condition, $\sigma_{rr}|_{r=R} = \sigma_{rr}|_{\rho=1} = p(\theta, \varphi)$, yields

$$\begin{cases} C_{l1}^m J_{l1} + C_{l2}^m J_{l2} = -A_l^m R \\ C_{l3}^m J_{l1} + C_{l4}^m J_{l2} = -B_l^m R \end{cases} \tag{V.14}$$

and

$$\begin{cases} \Omega_1(R_{n1}^m, I_{n1}^m) = A_n^m R \\ \Omega_1(R_{n2}^m, I_{n2}^m) = B_n^m R. \end{cases} \tag{V.15}$$

The coefficients, $C_{li}^m (i = 1, 2, 3, 4)$, can be derived from the set of equations of (V.9) and (V.14). The coefficients, $(R_{nk}^m, I_{n2}^m)(k = 1, 2)$, can be derived from the set of equations of (V.11) and (V.15).

VI   Three parameter distribution

Munz and Fett (1999) assumed that the scatter of failure strength P_s for brittle component is due to the presence of microflaws. The relation between P_s and flaw size distribution $P_a(a)$ is

$$P_s(\sigma_c) = 1 - \exp\left[- Z\big(1 - P_a(a)\big)\right] . \tag{VI.1}$$

where Z is number of flaws that dominate the failure. It could be volume or surface flaws. We assume that failure starts on the boundary of the contact circle. The threshold load can be introduced with the proposed P_a' (Eq. (4.7)). Equation (VI.1) can be written as

$$\begin{aligned}
P_s(\sigma_c) &= 1 - \exp\left[- Z\big(1 - P_a'(a)\big)\right] \\
&= 1 - \exp\left[- z2\pi R_a\left(\Big(\frac{a_0}{a}\Big)^{r-1} - \Big(\frac{a_0}{a_u}\Big)^{r-1}\right)\right] ,
\end{aligned} \tag{VI.2}$$

where z is the line flaw density along the contact circle, and R_a is the contact radius. Substitution the relation between stress and flaw size in Eq. (4.2), i.e., $\sigma = K_{Ic}/Y\sqrt{a}$, yields

$$P_s(\sigma_c) = 1 - \exp\left[- z2\pi R_a\sqrt{a_0}^m\Big(\frac{Y}{K_{Ic}}\Big)^m(\sigma_c^m - \sigma_u^m)\right] . \tag{VI.3}$$

Here, $m = 2(r-1)$ is the Weibull modulus. The characteristic stress σ_c is the maximum tensile stress on surface derived from Hertz theory. Plugging the relation between σ and F in Eq. (4.3), that is,

$$F = \frac{\pi^3 R^{*2}}{6E^{*2}}\sigma^3 , \tag{VI.4}$$

Equation (VI.3) can be expressed in terms of contact load or force

$$\begin{aligned}
P_s(F_c) &= 1 - \exp\left[- z2\pi\sqrt{a_0}^m\Big(\frac{Y}{K_{Ic}}\Big)^m\Big(\frac{3F_cR^*}{4E^*}\Big)^{\frac{1}{3}}\Big(\frac{6E^{*2}}{\pi^3R^{*2}}\Big)^{\frac{m}{3}}\Big(F_c^{\frac{m}{3}} - F_u^{\frac{m}{3}}\Big)\right] \\
&= 1 - \exp\left[- k\Big(\frac{E^*}{R^*}\Big)^{\frac{2m-1}{3}}\Big(F_c^{\frac{1+m}{3}} - F_c^{\frac{1}{3}}F_u^{\frac{m}{3}}\Big)\right] .
\end{aligned} \tag{VI.5}$$

Here, F_u is the thereshold force below which no failure occurs. k is regarded as a material parameter

$$k = z2\pi\sqrt{a_0}^m\Big(\frac{Y}{K_{Ic}}\Big)^m\Big(\frac{3}{4}\Big)^{\frac{1}{3}}\Big(\frac{6}{\pi^3}\Big)^{\frac{m}{3}} . \tag{VI.6}$$

Equation (VI.5) can be rewritten as

$$P_s(F) = 1 - \exp\left[-\Big(\frac{F}{F_1}\Big)^{\frac{1+m}{3}} + \Big(\frac{F}{F_2}\Big)^{\frac{1}{3}}\right] , \tag{VI.7}$$

where F_1, F_2, m are material parameters according to

$$F_1 = k^{-\frac{3}{1+m}}\Big(\frac{E^*}{R^*}\Big)^{\frac{1-2m}{1+m}} , \quad F_2 = k^{-3}\frac{E^*}{R^*}\Big(\frac{6}{\pi^3}\Big)^m\sigma_u^{-3m} . \tag{VI.8}$$

IX

Moreover, F_u depends on the threshold stress σ_u, that is

$$F_u = \frac{\pi^3 R^{*2}}{6 E^{*2}} \sigma_u^3 \qquad (VI.9)$$

It is assumed that σ_u is a constant for both load cases. For the present crush tests, $R^* = R = 0.25$ mm.

X

$$F_u = \frac{X}{6 E^{*2}} \sigma_u^3$$
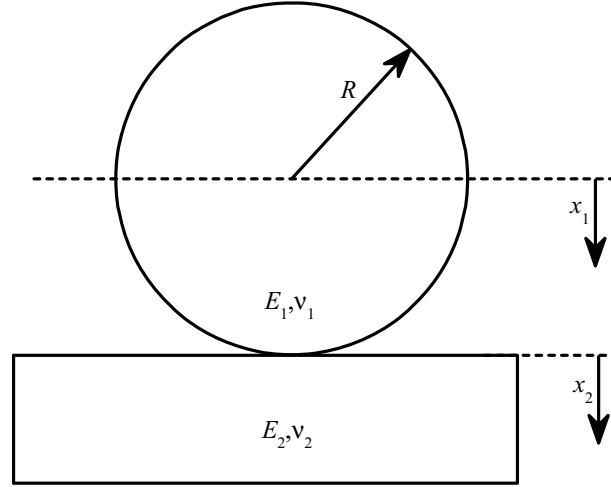
VII Energy absorption for Hertz contact

Figure VII.1: Hertz contact between a sphere and a plate.

Figure VII.1 shows the contact between an elastic sphere and an elastic plate. x_1 denotes the displacement of the sphere center. x_2 denotes the displacement of the plate surface. At the initial point contact, it holds $x_1 = x_2 = 0$. From Hertz theory, the relation between them is

$$\frac{x_1 - x_2}{x_2} = \frac{\frac{1-\nu_1^2}{E_1}}{\frac{1-\nu_2^2}{E_2}} = \frac{\alpha_1}{\alpha_2} \ , \tag{VII.1}$$

where $\alpha_i = (1 - \nu_i^2)/E_i$. The forces slow applied on the sphere and on the plate are the same. Therefore, the strain energy in the sphere W_1 and the plate W_2 satisfies

$$\frac{W_1}{W_2} = \frac{\int_0^{x_1 - x_2} F d(x_1 - x_2)}{\int_0^{x_2} F dx_2} = \frac{\alpha_1}{\alpha_2} \ . \tag{VII.2}$$

Meier et al. (2009) took the kinitec energy of flying particles W_k as the totall energy absorbed by the sphere and plate. The energy stored in the sphere is distributed according to Eq. (VII.2), that is, $W_k \alpha_1 / (\alpha_1 + \alpha_2)$. For slow compression tests, we assume that the total work is completely transformed into strain energy which is stored in the sphere and the plate, respectively.

During the period that F increases from 0 to F_0 while the overlapping between sphere and plate δ increases from 0 to δ_0, the total work reads as

$$W_{\text{tot}}(\delta_0) = \int_0^{\delta_0} F(\delta) d\delta = \frac{2}{5} \left(\frac{16 R E^{*2}}{9} \right)^{\frac{1}{2}} \delta_0^{\frac{5}{2}} \tag{VII.3}$$

or

$$W_{\text{tot}}(F_0) = F_0 \delta_0 - \int_0^{F_0} \delta(F) dF = \frac{2}{5} \left(\frac{9}{16R} \right)^{\frac{1}{3}} \frac{F_0^{\frac{5}{3}}}{E^{*\frac{2}{3}}} \ , \tag{VII.4}$$

XI

where δ_0 and F_0 satisfy

$$\delta_0 = \left(\frac{9F_0^2}{16RE^{*2}}\right)^{\frac{1}{3}} . \tag{VII.5}$$

As $W_{\text{tot}} = W_1 + W_2$, the strain energy in the sphere reads as

$$W_1 = \frac{\alpha_1}{\alpha_1 + \alpha_2} W_{\text{tot}} . \tag{VII.6}$$

Resume

Personal Details:

Name:	Shuo Zhao
Address:	Asternweg 8, 76297, Stutensee
Date / Place of birth:	28 April 1983 / Xinji, China
Marital status:	Married since 8 August 2007 to Lina Mi

Education:

1989 - 1995	Primary school
1995 - 1998	Middle school
1998 - 2001	High school
2001 - 2005	Bachelor of Engineering (Engineering Mechanics), Beijing Institute of Technology, China
2005 - 2007	Master of Engineering (Solid Mechanics), Beijing Institute of Technology, China

Experience:

Sep 2007 - present	Doctor candidate, Institute for Materials Research II (IMF II), Karlsruhe Institute of Technology Campus Nord, Germany.

Acknowledgement

First of all, I would like to gratefully and sincerely thank my advisor, Prof. Dr. Marc Kamlah, for his guidance, friendship, and especially his patience during the past three years. Because of my poor linguistic ability, he has to spend much time understanding what I want to say. Moreover, I would like to thank him for giving me the freedom to conduct researches that I like. Finally, thanks for his concern about my family as well. I am very pleased to have worked with him for three years.

I would also like to thank previous my colleague, Dr. Yixiang Gan. He gave me a lot of suggestions about my research. It is impossible for me to complete this work without his help. He also helped me a lot on my personal life. I am grateful to Dr. Christoph Eberl, Mr. Tobias Kennerknecht, and Mr. Ewald Ernst, without whom I have no chance to carry out the crush tests. I would like to thank Mr. Rolf Rolli for providing the experimental data of crush load for pebbles. I would also thank Dr. Regina Knitter for providing data and photos of the materials and her useful suggestions. I would like to thank Dr. Martin Härtelt and Dr. Heinz Riesch-Oppermann to help me to make use of the software STAU.

I would like to thank Prof. Dr. Oliver Kraft, Dr. Nigel John Smale, and Dr. Ratna Annabattula for finding time from their busy schedules to carefully read this thesis. I would specially thank Dr. Ratna Annabattula and Mr. Holger Schwaab for their help on the software for thesis writing. I would thank Mrs. Julia Ott for the German translation of the abstract of this thesis.

I would like to thank my previous and present officemates, Dr. Jie Wang and Mrs. Magalie Huttin, for setting up a nice and cheerful working condition at the office. Finally, and most importantly, I would like to thank my wife Lina for her continuous support and encouragement. I thank my mother, Manhua Zhao, and my father, Yongzhen Zhao, for the faith in me and allowing me to be as ambitious as I want.